For Reference

NOT TO BE TAKEN FROM THIS ROOM

Ex libris
universitatis
albertaensis



BRUCE PEEL SPECIAL COLLECTIONS LIBRARY
University of Alberta

REQUEST FOR DUPLICATION

I wish a photocopy of the thesis by_____

entitled_____

The copy is for the sole purpose of private scholarly or scientific study and research. I will not reproduce, sell or distribute the copy I request, and I will not copy any substantial part of it in my own work without the permission of the copyright owner. I understand that the Library performs the service of copying at my request, and I assume all copyright responsibility for the item requested.

Name ~~A~~_____

Address_____

List pages copied_____

Date_____ Signature_____

Name Nasser Albawtamani

Address 606 CME

List pages copied Abstract, Table of contents, P. 144 to 148 & P. 177 - 189

Date Oct. 14, 98 Signature [signature]

Name_____

Address_____

List pages copied_____

Date_____ Signature_____

Name_____

Address_____

List pages copied_____

Date_____ Signature_____

Name_____

Address_____

List pages copied_____

Date_____ Signature_____


Digitized by the Internet Archive
in 2023 with funding from
University of Alberta Library

https://archive.org/details/Oguztoreli1984

A MATHEMATICAL APPROACH TO THE SOLVENT LEACHING OF TAR SANDS

by

MUSTAFA OGUZTORELI

A THESIS

SUBMITTED TO THE FACULTY OF GRADUATE STUDIES AND RESEARCH

IN PARTIAL FULFILMENT OF THE REQUIREMENTS FOR THE DEGREE

OF MASTER OF SCIENCE

IN

PETROLEUM ENGINEERING

DEPARTMENT OF MINERAL ENGINEERING

EDMONTON, ALBERTA

SPRING, 1984

This thesis is dedicated to the warmest memories of my beloved younger sister, Billur, who left her earthly struggle against cancer for the everlasting peace of God.

ABSTRACT

Solvent flooding is the basis of a wide range of enhanced oil recovery methods, and has been shown to be a possible method of creating initial steam injectivity in tar sands. This investigation presents a unique model for the dissolution of a semi-solid bitumen, resulting from the injection of a solvent. The solution of the mathematical equations, describing this phenomena is discussed. Results, for a series of two-dimensional problems, are presented. Numerical aspects are addressed.

The mathematical treatment is based upon the rapid dispersion of solvent in the pores, which contain bitumen particles dissolving in a streaming interstitial solution. Macroscopic transport mechanisms, based upon the microscopic phenomena, trace the course of the diffusing species in a dynamically interactive solid-liquid network. The fluid velocity field is implicitly dependent on both solvent concentration and liquid saturation, while an apparent diffusion coefficient tensor includes the combined effects of molecular diffusion and directional velocity dispersion. The bitumen particles are given spherical symmetry such that a radial dissolution integro-differential equation accounts for the volume changes from solvent transfer into the initially immobile bitumen.

An overall numerical approach to the nonlinear system of equations determines the state vector of the fluid pressure, the fluid phase solvent concentration and the fluid saturation. The instantaneous radii of the bitumen particles are determined from an analytical solution of the moving boundary problem associated with the transfer of solvent

into a single particle from the streaming solution. The macroscopic saturation follows from a localized average particle radius. Together with the combined Darcy-continuity and convective-diffusion with adsorption equations, the coupled system is solved by a direct approach, using finite difference techniques.

It is shown that three dimensionless groups control the bitumen leaching process. In the absence of fluid flow, the dissolution of bitumen is governed by the Damköhler and solvent capacity numbers. In the absence of dissolution, the Peclet number governs the miscible displacement of an initial bitumen distribution in the fluid phase.

This work presents computational results for a series of two-dimensional problems with focus on the five spot flow geometry, showing the importance of the model developed.

ACKNOWLEDGEMENTS

I wish to express my sincere gratitude to my supervisor, Professor S.M. Farouq Ali for his guidance, assistance and encouragement during the course of this thesis.

I would like to thank Professor R.G. Bentsen for the informative discussions concerned with my research.

I wish to convey my gratitude to my parents for their love, encouragement and patience.

A special thanks to Mrs. Vivian Spak for typing this thesis.

TABLE OF CONTENTS

CHAPTER		PAGE
I	INTRODUCTION	1
	1.1 Statement of the Problem	1
	1.2 Literature Survey	3
	1.3 Tensor Notation	9
	1.4 Finite Difference Framework	9
	1.5 Thesis Structure	10
II	THEORETICAL FORMULATION	13
	2.1 The Porous Region	13
	2.2 Radial Dissolution	14
	2.3 Convective-Diffusion with Adsorption	19
	2.4 Darcy-Continuity	24
	2.5 Boundary Conditions	28
III	SIMULATOR DEVELOPMENT	32
	3.1 Central Differences	32
	3.2 Numerical Dispersion	37
	3.3 Time Integration	38
	3.4 The Associated Difference Equation for Particle Radius	41
	3.5 The Associated Difference Equation for Pressure .	43
	3.6 The Associated Difference Equation for Concentration	47
	3.7 Direct Solver	63
	3.8 Successive Substitution	83

CHAPTER PAGE

IV MISCIBLE DISPLACEMENT 89

4.1 Linear Convective Diffusion 89

4.2 Numerical Response and Tracking 92

4.3 The Five Spot 105

4.4 Grid Orientation and Viscosity Effects 111

V LEACHING 131

5.1 Single-Cell Dissolution 131

5.2 Damköhler Effects 139

VI CONCLUSION 144

6.1 Discussion 144

6.2 Further Study 148

REFERENCES 149

APPENDIX A. THE ANALYTICAL SOLUTION TO THE RADIAL SPHERICAL DIFFUSION EQUATION WITH A TIME DEPENDENT BOUNDARY 153

APPENDIX B. TRUNCATION CANCELLATION PROCEDURE FOR CONVECTIVE DOMINANT DISPLACEMENTS 158

APPENDIX C. THE ANALYTICAL SOLUTION FOR THE ONE-DIMENSIONAL CONSTANT-COEFFICIENT CONVECTIVE-DIFFUSION EQUATION 177

APPENDIX D. THE OPERATOR COMPACT IMPLICIT METHOD 184

LIST OF TABLES

Table	Description	Page
3.7-1	Possible Entry Combinations for R_ℓ^* and L_ℓ^*	77
3.7-2	Entry Assignment Tests for R_ℓ^* and L_ℓ^*	78
4.3-1	Miscible Displacement Simulation Data Set 1	108
4.3-2	Displacement Similarity - Injection Rate Effects	110
4.3-3	Displacement Similarity - Dispersion Effects	113
4.3-4	Asymptotic Displacement Similarity	115
4.4-1	Numerical Fingering	120
4.4-2	Modes of Numerical Fingering	122
4.4-3	Miscible Displacement Simulation Data Set 2	125
4.4-4	Displacement Similarity - Viscosity Effects	127
4.4-5	Viscous Fingering	130
5.2-1	Leaching Simulation Data Set	141

LIST OF FIGURES

Figure		Page
2.2-1	Radial Dissolution	17
2.3-1	Directional Dispersion	20
3.1-1	The Mesh-Centered Grid	33
3.1-2	The Nine-Point Difference Star	36
3.6-1	Impermeable Boundary	54
3.6-2	Outlet Sink Boundary	57
3.6-3	Inlet Source Boundary	60
3.7-1	Natural Ordering	64
3.7-2	Alternate Diagonal Ordering	66
3.7-3	D_4 Transformation	69
3.7-4	General Form of A_{D_4}	70
3.7-5	General Forms of Upper and Lower Matrices	71
3.7-6	General Forms of L_{22} and R_{22} Submatrices	74
3.8-1	Leap-Frog Iteration Loop (m)	84
3.8-2	Newton-Raphson Iteration Loop (k)	85
3.8-3	Time Advance Loop (n)	88
4.1-1	Series Solution - Lower Convergence Limit	93
4.1-2	Series Solution - Convergence Characteristics	94
4.1-3	Peclet Effects - The Linear Problem	95
4.2-1	Numerical Solutions - Low Cell - Peclet Numbers	97
4.2-2	Numerical Solutions - Moderate Cell - Peclet Numbers	100

Figure		Page
4.2-3	OCI Instability - Lower Limit	101
4.2-4	OCI Instability - Upper Limit	102
4.2-5	Numerical Solutions - High Cell - Peclet Numbers	103
4.3-1	Displacement Similarity - Injection Rate Effects	109
4.3-2	Displacement Similarity - Dispersion Effects	112
4.3-3	Asymptotic Displacement Similarity	114
4.3-4	The Stable TCP Solution for Convective Dominant Displacements	116
4.4-1	Diagonal and Parallel Grids	118
4.4-2	Numerical Fingering	119
4.4-3	Modes of Numerical Fingering	121
4.4-4	Mobility - Diffusivity Approximation	124
4.4-5	Displacement Similarity - Viscosity Effects	126
4.4-6	Viscous Fingering	129
5.1-1	Swelling - Solvent Absorption	134
5.1-2	Dissolution - Solvent Adsorption	136
5.1-3	Dissolution - Combined Adsorption with Absorption	137
5.1-4	Dissolution Avalanching - High Capacitance	138
5.2-1	Leaching - Damköhler Effects on Production	142

NOMENCLATURE

C - macroscopic liquid phase volumetric solvent concentration

C_s - microscopic solid phase volumetric solvent concentration

C^* - critical transition concentration

D_0 - liquid phase molecular diffusion coefficient

D_{ij} - apparent diffusion coefficient tensor element

D_ℓ - apparent longitudinal diffusion coefficient

D_s - solid phase molecular diffusion coefficient

D_t - apparent transverse diffusion coefficient

d_p - grain particle diameter

$\hat{e}$ - unit basis vector

f,F - convolution kernels

F_r - formation resistivity factor

g - acceleration due to gravity

h - height

k - permeability

L - length

N_{Da} - Damköhler number

N_{Pe} - Peclet number

N_p - particle number density

p - hydrodynamic pressure

q_{IN} - injection rate

r - radial coordinate

r_p - spherical particle radius

$\dot{r}_p$ - velocity of dissolution

S - liquid phase saturation

t - time

t_d - dimensionless time of dissolution

$\vec{u}$ - Darcy velocity

$\vec{w}$ - mass flux density

W - width

x,y - spatial coordinates

Δz - thickness

α - adsorption coefficient

α_s - skin factor

δ^* - transition layer thickness

θ - velocity angle

μ - viscosity

ϕ - instantaneous porosity

ϕ_m - matrix porosity

ρ - density

σ - packing inhomogeneity factor

τ - dimensionless time of miscible displacement

ξ - normalized spatial coordinate

Subscripts

c - convective

d - diffusive

e - equilibrium

i,j - spatial indices

ℓ - longitudinal

o - oil

p - particle

s - solvent (or solid)

t - transverse

0 - initial (or reference)

+ - right limit

- - left limit

Superscripts

* - transition

~ - tensor quantity

· - time rate of change

^ - unit vector

→ - vector quantity

' - velocity frame

$\overline{}$ - volume average

CHAPTER ONE

INTRODUCTION

Man's use of bitumen dates back to the roots of civilization, historically recorded as early as the legendary Tower of Babel[1]. Through the ages, man has grown accustomed to depend on petroleum. The Eygptians lined their graineries with bitumen and used its derivatives to mummify their Pharaohs, while Roman ladies applied it as cosmetic by the light of their petroleum fueled lamps. Present day civilization absorbs it insatiably while science labours ad infinitum to produce it.

Mega-projects have been proposed for producing supergiant underground fields of tar, which have remained untouched for millennia. Modern technology must first overcome virtual immobility before these ancient fields flow. The subject of this work concerns itself with bitumen leaching from these massive sands as a viable recovery procedure with the technology at hand.

1.1. Statement of the Problem

Bitumen recovery from tar sands is limited by the low injectivity associated with the displacement of the highly viscous tar. Miscible, or solvent flooding dilutes the oil in place and effectively increases the fluid mobility.

Favourable viscosity ratios provide for the stable advancement of the displacement front, with the limiting solvent-oil contact surface propagating in a piston-like fashion. Adverse viscosity ratios initiate

frontal instability, with the viscous fingering of solvent by-passing a major portion of the oil in place. For the extreme viscosity ratios characteristic of tar sand, the solvent rapidly fingers through the medium to give an early breakthrough. Once these high mobility fingers have set their paths of least resistance, dissolution becomes the controlling mechanism for bitumen extraction.

The mechanisms by which solvent fingers through the medium is beyond the scope of this work. The current problem concentrates on the transport phenomena after breakthrough. Earlier experiments by S.M. Farouq Ali have used gas injection techniques to obtain uniformly flooded tar sand packs with solvent at low saturations. This study considers the breakthrough time to be negligible with respect to the recovery time-scale and the injected solvent is assumed to instantaneously invade all interstices to give an initial continuity throughout.

The main objectives of this work are to develop a two-dimensional mathematical model for the in-situ isothermal solvent leaching of bitumen from tar sand, the implementation of solution and the analysis of simulated results.

Macroscopic transport phenomena are used to predict the state vector of fluid pressure, fluid solvent concentration and fluid fraction—essentially describing the leaching process. Simulation provides the means for the numerical advancement of a mathematical flood through a discrete representation of the physical system, with similarity groups establishing the scaling criterion between reservoir and laboratory conditions.

Two mechanisms compete for leaching status — miscible displacement and dissolution kinetics. These special cases are to be investigated in order to fully understand the individual mechanisms, and their contributions to the overall process.

1.2. Literature Survey

Current literature on leaching phenomena assume small porosity change in the reaction zone[2,3] limited to the solution mining of minerals. Solution mining considers the dissolution of a porous rock matrix by surface reaction[4,5], whereas the leaching of tar sands dissolves the interstitial bitumen. The present work relates porosity change to the dissolution of spherical bitumen particles, embedded in an inert rock matrix, subject to solvent adsorption.

Diffusion in spheres and linear moving boundary problems have been studied in great detail[6,7]. Ready and Cooper[8] modelled the dissolution of a single sphere in an infinite medium, accounting for the effects of the moving boundary and the resulting convective transport from the propagating interface. They assumed the interface reaction to be virtually instantaneous, with a constant solute concentration at the interface and interdiffusion as the only mechanism controlling the rate of interface motion. Transport within the sphere's interior was assumed sufficiently rapid to give a constant internal solute concentration, and the concentration in the surrounding solution varied with radial distance only. Their main concern was to model the physical problem of bubble growth and dissolution. In contrast, this work assumes dispersion in a finite liquid phase to be sufficiently large, such that a local

macroscopic average represents the microscopic concentration at every point in the solution about a multitude of spherical tar particles. In particular, radial diffusion into the solid interior is included, accounting for the solvent stored internally by absorption.

The solution process in polymer-solvent systems produce a thin transition layer[9], separating solid from liquid. Rosner and Epstein[10] investigated the effect of interface kinetics on bubble growth by introducing a thin concentration boundary layer to obtain closed form solutions. The basic concept of a thin transition layer is utilized in this work to relate first-order adsorption to the solvent transfer across the free boundary.

Mathematically, a radial spherical moving boundary problem determines the instantaneous radii of dissolving particles based on an average local size distribution for a given number density. Material balance, relating absorption kinetics to the rate of solvent transfer across the free boundary, is described by an integro-differential process. The liquid pore space available for miscible displacement follow directly from the average radius of the spherical dissolution front.

Miscible displacement is modelled by the convective-diffusion and Darcy-continuity equations[11,12]. Analytical solutions are not available for the general miscible displacement problem due to reservoir heterogeneities and the nonlinearity of the governing equations. Several methods[12-36] have been proposed for the numerical solution, but difficulties such as overshoot[12], numerical dispersion[13,14] and grid orientation effects[15] limit their range of applicability.

The Darcy-continuity equation is a second-order elliptic partial differential equation whereas the convective-diffusion equation behaves like either a second-order parabolic equation when dispersion dominates, or a first-order hyperbolic equation when transport dominates.

The second-order central difference approximation developed for parabolic equations suffers from nonphysical oscillations, or overshoot,[12] when convection becomes significant, and a finer grid mesh becomes necessary to resolve concentration profiles.[16] First-order upstream differences for approximating the convection term eliminates overshoot but introduces large numerical dispersion errors[13,14] which may be several orders of magnitude larger than the physical dispersion term. Implementation of these methods are advantageously simple and extension to multidimensional problems follow with relative ease. Their two-dimensional versions comprise the standard five-point difference formulas, serving as basis for many schemes offering an improvement in accuracy.

Laumbach[17] shows that a truncation cancellation procedure using weighted spatial averages with central differences, gives a high-order method eliminating overshoot and numerical dispersion for select time-steps. The method is conditionally stable, and an extension to two-dimensional problems is outlined using the alternating direction implicit method.[18]

Larson[19,20] uses explicit, upstream-weighted finite differences in space and time with variably timed flux updating. The convected flux is updated with a frequency determined by the concentration velocity — a linear combination of a downstream-weighted convection

velocity with a central-differenced dispersion velocity. Numerical dispersion is reduced, however frontal profiles suffer from the inherent inaccuracy of finite-difference pressure and flow fields.

Investigators including Settari, Price and Dupont[21] and Young[22] have shown that finite elements, based on Galerkin Methods,[23,24] have higher accuracy than standard finite differences.

Garder, Peaceman and Pozzi[25] proposed the method of characteristics used for hyperbolic equations to resolve sharp fronts at high convection rates. A system of ordinary differential equations determine the position and concentration of moving points using the finite-difference velocities interpolated on a stationary grid.

Ewing, Russel and Wheeler[26] have considered using mixed methods with a modified method of characteristics. The base method utilizes characteristic flow directions to model convection and finite elements for diffusion and dispersion. They suggest that care must be exercised when treating characteristics around wells and across flowing boundaries. The method generates some overshoot, reflecting the inability to resolve sharp fronts on a course mesh.

Other schemes have been proposed using a somewhat different approach to the convective-diffusion problem.

The random choice method[27] is based on operator splitting with fractional steps treating convection and diffusion separately. The first fractional step solves the convection equation without diffusion using Glimm's (piecewise sampling) method[28,29] to calculate the convective flow, and a second fractional step accounts for the parabolic character of the diffusion term using central differences. The method

resolves sharp fronts, but has first-order random errors in frontal position due to the sampling procedure used.

Schemes, including the operator compact implicit[30,31] method and single cell high order formulas,[32,33] use constraints based on the highest order accuracy possible on the smallest difference star, to determine suitable weighting coefficients. The single cell high order scheme, based on a local series solution, is intrinsically multi-dimensional and uses a nine-point formula for the two-dimensional case. The operator compact implicit procedure derives a spatial operator for the combined convective and diffusive terms using Taylor series. Restricted invertibility[30] of the compact operator limits this methods range of applicability and the extension to multidimensional problems involve the explicit evaluation of inverse operators for an alternating direction implicit procedure.

The fundamental problem with all multidimensional numerical methods, and in particular five-point schemes, is the nonuniqueness of solution for different orientations of the grid with respect to the pattern flow lines. The nonuniqueness was first observed by Todd et al.[15] when the solution of an identical problem on two extreme grid orientations produced conflicting results. They proposed the two-point upstream mobility approximation to alleviate the grid orientation problem, but were only successful for mildly adverse conditions.

Yanosik and McCracken[34] postulated that the grid orientation problem was caused by the lack of flow from a grid block to its diagonal neighbours, and introduced a nine-point formulation to account for this flow. The method alleviates grid orientation effects at moderately

adverse conditions, however frontal instabilities develop in both orientations at higher mobility ratios.

Robertson and Woo[35] proposed the use of orthogonal curvilinear coordinates which coincide with the streamlines and equipotentials for pattern floods having a unit mobility ratio, in place of conventional rectilinear grids, to reduce the grid orientation effect.

Vinsome and Au[36] discussed the directional dependence of the pressure field truncation error as the source for these orientation effects and suggested the use of total harmonic mobilities in place of standard upstream mobilities.

Ewing et al.[26] also mentioned that the numerical dispersion generated by truncation error is not rotationally invariant and this directional dependence causes grid orientation effects to occur in the solution.

For the extremely adverse mobility ratios associated with the miscible displacement of tar, all the mentioned techniques will exhibit some numerical deficiency. In the combined miscible displacement and dissolution problem, numerical difficulties are reduced by assuming solvent instantaneously invades the medium to give a uniform initial concentration. The oil-solvent discontinuity is implicit in the dissolution equation and concentration gradients remain small at the expense of a time dependent fluid saturation.

The solution methodology followed in this work is based on its simplicity of implementation. A five-point scheme using finite differences is the skeletal framework. A novel approach to eliminate numerical dispersion, reduce overshoot and alleviate grid orientation

effects is attempted for two-dimensional miscible floods. Extending Laumbach's[17] work to be used in conjunction with direct solution algorithms, this approach transforms the third-order truncation into local velocity or streamline coordinates, cancelling a dominant longitudinal error flux term at every mesh point.

1.3. Tensor Notation

This work has adopted Einstein's notation convention for differential expressions, where summations are to be performed over repeated indices in order to evaluate the tensor products. Standard vector notation is also used liberally, with "tilde" ($\sim$) as a superscript to distinguish tensor quantities.

1.4. Finite-Difference Framework

Three approaches may be considered in the derivation of finite difference analogs of the differential system. The partial differential equations can be discretized using finite differences in which reflection conditions with the introduction of fictitious points outside the physical grid are used to satisfy the boundary conditions. Secondly integral finite differences are obtained by spatially discretizing the integral conservation laws directly, bypassing the intermediate step of writing down the partial differential equations. Discretization of the integral forms yield transmissibilities between adjacent points, which are readily interpreted as the conductivities at the bounding faces of the volume element. The use of half and quarter blocks eliminates the need for fictitious points and the boundary conditions

are satisfied by constraining the appropriate transmissibility. Where central-differences are concerned, both approaches invariably lead to the same algebraic equations. The third approach constructs finite difference analogs of the differential system on the basis of existing mesh points in the grid. To obtain boundary difference equations of the same order, the boundary difference star must extend deep into the interior to determine the equation for the specified condition at the peripheral point.

The governing differential equations follow from integral conservation laws, and without any loss of generality, central-differencing techniques are applied to the integral forms. The author feels that integral discretization gives a better correspondence to the physical flow terms, and an increased compactness of notation, with superscripts denoting time levels and subscripts giving the spatial coordinates.

1.5. Thesis Structure

This introductory chapter has set the groundwork for the following chapters. The problem has been posed, a skeletal background presented and a solution methodology identified.

Chapter Two translates the physical aspects of the problem into mathematical language, carefully defining mechanistic dynamics with elaborate theoretical formulation.

Chapter Three outlines the solution, with discrete mathematical algorithms aimed at high-speed digital computers.

Chapter Four isolates the special case of miscible displacement,

Page left blank

scrutinizes simulator performance, and investigates similarity groups.

Chapter Five studies the effect of dissolution kinetics on phase behaviour, combines it with miscible displacement to analyze predicted leaching production data.

The final chapter draws conclusions on the basis of completed work, with remarks directed for further study.

Four appendices detail rigorous mathematical derivations, covering analytical solutions and high-order finite difference schemes.

CHAPTER TWO

THEORETICAL FORMULATION

The mathematical derivation to the physical problem of in-situ isothermal solvent leaching of bitumen from tar sand is presented. The particular field geometry of a two-dimensional rectangular lamina with a two-component solvent-bitumen system is considered. A dissolution model for bitumen spheres is proposed.

A series of mass balances are executed on both macroscopic and miscroscopic scales to derive the Darcy-continuity equation for fluid flow, the convective-diffusion with adsorption equation for solvent transport in the fluid stream, and the radial dissolution equation for the relative volume fractions of solid and liquid phases. Conditions for inlet, outlet and impermeable boundaries are established.

2.1. The Porous Region

Let $F\{x_i\}$ represent a stationary reference frame with the cartesian basis vectors $\{\hat{e}_i\}$. Consider a finite porous lamina, R, of uniform thickness, Δz, whose curvature is determined by the height, h, as measured from a horizontal reference. The projection of R on the horizontal is a rectangle with dimension (L,W). The region R is bounded by a closed surface, $\sum$, in which an inert rock matrix provides pore space for both liquid and semi-solid phases to coexist. The liquid phase consists of a quasi-continuous streaming solution, where constituent species propagate by convective and diffusive transport mechanisms. The semi-solid phase is composed of a discrete set of spherical solute

particles confined to the pores of the matrix rock. Constituent semi-solid species propagate by diffusion only. By definition, the streaming solution separates all solute particles from the rock matrix to provide maximum surface area for interphase mass transfer.

Consider a finite volume element, ΔV, bounded by the closed surface, σ, about a macroscopic point $P(\vec{x})$. The instananeous porosity, ϕ, is defined as the volume fraction in which convection currents exist — the liquid phase. The time independent matrix porosity, ϕ_m, is the volume fraction spanned by the combined solid-liquid system, with the saturation, S, as the liquid fraction.

$$S = \frac{\phi}{\phi_m} \qquad 2.1(1)$$

Let $R_s(\vec{x})$ represent the macroscopic solid subregion in the interior of the volume element $\Delta V(\vec{x})$. The solute particles have a uniform local size distribution such that a particle number density, N_p, relates the average particle radius, r_p, to the macroscopic liquid saturation.

$$S = 1 - \frac{4\pi}{3} \frac{N_p}{\phi_m} r_p^3 \qquad 2.1(2)$$

2.2. Radial Dissolution

Concentration gradients are established at the solute-solution contact surface of each particle as a result of the discontinuities in diffusive properties. These gradients create diffusion currents on the molecular level, carrying bitumen from the solute particles into

the streaming interstitial solution. As bitumen desorbs from the solute, the depletion in solid mass sets the bounding spherical surface into motion to balance the consequent shrinkage in solid volume. The radial advance velocity of the solute-solution contact surface is defined as the velocity of dissolution, $\dot{r}_p$.

$$\dot{r}_p = \frac{dr_p}{dt} \qquad 2.2(1)$$

A fluid source instantaneously invades the medium to give an initial liquid saturation with uniform solvent composition throughout. All solid particles are initially bitumen and void of solvent. A critical concentration, C*, determines the solidity of the solid-liquid interface. By definition, the solvent concentration within the solid interior is less than or equal to the critical and any point external in the liquid phase is greater. The interfacial concentration buildup to critical is instantaneous and the single-valued surface concentration is C* for the duration of the entire dissolution process.

All particles have homogeneous, isotropic diffusive properties, such that only normal concentration gradients exist at the contact surface. A semi-solid molecular diffusion coefficient, D_s, determines the diffusion rate of solvent in the solid interior. Microscopic mixing in the interstitial liquid is rapid and an ambient concentration stabilizes outside a thin transition layer of thickness, δ^*. The radial microscopic solvent concentration, C_s, is continuous across the transition zone with discontinuities in slope marked by the rapid change

in diffusive properties across the solid-liquid contact surface as depicted in Figure 2.2-1. The concentration is assumed linear across the transition layer and the stabilized ambient approximated by the local macroscopic average, C.

Diffusion is Fickian. An apparent convection flux across the transition layer results from the moving concentration surface. A solvent balance across the transition layer equates the solvent influx from the liquid to the flux entering the solid,

$$D_s \left.\frac{\partial C_s}{\partial r}\right|_{r_{p-}} + C^* \dot{r}_p = \frac{D_s^*}{\delta^*} (C-C^*) + C\dot{r}_p \qquad 2.2(2)$$

with D_s^* as the mean radial diffusion coefficient across the transition zone. The adsorption coefficient, α,

$$\alpha = \frac{D_s^*}{\delta^*} \qquad 2.2(3)$$

governs the rate of solvent adsorption across the transition zone. Conservation of solvent mass over the solid subregion equates the rate of solvent transfer from the liquid phase, through the transition layer, to the net rate of accumulation within the solid spheres.

$$4\pi \frac{\partial}{\partial t} \left[\int_0^{r_p} C_s r^2 dr\right] = 4\pi r_p^2 \left[C\dot{r}_p + \alpha(C-C^*)\right] \qquad 2.2(4)$$

Each sphere has an initial radius, r_0, and is subject to radial diffusion with a time dependent or moving boundary.

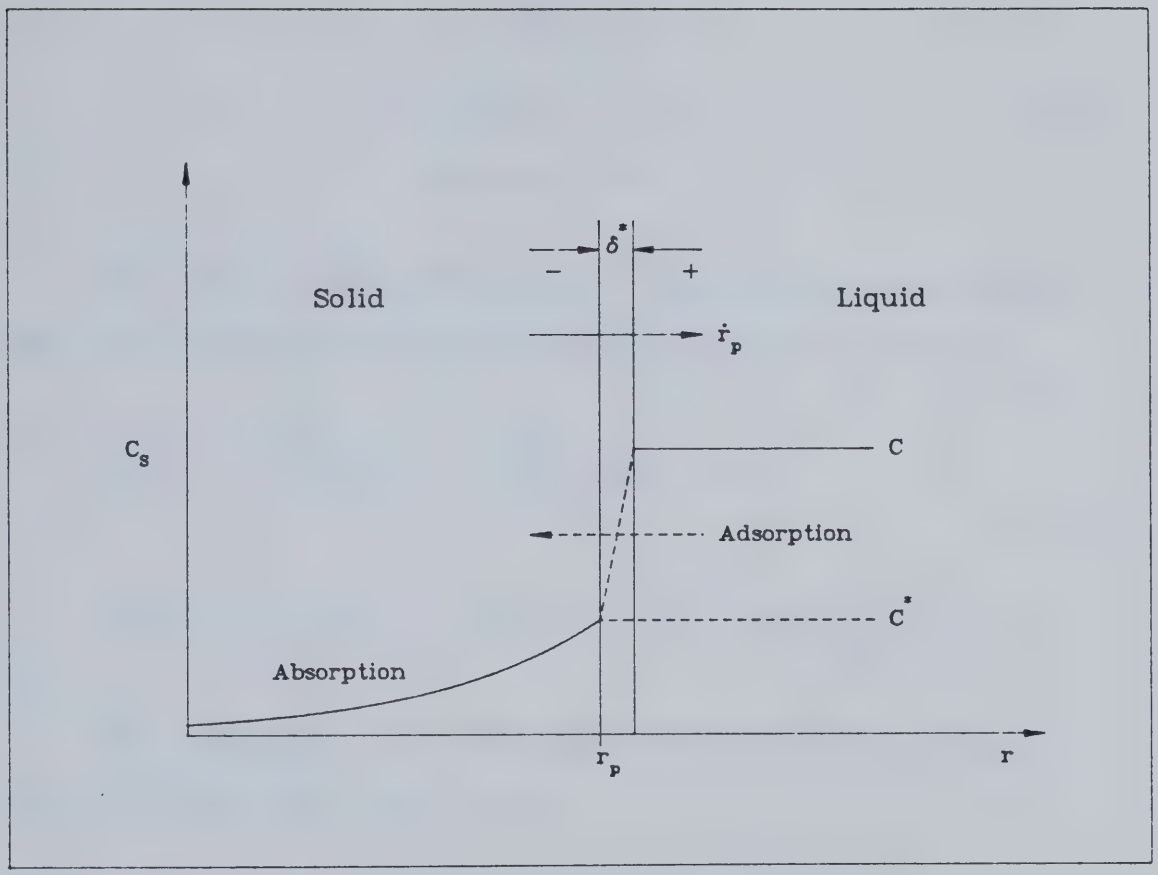


Figure 2.2-1 : Radial Dissolution

$$\frac{D_s}{r^2}\frac{\partial}{\partial r}\left(r^2\frac{\partial C_s}{\partial r}\right) = \frac{\partial C_s}{\partial t}\ ; \quad 0 \le r \le r_p(t) \qquad 2.2(5)$$

$$\left.\begin{aligned} r_p(0) &= r_0 \\ C_s(r_p, t>0) &= C^* \\ C_s(r, t=0) &= 0 \end{aligned}\right\} \qquad 2.2(6)$$

The instantaneous radial solvent concentration is determined analytically using the method of Laplace transform in Appendix A.

$$\left.\begin{aligned} C_s(r,t) &= C^*\left[r_0 f(r,t) + \int_0^t \dot{r}_p(\tau) f(r,t-\tau)\,d\tau\right] \\ f(r,t) &= \left[\frac{1}{r_p} + \frac{2}{\pi r}\sum_{k=1}^{\infty}\frac{(-1)^k}{k} e^{-k^2\pi^2 D_s t/r_p^2} \sin\left(\frac{k\pi r}{r_p}\right)\right] \end{aligned}\right\} \qquad 2.2(7)$$

The solvent mass within the sphere is obtained by spatially integrating the radial concentration.

$$\left.\begin{aligned} \int_0^{r_p} C_s r^2 dr &= C^*\left[r_0 F(t) + \int_0^t \dot{r}_p(\tau) F(t-\tau)\,d\tau\right] \\ F(t) &= r_p^2\left[\frac{1}{3} - \frac{2}{\pi^2}\sum_{k=1}^{\infty} e^{-k^2\pi^2 D_s t/r_p^2}\right] \end{aligned}\right\} \qquad 2.2(8)$$

Substitution of solvent mass into the conservation equation 2.2(4) yields the radial dissolution integro-differential equation for the sphere radius, r_p, as a function of the macroscopic liquid phase solvent concentration, C.

$$C^* \frac{\partial}{\partial t}\left\{r_0 F(t) + \int_0^t \dot{r}_p(\tau) F(t-\tau)\,d\tau\right\} = r_p^2\left[C\dot{r}_p + \alpha(C-C^*)\right] \qquad 2.2(9)$$

2.3. Convective-Diffusion with Adsorption

All macroscopic properties are assumed uniform in the vertical direction such that the rectangular lamina collapses into a degenerate two-dimensional problem.

Solvent with constant density, ρ_s, is transported in the liquid phase by both convection and diffusion. The convective solvent mass flux, $\vec{w}_c$, is due to gross fluid movement,

$$\vec{w}_c = \rho_s C\vec{u} \qquad 2.3(1)$$

with the volumetric fluid flux density, $\vec{u}$, as the apparent Darcy velocity.

In a flowing fluid, molecular diffusion in a porous medium is greatly enhanced by directional velocity dispersion. Dispersive behaviour is due to the interstitial inertia of diffusing species along tortuous capillary paths. For a point solvent source in a static fluid and homogeneous medium, Fickian diffusion results in the radial propagation of a spherical concentration front. Superposition of a velocity field deforms this spherical shell into an axisymmetric surface skewed towards the direction of flow, as illustrated in Figure 2.3-1.

The principal axis of dispersion coincides with the flow direction at every point in the flow field. An instantaneous local velocity frame $F_u\{x_i'\}$ can be defined by a longitudinal basis vector, $\hat{e}_1'$, which coincides with the flow direction and a transverse basis vector, $\hat{e}_2'$,

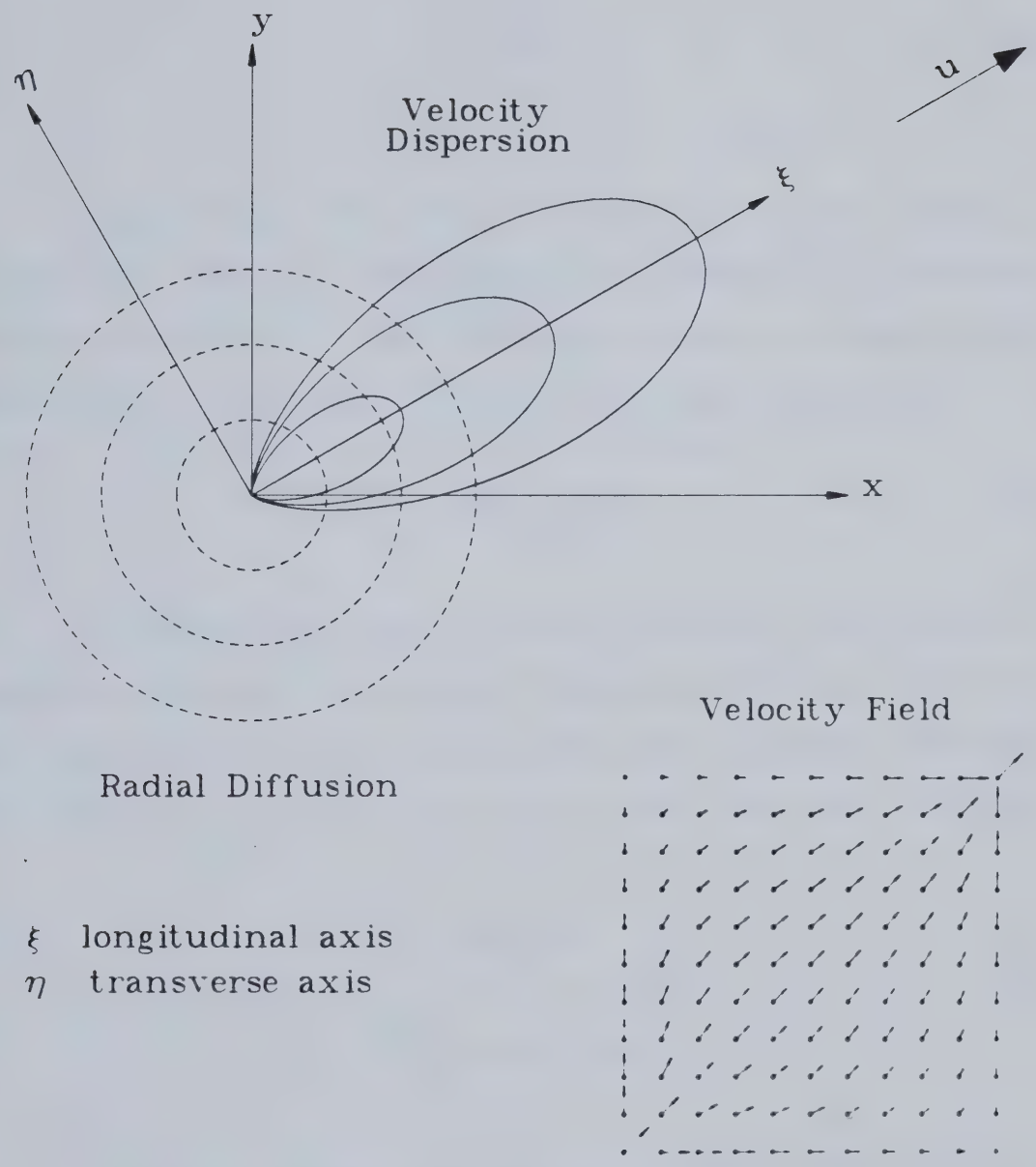


Figure 2.3-1 : Directional Dispersion

which is normal to the flow.

$$\left.\begin{aligned} \hat{e}'_1 &= \frac{\vec{u}}{|\vec{u}|} \\ \hat{e}'_1 \cdot \hat{e}'_2 &= 0 \end{aligned}\right\} \qquad 2.3(2)$$

In this frame, Fick's first law relates the apparent diffusion solvent mass flux, $\vec{w}_d$, to the concentration gradient by a diagonalized tensor of rank two, $\tilde{D}'$, whose consecutive elements correspond to the longitudinal and transverse diffusion coefficients, respectively.

$$\vec{w}_d = -\rho_s D'_{ii} \frac{\partial C}{\partial x'_i} \hat{e}'_i \qquad 2.3(3)$$

For moderate flow rates, Perkins and Johnston[37] find that the apparent longitudinal and transverse diffusion coefficients vary with the first power of the velocity magnitude. These apparent coefficients are determined in terms of total cross sectional areas for cgs units.

$$\left.\begin{aligned} D_\ell &= \frac{D_0}{F_r} + \frac{1}{2}\sigma d_p |\vec{u}| \\ D_t &= \frac{D_0}{F_r} + .0157\sigma d_p |\vec{u}| \end{aligned}\right\} \qquad 2.3(4)$$

The constant liquid phase molecular diffusion coefficient, D_0, is adjusted by the formation resistivity factor, F_r, to account for the tortuosity of the capillary network. The average particle diameter, d_p, is the grain size and σ is a measure of packing inhomogeneity.

The diffusion mass flux is invariant[38] of inertial reference frame and can equivalently be expressed in terms of the Cartesian

coordinate system.

$$\vec{w}_d = -\rho_s D_{ij} \frac{\partial C}{\partial x_j} \hat{e}_i \qquad 2.3(5)$$

The similarity transformation involves a rotation[39] through a velocity angle, θ,

$$\theta = \tan^{-1}\left(\frac{u_2}{u_1}\right) \qquad 2.3(6)$$

which determines the matrix of the cartesian tensor.

$$\begin{bmatrix} D_{11} & D_{12} \\ D_{21} & D_{22} \end{bmatrix} = \begin{bmatrix} D_\ell \cos^2\theta + D_t \sin^2\theta & (D_\ell - D_t)\cos\theta \sin\theta \\ (D_\ell - D_t)\cos\theta \sin\theta & D_\ell \sin^2\theta + D_t \cos^2\theta \end{bmatrix} \qquad 2.3(7)$$

Let $d\vec{\sigma}$ be a directed surface element on the closed surface, σ,

$$d\vec{\sigma} = \hat{n} d\sigma \qquad 2.3(8)$$

where $\hat{n}$ is an outward drawn unit vector normal to the surface element, $d\sigma$. The differential rate of solvent flow through this surface element is due to the combined effects of convective and diffusive transport mechanisms. The net rate of solvent outflow through the closed surface, σ, is the integral sum over all elements.

$$\oiint_\sigma (\vec{w}_c + \vec{w}_d) \cdot d\vec{\sigma} = \rho_s \oiint_\sigma \left[u_i C - D_{ij} \frac{\partial C}{\partial x_j}\right] \hat{e}_i \cdot \hat{n} d\sigma \qquad 2.3(9)$$

Conservation of solvent mass on the macroscopic scale equates the rate of solvent depletion from the combined solute-solution system

over the volume element to the net rate of solvent outflow through the bounding surface.

$$\frac{\partial}{\partial t}\left[\iiint_{\Delta V} \phi_m SC dv + \iiint_{R_s} C_s dv_s \right] = \oiint_{\sigma} \left(D_{ij} \frac{\partial C}{\partial x_j} - u_i C \right) \hat{e}_i \cdot \hat{n} d\sigma \qquad 2.3(10)$$

The total solvent content in the solute has contributions from all spheres in the volume element,

$$\iiint_{R_s} C_s dv_s = \iiint_{\Delta V} \left(N_p \int_0^{r_p} C_s r^2 dr \right) dv = \iiint_{\Delta V} \phi_m (1-S) \overline{C}_s dv \qquad 2.3(11)$$

and can equivalently be expressed in terms of a macroscopic volume-averaged solid-phase solvent concentration, $\overline{C}_s$.

$$\overline{C}_s = \frac{3}{r_p^3} \int_0^{r_p} C_s r^2 dr \qquad 2.3(12)$$

The volume element is stationary, allowing an interchange in the order of integration and differentiation.

$$\iiint_{\Delta V} \phi_m \frac{\partial}{\partial t} \left[SC + (1-S)\overline{C}_s \right] dV = \oiint_{\sigma} \left[D_{ij} \frac{\partial C}{\partial x_j} - u_i C \right] \hat{e}_i \cdot \hat{n} d\sigma \qquad 2.3(13)$$

The rate of solvent accumulation in the solute is related to the interphase solvent transfer by the dissolution equation 2.2(4), such that the integral form of the convective-diffusion with adsorption equation is expressed in terms of the dependent variables.

$$\iiint_{\Delta V} \left\{ \left(\phi_m - \frac{4\pi}{3} N_p r_p^3 \right) \frac{\partial C}{\partial t} + 4\pi N_p r_p^2 [\alpha(C-C^*)] \right\} dv$$

$$= \oint_{\sigma} \left[D_{ij} \frac{\partial C}{\partial x_j} - u_i C \right] \hat{e}_i \cdot \hat{n} d\sigma \qquad 2.3(14)$$

Application of the Divergence theorem,

$$\iiint_{\Delta V} \left\{ \left(\phi_m - \frac{4\pi}{3} N_p r_p^3 \right) \frac{\partial C}{\partial t} + 4\pi N_p r_p^2 [\alpha(C-C^*)] \right.$$

$$\left. - \frac{\partial}{\partial x_i} \left[D_{ij} \frac{\partial C}{\partial x_j} - u_i C \right] \right\} dv = 0 \qquad 2.3(15)$$

determines the differential form of the convective-diffusion with adsorption equation for all macroscopic points in R.

$$\frac{\partial}{\partial x_i} \left[D_{ij} \frac{\partial C}{\partial x_j} - u_i C \right] = \left(\phi_m - \frac{4\pi}{3} N_p r_p^3 \right) \frac{\partial C}{\partial t} + 4\pi N_p r_p^2 [\alpha(C-C^*)] \qquad 2.3(16)$$

2.4. Darcy-Continuity

Convection currents in the streaming solution are established by local pressure gradients within the porous region. The apparent velocity vector, $\vec{u}$, is the rate of gross fluid movement through a unit area normal to the direction of flow. With the assumption of sufficient capillarity and flow rates within the laminar regime, the velocity is related to the potential gradient by Darcy's law.

$$u_i = - \frac{k_{ij}}{\mu} \frac{\partial \Phi}{\partial x_j} \qquad 2.4(1)$$

Density variations are assumed small, such that the force

potential[40] per unit volume, Φ, is the combined hydrodynamic pressure, p, and the hydrostatic gravity head, ρgh.

$$\Phi = p + \rho gh \qquad 2.4(2)$$

The fluid density, ρ, is determined by the concentration weighted average of the component densities,

$$\rho = (\rho_s - \rho_o)C + \rho_o \qquad 2.4(3)$$

and g is the acceleration due to gravity.

The permeability tensor of rank two, $\tilde{k}$, is the conductance of the porous medium to gross fluid movement and is intrinsically dependent on the geometry of the local capillary networks. These networks give preferential directions to gross fluid movement. For convenience, the principal axes of the permeability trend are chosen to coincide with the coordinate axes.

Dissolution of the solid phase will create a porosity increase resulting in capillary enlargement and enhanced flow conductance. Similarity of capillary enlargement is assumed for the packed bed and the component permeabilities related analytically to the porosity by the Kozeny-Carman equation.[41]

$$k_i = k_{i_0} \frac{(1-\phi_0)^2 \phi^3}{\phi_0^3 (1-\phi)^2} \qquad 2.4(4)$$

The permeabilities, k_{i_0}, are measured at the reference porosity, ϕ_0.

The fluid viscosity, μ, is the fluid resistance to flow due to

internal cohesive forces. The viscosity is assumed to be independent of fluid inertia for the flow rates of the laminar regime and dependent only on molecular interaction.

For the solvent-bitumen system, the viscosity is related to the liquidity determined by the solvent concentration, component viscosities and densities using Cragoe's Method.[42] The method defines a liquidity, L, based on the viscosity measured in poise.

$$L(\mu) = \frac{1000 \ \ell n \ 20}{\ell n \ \mu - \ell n(5\times10^{-4})} \qquad 2.4(5)$$

The fluid liquidity is calculated by the mass-fractional weighted average of component liquidities,

$$L(\mu) = M_s L(\mu_s) + (1-M_s)L(\mu_o) \qquad 2.4(6)$$

with M_s as the solvent mass fraction.

$$M_s = \frac{\rho_s}{\rho} C \qquad 2.4(7)$$

The fluid viscosity is functionally dependent on the concentration, with parametric dependence on component properties.

$$\mu = \exp\left(\frac{a_1 C + b_1}{a_2 C + b_2}\right) \qquad 2.4(8)$$

$$a_1 = \left(1 - \frac{\rho_o}{\rho_s}\right) \ell n\ \mu_o\ \ell n\ \mu_s - \left[\ell n\ \mu_s - \frac{\rho_o}{\rho_s}\ \ell n\ \mu_o\right] \ell n(5\times10^{-4})$$

$$a_2 = \frac{\rho_o}{\rho_s}\ \ell n\ \mu_o \left[\ell n\ \mu_s - \ell n(5\times10^{-4})\right]$$

$$b_1 = \ell n\ \mu_o - \frac{\rho_o}{\rho_s}\ \ell n\ \mu_s - \left[1 - \frac{\rho_o}{\rho_s}\right] \ell n(5\times10^{-4}) \qquad 2.4(9)$$

$$b_2 = \frac{\rho_o}{\rho_s} \left[\ell n\ \mu_s - \ell n(5\times10^{-4})\right]$$

Although the individual fluid components are incompressible, there can be mass accumulation in the volume element as a result of porosity changes from dissolution, and density variations due to mixing. Dissolution of solid matter leads to the creation of fluid as a result of nonreversible phase changes. Conservation of fluid mass dictates the rate of mass accumulation over the volume element is a direct consequence of the mass inflow through the bounding surface, combined with the mass created from the internal fluid-generating source. The dissolution mass-source creates fluid with ambient density approximated by the local macroscopic average, at the rate of solute dissolution.

$$\frac{\partial}{\partial t} \iiint_{\Delta V} \rho\phi dv = - \oint\!\!\!\!\!\!\int_{\sigma} \rho\vec{u} \cdot \hat{n} d\sigma + \iiint_{\Delta V} \rho\ \frac{\partial \phi}{\partial t}\ dv \qquad 2.4(10)$$

The source effectively cancels fluid accumulation due to porosity changes, leading to the integral form of the continuity equation.

$$\iiint_{\Delta V} \phi\ \frac{\partial \rho}{\partial t}\ dv = - \oint\!\!\!\!\!\!\int_{\sigma} \rho\vec{u} \cdot \hat{n} d\sigma \qquad 2.4(11)$$

Applying the Divergence Theorem,

$$\iiint_{\Delta V} \left[\frac{\partial}{\partial x_i} (\rho u_i) + \phi \frac{\partial \rho}{\partial t} \right] dv = 0 \qquad 2.4(12)$$

determines the differential form of the continuity equation for all macroscopic points in R.

$$\frac{\partial}{\partial x_i} (\rho u_i) = -\phi \frac{\partial \rho}{\partial t} \qquad 2.4(13)$$

The combined Darcy-continuity equation,

$$\frac{\partial}{\partial x_i} \left\{ \frac{\rho k_i}{\mu} \frac{\partial}{\partial x_i} (p+\rho gh) \right\} = \phi_m \left(1 - \frac{4\pi}{3} N_p r_p^3 \right) \frac{\partial \rho}{\partial t} \qquad 2.4(14)$$

together with the convective-diffusion with adsorption equation 2.3(16) and the radial dissolution equation 2.2(9) constitute the coupled system of nonlinear equations for the state vector (p,C,r_p) whose closed form solution determines the evolution of the leaching process.

2.5. Boundary Conditions

A thin surface layer, $\sum$, of thickness δ separates the lamina R from all external points. External properties are generally different from those just within the porous interior, and solvent transmission is regulated across the surface layer. The interior of R is void of external fluid sources, such that the only introduction of fluid mass into the porous lamina is through the bounding perimeter.

There is no accumulation in the surface layer and the solvent influx from an external reservoir (+) balances the influx into the porous interior (-). Mass transport across the surface layer is normal to the bounding perimeter and all tangential fluxes vanish over $\sum$.

$$\left[u_i C - D_{ij} \frac{\partial C}{\partial x_j}\right]_{(+)} = \left[u_i C - D_{ij} \frac{\partial C}{\partial x_j}\right]_{(-)} ; \quad \hat{e}_i \cdot \hat{n} = 0, \; P(\vec{x}) \in \sum \qquad 2.5(1)$$

As a consequence of the normal velocity constraint, the off-diagonal elements of the cartesian diffusion tensor coefficient vanish, restricting cross diffusion to the interior.

$$D_{ij} = 0; \quad i \neq j \; , \; P(\vec{x}) \in \sum \qquad 2.5(2)$$

Three boundary types are considered for the two-dimensional rectangular lamina of dimension (L,W,Δz). The set of point and/or line sources, $\{\sum_{IN}\}$, constitute all fluid inlets on the perimeter. The set of sinks, $\{\sum_{OUT}\}$, constitute all outlets. The complementary set of points, neither inlet nor outlet, are impermeable $\{\sum_{NO\ FLOW}\}$.

The normal velocity components vanish at all impermeable points. Both concentration and pressure are continuous. Solvent transport is restricted. No solvent is allowed to diffuse in, or out, through any impermeable point. The normal components of the potential and concentration gradients vanish, with Neumann boundary conditions to satisfy the imposed impermeable constraint.

$$\frac{\partial \Phi}{\partial x_i} = \frac{\partial C}{\partial x_i} = 0; \quad \hat{e}_i \cdot \hat{n} = 0 \; , P(\vec{x}) \in \{\sum_{NO\ FLOW}\} \qquad 2.5(3)$$

Fluid is removed from the porous region at an outlet pressure, P_{OUT}. The outlet channel is designed to remove solvent with the outlet stream, and filter any solvent from diffusing back into the interior. The concentration is continuous over the outlet channel and the fluid velocity uniform. The normal component of the concentration gradient vanishes, such that solvent passes unidirectionally from the rectangular region to an isolated outlet reservoir sink. The fluid front is annihilated at the isolated outlet singularity, resulting in an external discontinuity within the velocity field.

$$\frac{\partial C}{\partial x_i} = \left.\frac{\partial u_i}{\partial x_i}\right|_{(-)} = 0; \quad P_{(-)} = P_{OUT}; \qquad \hat{e}_i \cdot \hat{n} = 0 \,, P(\vec{x}) \in \{\textstyle\sum_{OUT}\} \qquad 2.5(4)$$

Solvent of concentration C_{IN} is injected from an external source reservoir into the porous region through all inlet points at an inlet pressure, P_{IN}. Concentration gradients are established at the inlet surface as a result of the discontinuities in diffusive properties between the external and internal boundaries. Solvent diffusion from the external reservoir is regulated by selectively passing solvent unidirectionally into the interior. In this manner, the source reservoir remains isolated and is unaffected by the processes occurring within the porous region. Regulation is achieved by allowing solvent mass to accumulate on the external inlet surface at a rate proportional to the solvent diffusing into the interior.

$$\left[D_{ii}\,\frac{\partial C}{\partial x_i}\right]_{(+)} = \alpha_s \left[D_{ii}\,\frac{\partial C}{\partial x_i}\right]_{(-)}; \quad \hat{e}_i \cdot \hat{n} = 0 \,, P(\vec{x}) \in \{\textstyle\sum_{IN}\} \qquad 2.5(5)$$

The skin factor, α_s, is the constant of proportionality which determines the diffusion conductivity of the inlet surface. A fluid front is created at the isolated inlet singularity causing an external discontinuity in both velocity and concentration. The fluid velocity is assumed uniform within the inlet channel, and conservation of mass equates external to internal fluxes,

$$\left\{u_i C - D_{ii} \frac{\partial C}{\partial x_i}\right\}_{(+)} = \left\{u_{i_{(-)}} C_{IN} - \alpha_s \left[D_{ii} \frac{\partial C}{\partial x_i}\right]_{(-)}\right\}$$

$$= \left\{u_i C - D_{ii} \frac{\partial C}{\partial x_i}\right\}_{(-)} \qquad 2.5(6)$$

to give the inlet boundary conditions.

$$\left.\begin{aligned} \left.\frac{\partial C}{\partial x_i}\right|_{(-)} &= \frac{-u_i}{(1-\alpha_s)D_{ii}} \left[C_{IN} - C_{(-)}\right] \\ \left.\frac{\partial u_i}{\partial x_i}\right|_{(-)} &= 0; \quad p_{(-)} = p_{IN} \end{aligned}\right\}; \quad \hat{e}_i \cdot \hat{n} = 0 \,, \vec{P(x)} \in \{\Sigma_{IN}\} \qquad 2.5(7)$$

As the skin factor approaches unity, the inlet gives no resistance to solvent diffusion and the internal concentration approaches that of the external source. When the skin factor vanishes, the inlet becomes impermeable to diffusive transport and fluid of concentration C_{IN} is introduced into the interior by convection only.

CHAPTER THREE

SIMULATOR DEVELOPMENT

An overall numerical approach to the nonlinear system of integral and differential equations for solvent leaching of bitumen spheres is presented. The numerical solution for the state vector of fluid pressure, fluid phase solvent concentration and the fluid phase saturation using the method of successive substitution is outlined.

Central-differences on a regular mesh centered grid with a Crank Nicolson temporal discretization determines the finite difference analogs for the integral conservation laws. The time step is based on the incremental fractional pore volume of fluid injected at a constant flow rate, over each discrete injection interval. For line sources, the Newton-Raphson method iterates the inlet pressure necessary to maintain the designated flow rates. A mass balance check is used to monitor the differential and cumulative errors that may arise in the approximate solution to the overall system.

3.1. Central Differences

The rectangular region R of dimension $(L,W,\Delta z)$ is partitioned into a grid of N_x and N_y equidistant intervals in the x- and y- directions, respectively (cf. Figure 3.1-1). Each discrete mesh point P_{ij} has the coordinates (x_i,y_j),

$$\begin{aligned} x_i &= (i-1)\Delta x; \qquad i = 1,2,\ldots,N_x+1 \\ y_i &= (j-1)\Delta y; \qquad j = 1,2,\ldots,N_y+1 \end{aligned} \tag{3.1(1)}$$

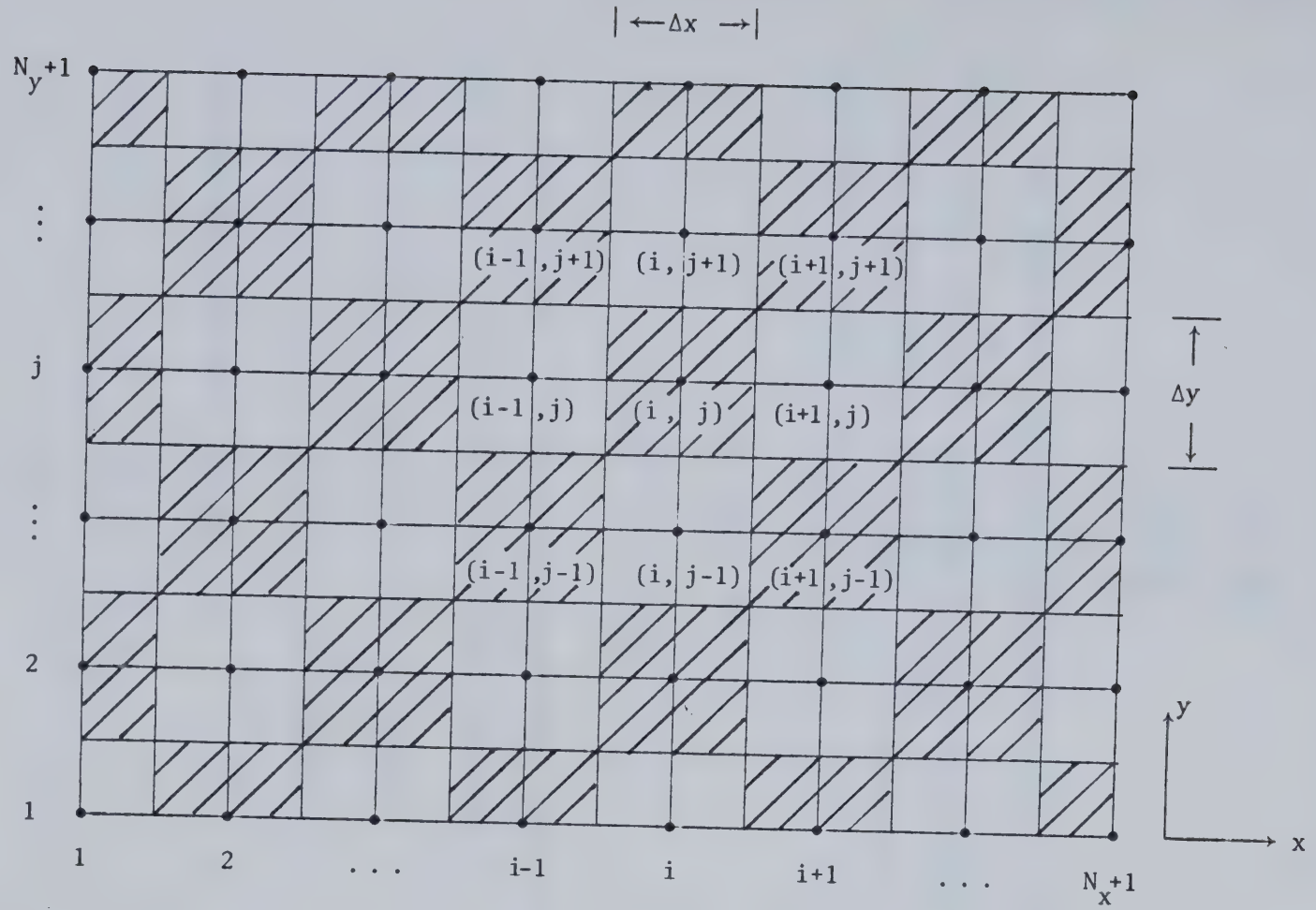


Figure 3.1-1 : The Mesh-Centered Grid

with the respective equidistant intervals, Δx and Δy.

$$\Delta x = \frac{L}{N_x}$$
$$\Delta y = \frac{W}{N_y} \qquad 3.1(2)$$

Each mesh point P_{ij} has an associated block of volume $\Delta V_{b_{ij}}$, whose bounding surface is determined by the vertical midplanes of height Δz lying between adjacent mesh points. The midpoints are fixed by their spatial arithmetic means.

$$x_{i+\frac{1}{2}} = \frac{1}{2}(x_i + x_{i+1})$$
$$y_{j+\frac{1}{2}} = \frac{1}{2}(y_j + y_{j+1}) \qquad 3.1(3)$$

Let i^* and j^* denote the corresponding faces of those volume elements which map onto the boundary perimeter, $\sum$.

$$i^*_+ = 1, \quad i^*_- = N_x + 1; \quad i^* \in \{i^*_+, i^*_-\}$$
$$j^*_+ = 1, \quad j^*_- = N_y + 1; \quad j^* \in \{j^*_+, j^*_-\} \qquad 3.1(4)$$

Each block has dimensions $(\Delta x_i, \Delta y_j, \Delta z)$,

$$\Delta x_i = \left\{ \begin{array}{ll} \frac{\Delta x}{2}; & i = i^* \\ \Delta x; & i \neq i^* \end{array} \right\}$$
$$\Delta y_i = \left\{ \begin{array}{ll} \frac{\Delta y}{2}; & j = j^* \\ \Delta y; & j \neq j^* \end{array} \right\} \qquad 3.1(5)$$

with cross sectional surface areas A_x, A_y and volume ΔV_b,

$$A_{x_j} = \Delta y_j \Delta z$$

$$A_{y_i} = \Delta x_i \Delta z \qquad 3.1(6)$$

$$\Delta V_{b_{ij}} = \Delta x_i \Delta y_j \Delta z$$

Consider the nine-point difference star centered about mesh point P_{ij} [cf. Figure 3.1-2]. Let $f(x,y)$ be any function which can be expressed by a Taylor series in the neighbourhood of P_{ij}. By expanding f about the adjacent midpoints, the central-difference approximations to the central first-order derivatives are obtained with second-order accuracy.

$$\left.\frac{\partial f}{\partial x}\right|_{i,j} = \frac{1}{\Delta x}\left(f_{i+\frac{1}{2},j} - f_{i-\frac{1}{2},j}\right) - 0(\Delta x^2)$$

$$\left.\frac{\partial f}{\partial y}\right|_{i,j} = \frac{1}{\Delta y}\left(f_{i,j+\frac{1}{2}} - f_{i,j-\frac{1}{2}}\right) - 0(\Delta y^2) \qquad 3.1(7)$$

Second-order derivatives are approximated to second-order accuracy with the successive application of the first-order difference. The adjacent mesh points are used in place of the midpoints to evaluate inner first-order differences to approximate the mixed partials.

$$\left.\frac{\partial}{\partial x}\left(\alpha_{xx}\frac{\partial f}{\partial x}\right)\right|_{i,j} = \frac{1}{\Delta x^2}\left\{\alpha_{xx_{i+\frac{1}{2},j}}\left(f_{i+1,j} - f_{i,j}\right) - \alpha_{xx_{i-\frac{1}{2},j}}\left(f_{i,j} - f_{i-1,j}\right)\right\} - 0(\Delta x^2)$$

$$\left.\frac{\partial}{\partial x}\left(\alpha_{xy}\frac{\partial f}{\partial y}\right)\right|_{i,j} = \frac{1}{4\Delta x \Delta y}\left\{\alpha_{xy_{i+\frac{1}{2},j}}\left[\left(f_{i+1,j+1}+f_{i,j+1}\right) - \left(f_{i+1,j-1}+f_{i,j-1}\right)\right] - \alpha_{xy_{i-\frac{1}{2},j}}\left[\left(f_{i,j+1}+f_{i-1,j+1}\right) - \left(f_{i,j-1}+f_{i-1,j-1}\right)\right]\right\}$$

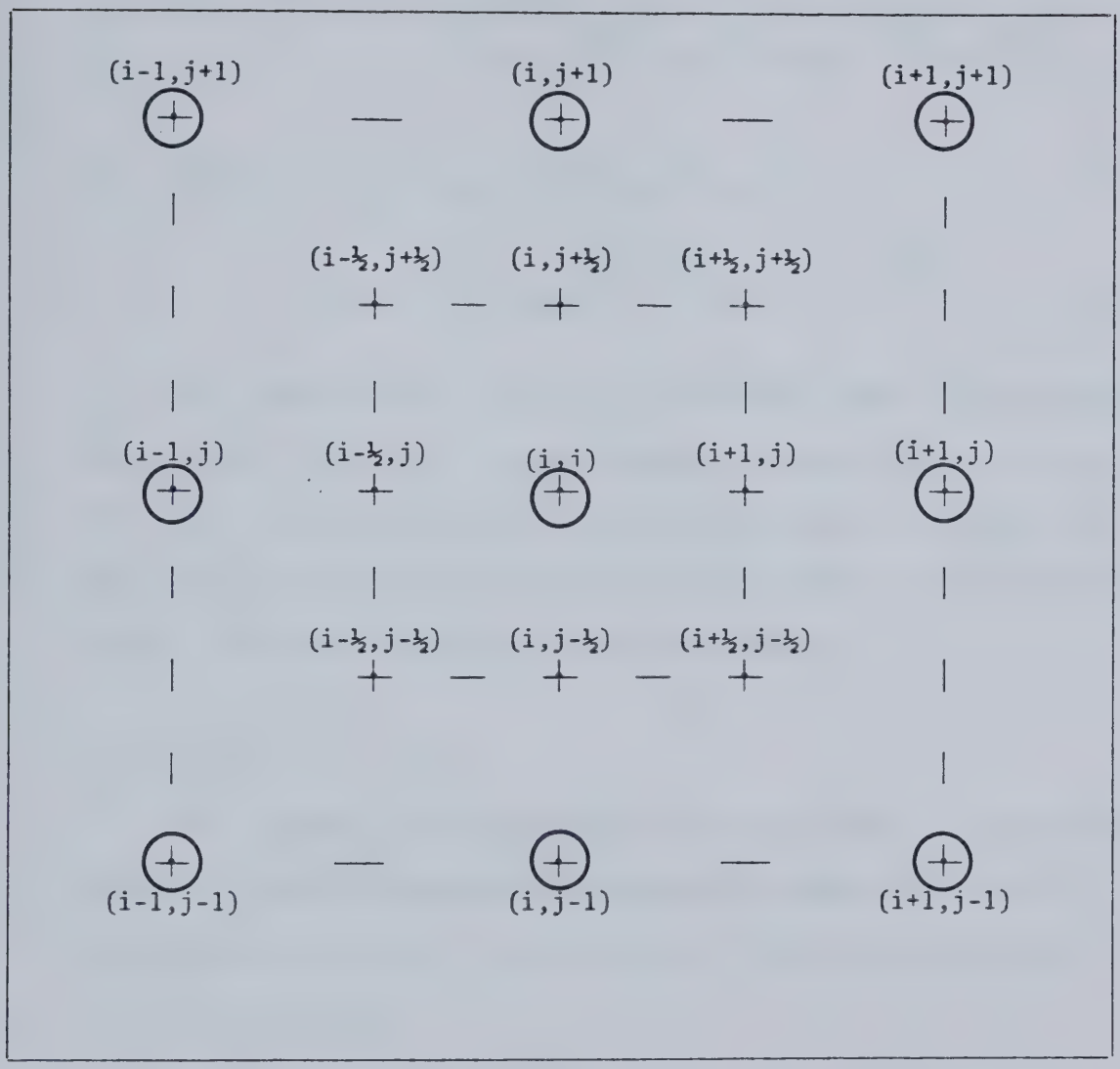


Figure 3.1-2 : The Nine-Point Difference-Star

$$\frac{\partial}{\partial y}\left(\alpha_{yx}\frac{\partial f}{\partial x}\right)\Big|_{i,j} = \frac{1}{4\Delta x\Delta y}\left\{\alpha_{yx_{i,j+\frac{1}{2}}}\left[\left(f_{i+1,j+1}+f_{i+1,j}\right)-\left(f_{i-1,j+1}+f_{i-1,j}\right)\right]\right.$$

$$\left.-\alpha_{yx_{i,j-\frac{1}{2}}}\left[\left(f_{i+1,j}+f_{i+1,j-1}\right)-\left(f_{i-1,j}+f_{i-1,j-1}\right)\right]\right\}$$

$$\frac{\partial}{\partial y}\left(\alpha_{yy}\frac{\partial f}{\partial y}\right)\Big|_{i,j} = \frac{1}{\Delta y^2}\left\{\alpha_{yy_{i,j+\frac{1}{2}}}\left(f_{i,j+1}-f_{i,j}\right)\right.$$

$$\left.-\alpha_{yy_{i,j-\frac{1}{2}}}\left(f_{i,j}-f_{i,j-1}\right)\right\} - O(\Delta y^2) \qquad 3.1(8)$$

The mixed partials arising from the cross terms of the diffusion tensor product are small, but nevertheless included in the analysis. Both first- and second-order pure partials are evaluated using only those points on the five-point sub-star, and thereby categorizing this central difference scheme as a five-point method.

3.2. Numerical Dispersion

The component convective fluxes can be expanded to second order accuracy at the bounding faces of the volume element. The spatial variation in solvent flow over the volume element approximates the convective derivative.

$$\frac{\partial}{\partial x}\left(u_x C\right)\Big|_{i,j} = \frac{1}{\Delta x}\left[u_{x_{i+\frac{1}{2},j}}C_{i+\frac{1}{2},j} - u_{x_{i-\frac{1}{2},j}}C_{i-\frac{1}{2},j}\right] \qquad 3.2(1)$$

All dependent variables must be expressed in terms of the mesh points, and to the same order of accuracy, the mid-concentrations are replaced by their spatial averages.

$$\frac{\partial}{\partial x}\left(u_x C\right)\Big|_{i,j} = \frac{1}{2\Delta x}\left[u_{x_{i+\frac{1}{2},j}}\left(C_{i+1,j}+C_{i,j}\right) - u_{x_{i-\frac{1}{2},j}}\left(C_{i,j}+C_{i-1,j}\right)\right] \qquad 3.2(2)$$

A clever regrouping of the central difference approximation isolates an upstream weighted component.

$$\frac{\partial}{\partial x}(u_x C)_{i,j} = \frac{1}{\Delta x}\left[u_{x_{i+\frac{1}{2},j}} C_{i,j} - u_{x_{i-\frac{1}{2},j}} C_{i-1,j}\right]$$

$$+ \frac{1}{\Delta x^2}\left[u_{x_{i+\frac{1}{2},j}} \frac{\Delta x}{2}(C_{i+1,j} - C_{i,j})\right.$$

$$\left. - u_{x_{j-\frac{1}{2},j}} \frac{\Delta x}{2}(C_{i,j} - C_{i-1,j})\right] \qquad 3.2(3)$$

The numerical dispersion counterpart is termed accordingly for its similarity in form to the central difference approximation of the diffusion derivative. Chaudhari[13] obtains this numerical dispersion term directly from a second-order correct upstream-weighted discretization.

Even though central differences and second-order correct upstream-weighting give identical discretizations, the latter form will be adopted to accentuate the smearing of truncation errors that may arise from first-order correct methods, and quantify these errors with a physically analogous dispersive mechanism. One should keep in mind that second-order correct methods also have truncation error, and the weighted combinations of these higher order derivatives will produce numerical distortions to some degree.

3.3. Time Integration

The time domain is partitioned into sufficiently many irregular intervals to determine the required leaching history of the miscible

flood. Each time step, Δt, with respective upper and lower bounds t^{n+1} and t^{n}, is based on the incremental fractional pore volume, ΔPV, of fluid injected at a constant injection rate, q_{IN}.

$$\Delta t_{n+\frac{1}{2}} = \left(\frac{\phi_m LW\Delta z}{q_{IN}} \right) \Delta PV_{n+\frac{1}{2}} \qquad 3.3(1)$$

Consider a nonlinear differential equation with the form,

$$\frac{\partial f}{\partial t} = G(\gamma f) \qquad 3.3(2)$$

where γ, f and G are any functions expressible by a Taylor series about a discrete point in time. Numerical integration may be performed using a number of techniques, ranging from high-order Runga Kutta methods demanding many points for Lagrangian interpolation, to Riemann sums using two-point rules. Both midpoint and trapezoid rules give the same order of accuracy as central differences, and require a minimal amount of computation to evaluate.

Integration over the time step using the trapezoid rule for the right hand side of 3.3(2) gives:

$$(f^{n+1}-f^{n}) = \frac{1}{2} [G(\gamma^{n+1}f^{n+1}) + G(\gamma^{n}f^{n})]\Delta t_{n+\frac{1}{2}} \qquad 3.3(3)$$

In comparison, the midpoint rule preserves the nonlinearity,

$$(f^{n+1}-f^{n}) = G(\gamma^{n+\frac{1}{2}}f^{n+\frac{1}{2}})\Delta t_{n+\frac{1}{2}} \qquad 3.3(4)$$

but requires interpolation to evaluate mid-time values. To the same order of accuracy, linear interpolation of the dependent variable relates

the mid-time value to its neighbouring nodes.

$$(f^{n+1}-f^{n}) = G\left(\frac{\gamma^{n+\frac{1}{2}}}{2}\,[f^{n+1}+f^{n}]\right)\Delta t_{n+\frac{1}{2}} \qquad 3.3(5)$$

This midpoint approach assumes that only the dependent variables are piecewise linear, whereas the trapezoid rule averages the non-linearity. The author feels that the midpoint rule tracks the non-linearity more effectively while requiring less work in evaluating a single mid-time coefficient.

The simulator in discussion adopts this midpoint weighting for the temporal discretization of the governing nonlinear system of leaching equations.

The integro-differential radial dissolution equation [2.2(9)] is discretized over the time step to give:

$$C^{*}\left\{\left[r_{0}F^{n+1} + \int_{0}^{t^{n+1}} \dot{r}_{p}(\tau)F(t-\tau)d\tau\right] - \left[r_{o}F^{n} + \int_{0}^{t^{n}} \dot{r}_{p}(\tau)F(t-\tau)d\tau\right]\right\}$$
$$= \left(\frac{r_{p}^{n+1}+r_{p}^{n}}{2}\right)^{2}\left\{\left(\frac{C^{n+1}+C^{n}}{2}\right)\left(\frac{r_{p}^{n+1}-r_{p}^{n}}{\Delta t_{n+\frac{1}{2}}}\right) + \alpha^{n+\frac{1}{2}}\left[\left(\frac{C^{n+1}+C^{n}}{2}\right) - C^{*}\right]\right\}\Delta t_{n+\frac{1}{2}} \qquad 3.3(6)$$

The convective-diffusion with adsorption equation [2.3(16)] in compact tensor notation is temporally discretized to yield:

$$\frac{\partial}{\partial x_{i}}\left\{D_{ij}^{n+\frac{1}{2}}\frac{\partial}{\partial x_{j}}\left(\frac{C^{n+1}+C^{n}}{2}\right) - u_{i}^{n+\frac{1}{2}}\left(\frac{C^{n+1}+C^{n}}{2}\right)\right\}$$
$$= \left[\phi_{m} - \frac{4\pi}{3}N_{p}\left(\frac{r_{p}^{n+1}+r_{p}^{n}}{2}\right)^{3}\right]\left(\frac{C^{n+1}-C^{n}}{\Delta t_{n+\frac{1}{2}}}\right) + 4\pi N_{p}\left(\frac{r_{p}^{n+1}+r_{p}^{n}}{2}\right)^{2}\left[\alpha^{n+\frac{1}{2}}\left(\frac{C^{n+1}+C^{n}}{2}\right) - C^{*}\right] \qquad 3.3(7)$$

Midtime pressures are implicitly evaluated in order to directly calculate the midtime convective-diffusion coefficients. The temporally discretized Darcy-continuity equation 2.4(14) has the form:

$$\frac{\partial}{\partial x_i}\left\{\left(\frac{\rho k_i}{\mu}\right)^{n+\frac{1}{2}} \frac{\partial}{\partial x_i}\left[p^{n+\frac{1}{2}} + \rho^{n+\frac{1}{2}} gh\right]\right\}$$

$$= \phi_m \left[1 - \frac{4\pi}{3} N_p \left(\frac{r_p^{n+1} + r_p^n}{2}\right)^3\right]\left(\frac{\rho^{n+1} - \rho^n}{\Delta t_{n+\frac{1}{2}}}\right) \qquad 3.3(8)$$

with velocity components evaluated at the mid-times.

$$u_i^{n+\frac{1}{2}} = -\left(\frac{k_i}{\mu}\right)^{n+\frac{1}{2}} \frac{\partial}{\partial x_i}\left[p^{n+\frac{1}{2}} + \rho^{n+\frac{1}{2}} gh\right] \qquad 3.3(9)$$

3.4. The Associated Difference Equation for Particle Radius

Time levels have been established for discretization of the radial dissolution equation in 3.3(6). The convolution integral is approximated by a Reimann sum using the extended mid-point rule.

$$\int_0^{t^{n+1}} \dot{r}_p(\tau) F(t-\tau)\, d\tau = \sum_{k=0}^{n} (r_p^{k+1} - r_p^k) F(t^{n+1} - t^{k+\frac{1}{2}}) \qquad 3.4(1)$$

An interpolation scheme is constructed for the evaluation of the discrete convolution kernal, F^m, at times, t^m, that do not coincide with the given time nodes $\{t^k;\ k = 1,n+1\}$. A search is executed through the set of time nodes to find the interval (t^k, t^{k+1}) which includes t^m. The corresponding radius r_p^m is linearly interpolated within this interval and consequently used to calculate F^m.

$$F^m = (r_p^m)^2 \left[\frac{1}{3} - \frac{2}{\pi^2} \sum_{k=1}^{\infty} \frac{e^{-k^2\pi^2 D_s t^m/(r_p^m)^2}}{k^2} \right] \qquad 3.4(2)$$

The particle radius is the volume average over the volume element $\Delta V_{b_{ij}}$ and may vary spatially from element to element. The discrete version of the radial dissolution equation for each element is:

$$C^*\Big\{r_0(F^{n+1}-F^n) + \sum_{k=0}^{n} [(r_p^{k+1}-r_p^k)F(t^{n+1}-t^{k+\frac{1}{2}})] - \sum_{k=0}^{n-1} [(r_p^{k+1}-r_p^k)F(t^n-t^{k+\frac{1}{2}})]\Big\}_{i,j}$$

$$= \Big\{(r_p^{n+\frac{1}{2}})^2[C^{n+\frac{1}{2}}(r_p^{n+1}-r_p^n) + \alpha^{n+\frac{1}{2}}(C^{n+\frac{1}{2}}-C^*)\Delta t_{n+\frac{1}{2}}\Big\}_{i,j} \qquad 3.4(3)$$

Isolating for the new particle radius, r_p^{n+1}, gives the associated difference equation for radial dissolution, with the standard form:

$$E_{ij} r_{p_{ij}}^{n+1} = Q_{ij} \qquad 3.4(4)$$

and associated coefficients,

$$E_{ij} = [C^{n+\frac{1}{2}}(r_p^{n+\frac{1}{2}})^2 - C^*F(t^{n+1}-t^{n+\frac{1}{2}})]_{i,j}$$

$$Q_{ij} = \Big\{C^*\Big[r_0(F^{n+1}-F^n) + \sum_{k=0}^{n-1} (r_p^{k+1}-r_p^k)[F(t^{n+1}-t^{k+\frac{1}{2}})-F(t^n-t^{k+\frac{1}{2}})] - r_p^n F(t^{n+1}-t^{n+\frac{1}{2}})\Big] + (r_p^{n+\frac{1}{2}})^2[C^{n+\frac{1}{2}}r_p^n - \alpha^{n+\frac{1}{2}}(C^{n+\frac{1}{2}}-C^*)\Delta t_{n+\frac{1}{2}}]\Big\}_{i,j}$$

3.4(5)

Iterative techniques must be used to solve the highly nonlinear algebraic equation for the particle radius. The summations of F require many terms for convergence. Caution must be excersized as the dependent variables approach zero, for the equation becomes singular. Dissolution is nonreversible and must terminate at the zero radius, and hence the integro-differential equation is valid only while solid material exists. Once dissolution is complete, a zero radius must prevail.

$$r_{p_{ij}}^{n+1} \geq 0 \qquad 3.4(6)$$

3.5. The Associated Difference Equation for Pressure

The specified boundary conditions will fix an inlet pressure on the perimeter to produce the desired injection rate. Flow rates are monitored at the block boundaries over each element by the integral form of the Darcy-continuity equation. The mass flow transmissibility between adjacent mesh points determines inter-block fluid transmission across common elemental faces. With the time levels established in equation 3.3(8), the central-differenced Darcy-continuity equation has the integral form:

$$\left\{ T_{x_{i+\frac{1}{2},j}} (\Phi_{i+1,j} - \Phi_{i,j}) - T_{x_{i-\frac{1}{2},j}} (\Phi_{i,j} - \Phi_{i-1,j}) + T_{y_{i,j+\frac{1}{2}}} (\Phi_{i,j+1} - \Phi_{i,j}) - T_{y_{i,j-\frac{1}{2}}} (\Phi_{i,j} - \Phi_{i,j-1}) \right\}^{n+\frac{1}{2}}$$

$$= \left\{ \phi_m \left[1 - \frac{4\pi}{3} N_p (r_p^{n+\frac{1}{2}})^3 \right] (\rho^{n+1} - \rho^n) \right\}_{i,j} \frac{\Delta V_{b_{ij}}}{\Delta t_{n+\frac{1}{2}}} \qquad 3.5(1)$$

where both fluid mobility and grid dimension determine the flow transmissibility.

$$T^{n+\frac{1}{2}}_{x_{i+\frac{1}{2},j}} = \frac{A_{x_j}}{\Delta x}\left(\frac{\rho k_x}{\mu}\right)^{n+\frac{1}{2}}_{i+\frac{1}{2},j}$$

$$T^{n+\frac{1}{2}}_{y_{i,j+\frac{1}{2}}} = \frac{A_{y_i}}{\Delta y}\left(\frac{\rho k_y}{\mu}\right)^{n+\frac{1}{2}}_{i,j+\frac{1}{2}} \qquad 3.5(2)$$

The associated difference equation for pressure at each mesh point has the standard form:

$$B_{ij}p^{n+\frac{1}{2}}_{i,j-1} + D_{ij}p^{n+\frac{1}{2}}_{i-1,j} + E_{ij}p^{n+\frac{1}{2}}_{ij} + F_{ij}p^{n+\frac{1}{2}}_{i+1,j} + H_{ij}p^{n+\frac{1}{2}}_{i,j+1} = Q_{ij} \qquad 3.5(3)$$

with the associated scalar coefficients,

$$B_{ij} = T^{n+\frac{1}{2}}_{y_{i,j-\frac{1}{2}}}$$

$$D_{ij} = T^{n+\frac{1}{2}}_{x_{i-\frac{1}{2},j}}$$

$$F_{ij} = T^{n+\frac{1}{2}}_{x_{i+\frac{1}{2},j}}$$

$$H_{ij} = T^{n+\frac{1}{2}}_{y_{i,j+\frac{1}{2}}}$$

$$E_{ij} = -(B_{ij} + D_{ij} + F_{ij} + H_{ij})$$

$$Q_{ij} = \frac{\Delta V_{b_{ij}}}{\Delta t_{n+\frac{1}{2}}}\left\{\phi_m\left[1 - \frac{4\pi}{3}N_p(r_p^{n+\frac{1}{2}})^3\right](\rho^{n+1} - \rho^n)\right\}_{i,j}$$

$$- g\left\{B_{ij}(\rho^{n+\frac{1}{2}}h)_{i,j-1} + D_{ij}(\rho^{n+\frac{1}{2}}h)_{i-1,j} + E_{ij}(\rho^{n+\frac{1}{2}}h)_{ij}\right.$$

$$\left. + F_{ij}(\rho^{n+\frac{1}{2}}h)_{i+1,j} + H_{ij}(\rho^{n+\frac{1}{2}}h)_{i,j+1}\right\} \qquad 3.5(4)$$

Special consideration is given to the mesh points which map onto the bounding perimeter, $\sum$. If no inlet fluid sources, or outlet fluid sinks, are specified at the perimeter block, then the face which maps onto the perimeter is impermeable to flow. Reflection conditions, using fictitious points outside the physical region, are constructed from the finite difference analogs of the differential impermeable boundary conditions.

$$\left.\frac{\partial \Phi}{\partial x}\right|_{i^*,j} = 0 \Rightarrow \Phi_{i^*+1,j} = \Phi_{i^*-1,j}\,; \qquad P_{i^*j} \in \{\textstyle\sum_{\text{NO FLOW}}\}$$

$$\left.\frac{\partial \Phi}{\partial y}\right|_{i,j^*} = 0 \Rightarrow \Phi_{i,j^*+1} = \Phi_{i,j^*-1}\,; \qquad P_{ij^*} \in \{\textstyle\sum_{\text{NO FLOW}}\} \qquad 3.5(5)$$

Identical algebraic expressions are obtained for the integral difference form by constraining the corresponding fluid mass transmissibilities, and consequently the associated difference coefficients, to vanish.

$$\begin{aligned} T^{n+\frac{1}{2}}_{x_{i^*\pm\frac{1}{2},j}} &= 0\,; \qquad P_{i^*j} \in \{\textstyle\sum_{\text{NO FLOW}}\} \\ T^{n+\frac{1}{2}}_{y_{i,j^*\pm\frac{1}{2}}} &= 0\,; \qquad P_{ij^*} \in \{\textstyle\sum_{\text{NO FLOW}}\} \end{aligned} \qquad 3.5(6)$$

If a fluid outlet is specified, the corresponding point and subsequently the outlet block is maintained at the outlet pressure.

$$P^{n+\frac{1}{2}}_{ij} = P_{OUT}\,; \qquad P_{ij} \in \{\textstyle\sum_{OUT}\} \qquad 3.5(7)$$

The outlet condition, expressed in standard form, forces all coefficients

except the central ones to vanish.

$$E_{ij} = 1 \quad ; \quad P_{ij} \in \{\sum_{OUT}\} \qquad 3.5(8)$$
$$Q_{ij} = P_{OUT}$$

The discrete Newton-Raphson method is used to iterate midtime inlet pressures required to sustain constant injection rates for line sources. A line source is any succession of consecutive inlet mesh points, with a minimum restricted to two. The inlet faces of these consecutive blocks fuse to allow fluid injection over their combined length. Inlet pressure is constant. The fluid flux need not be uniform over the line source, however the piecewise sum of individual rates is required to total the specified injection rate. Pressure iterates are obtained from an initial guess and flow rates calculated. The change in pressure with respect to the change in flow rate is approximated by a backward difference, and the required inlet pressure converges within a few iterations.

$$P_{IN_{k+1}} = P_{IN_k} - \left[\frac{q_k - q_{IN}}{q_k - q_{k-1}}\right]\left(P_{IN_k} - P_{IN_{k-1}}\right) \qquad 3.5(9)$$

The associated coefficients for each inlet point on the line source are set to:

$$E_{ij} = 1 \quad ; \quad P_{ij} \in \{\sum_{IN}\} \qquad 3.5(10)$$
$$Q_{ij} = P_{IN_{k+1}}^{n+\frac{1}{2}}$$

with k as the Newton-Raphson iteration index.

No such iteration is necessary for an isolated point source. The perimeter faces of the point inlet become impermeable and a mass source term equal to the fluid injected at the specified rate is included on the right hand side of the Darcy-continuity equation, 3.5(1).

Discretization has quantized the dependent variables both spatially and temporally, such that the step discontinuities at the block boundaries and mid-time levels have been linearly averaged out. Nonlinearities stem from the implicit dependence of the mobility on both fluid concentration and saturation. Mid-time mobilities evaluated at the midpoints are subject to both spatial and temporal discontinuity. Averaging techniques must be used to weight implicit dependence to existing mesh points and time nodes. Such techniques as upstream or downstream weighting, and arithmetic or harmonic means, evaluated ahead or back in time, may be considered. Each will produce different results for different degrees of nonlinearity, and one must numerically experiment to obtain the most suitable weighting.

3.6. Associated Difference Equation for Concentration

The pressure field, implicitly evaluated at the mid-time, has a deliberate phase lag of half a time step in order to directly calculate the mid-time velocities. The scalar potential field is well defined at these mid-time nodes and the normal velocity components at the bounding faces of the volume element are readily obtained using the central-differenced Darcy's law.

$$u^{n+\frac{1}{2}}_{x_{i+\frac{1}{2},j}} = -\frac{1}{\Delta x}\left(\frac{k_x}{\mu}\right)^{n+\frac{1}{2}}_{i+\frac{1}{2},j}\left[\Phi^{n+\frac{1}{2}}_{i+1,j} - \Phi^{n+\frac{1}{2}}_{i,j}\right] \qquad 3.6(1)$$

Even though the normal velocity components are defined at the bounding faces, the tangential components may be discontinuous as a result of spatial quantization. To avoid slippage along these numerical boundaries, the tangential components must be single-valued. Both velocity components are defined at the mesh points, allowing a simple arithmetic mean to relate the central components to those at the peripheral faces.

$$\begin{aligned} u_{x_{ij}} &= \frac{1}{2}\left(u_{x_{i+\frac{1}{2},j}} + u_{x_{i-\frac{1}{2},j}}\right) \\ u_{y_{ij}} &= \frac{1}{2}\left(u_{y_{i,j+\frac{1}{2}}} + u_{y_{i,j-\frac{1}{2}}}\right) \end{aligned} \qquad 3.6(2)$$

Velocity angles and magnitudes follow directly.

$$\begin{aligned} u_{ij} &= \sqrt{u^2_{x_{ij}} + u^2_{y_{ij}}} \\ \theta_{ij} &= \tan^{-1}\left(\frac{u_{y_{ij}}}{u_{x_{ij}}}\right) \end{aligned} \qquad 3.6(3)$$

Cartesian diffusion coefficients are implicitly dependent on both velocity angle and magnitude, introducing further nonlinearity into the system. As with the mobilities, the diffusivities at the bounding faces must be spatially averaged to weight implicit dependence to existing mesh points.

$$D_{xx}{}^{n+\frac{1}{2}}_{i+\frac{1}{2},j} = D_{xx}(u^{n+\frac{1}{2}}_{i+\frac{1}{2},j}, \theta^{n+\frac{1}{2}}_{i+\frac{1}{2},j}) \qquad 3.6(4)$$

The midpoint velocity angles and magnitudes can be evaluated using similar upstream, downstream or arithmetic spatial weightings, as mentioned previously.

Analogous to the mass flow transmissibility, the solvent diffusivity controls the solvent transmission by normal Fickian diffusion.

$$(DFS)^{n+\frac{1}{2}}_{x_{i+\frac{1}{2},j}} = \frac{A_{x_j}}{\Delta x}\left(D_{xx}{}^{n+\frac{1}{2}}_{i+\frac{1}{2},j}\right) \qquad 3.6(5)$$

The numerical dispersivities follow from the central-differenced convection term,

$$(NMR)^{n+\frac{1}{2}}_{x_{i+\frac{1}{2},j}} = \frac{A_{x_j}}{\Delta x}\left(\frac{\Delta x}{2}\, u^{n+\frac{1}{2}}_{x_{i+\frac{1}{2},j}},\right) \qquad 3.6(6)$$

with the convection transmissibilities as the interblock fluid flow rates.

$$(CNV)^{n+\frac{1}{2}}_{x_{i+\frac{1}{2},j}} = A_{x_j}\left(u^{n+\frac{1}{2}}_{x_{i+\frac{1}{2},j}}\right) \qquad 3.6(7)$$

Cross dispersion, as a result of the off-diagonal terms of the diffusion tensor product, determines the transverse solvent diffusion tangential to the bounding elemental faces.

$$(CRS)^{n+\frac{1}{2}}_{x_{i+\frac{1}{2},j}} = \frac{A_{x_j}}{4\Delta y}\left\{D_{xy}{}^{n+\frac{1}{2}}_{i+\frac{1}{2},j}\left[(C^{n+\frac{1}{2}}_{i+1,j+1}+C^{n+\frac{1}{2}}_{i,j+1}) - (C^{n+\frac{1}{2}}_{i+1,j-1}+C^{n+\frac{1}{2}}_{i,j-1})\right]\right\} \qquad 3.6(8)$$

$$(CRS)^{n+\frac{1}{2}}_{y_{i,j+\frac{1}{2}}} = \frac{A_{y_i}}{4\Delta x}\left\{D_{yx}{}^{n+\frac{1}{2}}_{i,j+\frac{1}{2}}\left[(C^{n+\frac{1}{2}}_{i+1,j+1}+C^{n+\frac{1}{2}}_{i+1,j}) - (C^{n+\frac{1}{2}}_{i-1,j+1}+C^{n+\frac{1}{2}}_{i-1,j})\right]\right\}$$

With the time levels established in equation 3.3(7), the central-differenced convective-diffusion with adsorption equation has the integral form:

$$\left\{[(DFS)_x-(NMR)_x]_{i+\frac{1}{2},j}(C_{i+1,j}-C_{i,j}) - (CNV)_{x_{i+\frac{1}{2},j}} C_{ij} + (CRS)_{x_{i+\frac{1}{2},j}}\right\}^{n+\frac{1}{2}}$$

$$- \left\{[(DFS)_x-(NMR)_x]_{i-\frac{1}{2},j}(C_{i,j}-C_{i-1,j}) - (CNV)_{x_{i-\frac{1}{2},j}} C_{i-1,j} + (CRS)_{x_{i-\frac{1}{2},j}}\right\}^{n+\frac{1}{2}}$$

$$+ \left\{[(DFS)_y-(NMR)_y]_{i,j+\frac{1}{2}}(C_{i,j+1}-C_{i,j}) - (CNV)_{y_{i,j+\frac{1}{2}}} C_{i,j} + (CRS)_{y_{i,j+\frac{1}{2}}}\right\}^{n+\frac{1}{2}}$$

$$- \left\{[(DFS)_y-(NMR)_y]_{i,j-\frac{1}{2}}(C_{i,j}-C_{i,j-1}) - (CNV)_{y_{i,j-\frac{1}{2}}} C_{i,j-1} + (CRS)_{y_{i,j-\frac{1}{2}}}\right\}^{n+\frac{1}{2}}$$

$$= \Delta V_{b_{ij}} \left\{\overline{\left[\phi_m - \frac{4\pi}{3} N_p (r_p^{n+\frac{1}{2}})^3\right] (\frac{\partial C}{\partial t})^{n+\frac{1}{2}}} + 4\pi N_p (r_p^{n+\frac{1}{2}})^2 [\alpha^{n+\frac{1}{2}}(C^{n+\frac{1}{2}} - C^*)]\right\}_{i,j}$$

3.6(9)

The central accumulation term is spatially weighted over the five-point difference-star in order to cancel a portion of the convective truncation error.

$$\overline{(\phi \frac{\partial C}{\partial t})}\Big|_{ij}^{n+\frac{1}{2}} = \frac{1}{\Delta t_{n+\frac{1}{2}}} \left\{(1-w_1-w_2)\phi_{ij}^{n+\frac{1}{2}}[C_{ij}^{n+1}-C_{ij}^n]\right.$$

$$+ \frac{w_1}{2}\left[\phi_{i+1,j}^{n+\frac{1}{2}}(C_{i+1,j}^{n+1}-C_{i+1,j}^n)+\phi_{i-1,j}^{n+\frac{1}{2}}(C_{i-1,j}^{n+1}-C_{i-1,j}^n)\right]$$

$$\left. + \frac{w_2}{2}\left[\phi_{i,j+1}^{n+\frac{1}{2}}(C_{i,j+1}^{n+1}-C_{i,j+1}^n)+\phi_{i,j-1}^{n+\frac{1}{2}}(C_{i,j-1}^{n+1}-C_{i,j-1}^n)\right]\right\}$$

3.6(10)

The truncation cancellation procedure, effective when convection dominates, determines the optimal weights (w_1,w_2) which minimize the

combined convective and weighted accumulation truncation errors. The combined error, consisting of third-order mixed partials, is transformed into the velocity frame, where the derived weights suppress a dominant longitudinal error term. Appendix B gives a detailed derivation in which these weights are analytically determined for a direct solution scheme.

$$w_1 = \frac{1}{3}\left[\cos^2\theta + \frac{1}{2}\left(\frac{u\Delta t}{\phi\Delta x}\right)^2\right]^{n+\frac{1}{2}}_{i,j}$$

$$w_2 = \frac{1}{3}\left[\sin^2\theta + \frac{1}{2}\left(\frac{u\Delta t}{\phi\Delta y}\right)^2\right]^{n+\frac{1}{2}}_{i,j} \qquad 3.6(11)$$

In comparison, Laumbach[17] determines

$$w_1 = \frac{1}{3}\left[1 + \frac{1}{2}\left(\frac{u_x\Delta t}{\phi\Delta x}\right)^2\right]^{n+\frac{1}{2}}_{i,j}$$

$$w_2 = \frac{1}{3}\left[1 + \frac{1}{2}\left(\frac{u_y\Delta t}{\phi\Delta y}\right)^2\right]^{n+\frac{1}{2}}_{i,j} \qquad 3.6(12)$$

for an alternating direction implicit (ADI) procedure.

The truncation cancellation procedure is limited to a maximum time step determined from a stability analysis in Appendix B.

$$(w_1 + w_2) \leq \frac{1}{2}$$

$$\Delta t_{max} = \left\{\frac{\phi}{u}\left(\frac{\Delta x\Delta y}{\sqrt{\Delta x^2+\Delta y^2}}\right)\right\}^{n+\frac{1}{2}}_{ij} \qquad 3.6(13)$$

Truncation cancellation assumes neglible diffusion and adsorption, such that these weights are mainly applicable to the

convective dominat problems associated with miscible displacement. By setting both weights to zero, the proposed discretization collapses to a second-order correct central-difference scheme, applicable to the more general class of leaching problems.

The resulting associated difference equation for concentration has the standard form:

$$B_{ij}C^{n+1}_{i,j-1} + D_{ij}C^{n+1}_{i-1,j} + E_{ij}C^{n+1}_{ij} + F_{ij}C^{n+1}_{i+1,j} + H_{ij}C^{n+1}_{i,j+1} = Q_{ij} \qquad 3.6(14)$$

with the associated difference coefficients,

$$B_{ij} = -\frac{1}{2}\left[(DFS)_y-(NMR)_y+(CNV)_y\right]^{n+\frac{1}{2}}_{i,j-\frac{1}{2}} + \frac{w_2}{2}\frac{\phi^{n+\frac{1}{2}}_{i,j-1}}{\Delta t_{n+\frac{1}{2}}}\Delta V_{b_{ij}}$$

$$D_{ij} = -\frac{1}{2}\left[(DFS)_x-(NMR)_x+(CNV)_x\right]^{n+\frac{1}{2}}_{i-\frac{1}{2},j} + \frac{w_1}{2}\frac{\phi^{n+\frac{1}{2}}_{i-1,j}}{\Delta t_{n+\frac{1}{2}}}\Delta V_{b_{ij}}$$

$$F_{ij} = -\frac{1}{2}\left[(DFS)_x-(NMR)_x\right]^{n+\frac{1}{2}}_{i+\frac{1}{2},j} + \frac{w_1}{2}\frac{\phi^{n+\frac{1}{2}}_{i+1,j}}{\Delta t_{n+\frac{1}{2}}}\Delta V_{b_{ij}}$$

$$H_{ij} = -\frac{1}{2}\left[(DFS)_y-(NMR)_y\right]^{n+\frac{1}{2}}_{i,j+\frac{1}{2}} + \frac{w_2}{2}\frac{\phi^{n+\frac{1}{2}}_{i,j+1}}{\Delta t_{n+\frac{1}{2}}}\Delta V_{b_{ij}}$$

$$E_{ij} = \frac{1}{2}\left\{\left[(DFS)_x-(NMR)_x+(CNV)_x\right]^{n+\frac{1}{2}}_{i+\frac{1}{2},j} + \left[(DFS)_x-(NMR)_x\right]^{n+\frac{1}{2}}_{i-\frac{1}{2},j}\right.$$
$$\left. + \left[(DFS)_y-(NMR)_y+(CNV)_y\right]^{n+\frac{1}{2}}_{i,j+\frac{1}{2}} + \left[(DFS)_y-(NMR)_y\right]^{n+\frac{1}{2}}_{i,j-\frac{1}{2}}\right\}$$
$$+ \left\{(1-w_1-w_2)\frac{\phi^{n+\frac{1}{2}}}{\Delta t_{n+\frac{1}{2}}} + 2\pi N_p (r_p^{n+\frac{1}{2}})^2 \alpha^{n+\frac{1}{2}}\right\}_{ij}\Delta V_{b_{ij}}$$

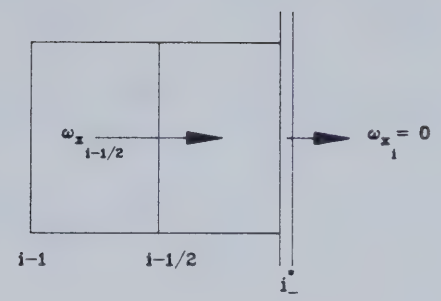
$$
\begin{aligned}
Q_{ij} = {} & \frac{1}{2}\left\{[DFS)_x - (NMR)_x]^{n+\frac{1}{2}}_{i+\frac{1}{2},j}(C^n_{i+1,j} - C^n_{i,j}) - (CNV)^{n+\frac{1}{2}}_{x_{i+\frac{1}{2},j}} C^n_{ij}\right\} + (CRS)^{n+\frac{1}{2}}_{x_{i+\frac{1}{2},j}} \\
& - \frac{1}{2}\left\{[DFS)_x - (NMR)_x]^{n+\frac{1}{2}}_{i-\frac{1}{2},j}(C^n_{i,j} - C^n_{i-1,j}) - (CNV)^{n+\frac{1}{2}}_{x_{i-\frac{1}{2},j}} C^n_{i-1,j}\right\} - (CRS)^{n+\frac{1}{2}}_{x_{i-\frac{1}{2},j}} \\
& + \frac{1}{2}\left\{[DFS)_y - (NMR)_y]^{n+\frac{1}{2}}_{i,j+\frac{1}{2}}(C^n_{i,j+1} - C^n_{i,j}) - (CNV)^{n+\frac{1}{2}}_{y_{i,j+\frac{1}{2}}} C^n_{i,j}\right\} + (CRS)^{n+\frac{1}{2}}_{y_{i,j+\frac{1}{2}}} \\
& - \frac{1}{2}\left\{[DFS)_y - (NMR)_y]^{n+\frac{1}{2}}_{i,j-\frac{1}{2}}(C^n_{i,j} - C^n_{i,j-1}) - (CNV)^{n+\frac{1}{2}}_{y_{i,j-\frac{1}{2}}} C^n_{i,j-1}\right\} - (CRS)^{n+\frac{1}{2}}_{y_{i,j-\frac{1}{2}}} \\
& + \left\{(1-w_1-w_2)\frac{\phi^{n+\frac{1}{2}}}{\Delta t_{n+\frac{1}{2}}} C^n + 4\pi N_p (r_p^{n+\frac{1}{2}})^2 \left[\alpha^{n+\frac{1}{2}}\left(\frac{C^n}{2} - C^*\right)\right]\right\}_{ij} \Delta V_{b_{ij}} \\
& + \left\{\frac{w_1}{2}\left[(\phi^{n+\frac{1}{2}}C^n)_{i+1,j} + (\phi^{n+\frac{1}{2}}C^n)_{i-1,j}\right]\right. \\
& \qquad \left. + \frac{w_2}{2}\left[(\phi^{n+\frac{1}{2}}C^n)_{i,j+1} + (\phi^{n+\frac{1}{2}}C^n)_{i,j-1}\right]\right\} \Delta V_{b_{ij}}
\end{aligned}
$$

3.6(15)

The cross dispersion terms are included in the right-hand side of the associated difference equation and their values are subsequently iterated with all other time-dependent coefficients.

As established, the perimeter is impermeable to solvent unless an inlet or outlet is specified. The normal components of both velocity and the concentration gradient must vanish at all impermeable faces of the perimeter blocks. Reflection conditions yield the superposition of a negative flow field, in which a reverse-running image concentration-wave accounts for the total reflection of solvent at the no-flow boundaries of the finite porous region [cf. Figure 3.6-1].

Figure 3.6-1 : Impermeable Boundary

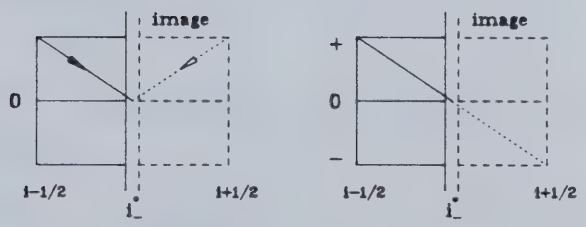


Solvent Flow

Boundary Conditions

$u_x = 0$ (at i)

$(\partial C/\partial x)_i = 0$

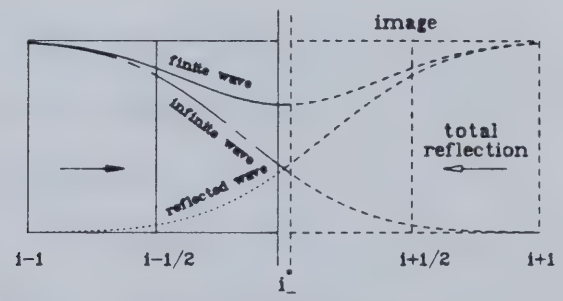


Velocity Superposition

Reflection Conditions

$u_{x\ i+1/2} = -u_{x\ i-1/2}$

$u_{x\ i} = 0$

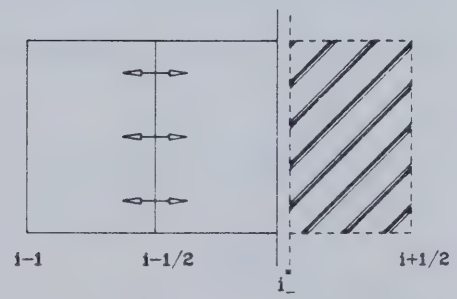


Concentration Waves

Reflection Conditions

$D_{xx\ i+1/2} = D_{xx\ i-1/2}$

$C_{i+1} = C_{i-1}$



Solvent Transmission

Transmissibility Conditions

$(DFS)_{x\ i+1/2} = 0$

$(NMR)_{x\ i+1/2} = 0$

$(CNV)_{x\ i+1/2} = 0$

$$\left.\begin{array}{l} u_{x_{i^*j}} = 0 \\ \left.\dfrac{\partial C}{\partial x}\right|_{i^*j} = 0 \end{array}\right\} \Rightarrow \left.\begin{array}{l} u_{x_{i^*+\frac{1}{2},j}} = -u_{x_{i^*-\frac{1}{2},j}} \\ C_{i^*+1,j} = C_{i^*-1,j} \end{array}\right\} P_{i^*j} \in \{\textstyle\sum_{\text{NO FLOW}}\}$$

$$\left.\begin{array}{l} u_{y_{ij^*}} = 0 \\ \left.\dfrac{\partial C}{\partial y}\right|_{ij^*} = 0 \end{array}\right\} \Rightarrow \left.\begin{array}{l} u_{y_{i,j^*+\frac{1}{2}}} = -u_{y_{i,j^*-\frac{1}{2}}} \\ C_{i,j^*+1} = C_{i,j^*-1} \end{array}\right\} P_{ij^*} \in \{\textstyle\sum_{\text{NO FLOW}}\} \qquad 3.6(16)$$

Identical algebraic expressions are obtained by constraining all transmissibilities to vanish at these no-transport boundaries.

$$(\text{DFS})^{n+\frac{1}{2}}_{x_{i^*_{\mp}\pm\frac{1}{2},j}} = (\text{NMR})^{n+\frac{1}{2}}_{x_{i^*_{\mp}\pm\frac{1}{2},j}} = (\text{CNV})^{n+\frac{1}{2}}_{x_{i^*_{\mp}\pm\frac{1}{2},j}} = 0 \; ; \quad P_{i^*j} \in \{\textstyle\sum_{\text{NO FLOW}}\}$$

$$(\text{DFS})^{n+\frac{1}{2}}_{y_{i,j^*_{\mp}\pm\frac{1}{2}}} = (\text{NMR})^{n+\frac{1}{2}}_{y_{i,j^*_{\mp}\pm\frac{1}{2}}} = (\text{CNV})^{n+\frac{1}{2}}_{y_{i,j^*_{\mp}\pm\frac{1}{2}}} = 0 \; ; \quad P_{ij^*} \in \{\textstyle\sum_{\text{NO FLOW}}\} \qquad 3.6(17)$$

Tangential fluxes exist on the interior of the impermeable faces and only the normal velocity components vanish at these points. Solvent enters and leaves the interior normal to the bounding surface, thereby the tangential fluxes vanish at all inlet and outlet perimeter mesh points. As a consequence of the velocity angles at the perimeter, the off-diagonal cartesian diffusion coefficients, and subsequently the cross dispersion terms, vanish at all perimeter faces.

$$(\text{CRS})^{n+\frac{1}{2}}_{x_{i^*_{\mp}\pm\frac{1}{2},j}} = 0 \; ; \quad P_{i^*j} \in \textstyle\sum$$

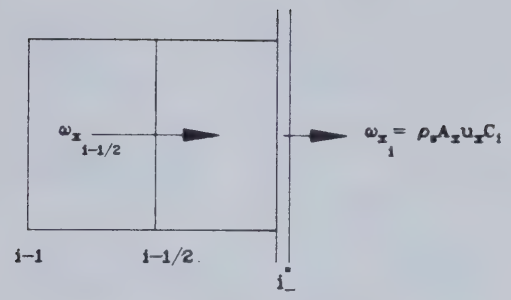
$$(\text{CRS})^{n+\frac{1}{2}}_{y_{i,j^*_{\mp}\pm\frac{1}{2}}} = 0 \; ; \quad P_{ij^*} \in \textstyle\sum \qquad 3.6(18)$$

Fluid is introduced into, and removed from the porous region at a uniform rate and hence both inlet and outlet velocity gradients vanish. Unlike the no-flow boundaries encountered at the impermeable points, the inlet/outlet points involve the partial transmission of solvent. Superposition of a negative velocity field results in a singular discontinuity, in which fluid fronts are either created (inlet source) or annihilated (outlet sink) to preserve the material balance. These source-sink terms must account for the fluid distributed over both the physical and image counterparts.

Solvent is removed at all outlet points with the fluid stream by convection only and thereby the normal component of the concentration gradients vanish. The resulting finite concentration wave is obtained by the superposition of a diffusion reflection defined in the physical domain of the porous region [cf. Figure 3.6-2]. Reflection conditions, including a distributed solvent sink density with a superimposed negative flow field, resolves the fluid singularity at the outlet point.

$$\left\{ \begin{array}{ll} \left.\dfrac{\partial u_x}{\partial x}\right|_{i^*j} = 0 & u_{x_{i^*_{\mp},j}} = u_{x_{i^*_{\mp}\pm\frac{1}{2},j}} \\ \left.\dfrac{\partial C}{\partial x}\right|_{i^*j} = 0 & C_{i^*+1,j} = C_{i^*-1,j} \\ \text{IMAGE FLOW:} & u_{x_{i^*+\frac{1}{2},j}} = -u_{x_{i^*-\frac{1}{2},j}} \\ \text{SINK DENSITY:} & -\dfrac{2}{\Delta x}\,(u_x C)_{i^*j} \end{array} \right\} \quad P_{i^*j} \in \{\textstyle\sum_{OUT}\}$$

Figure 3.6-2 : Outlet Sink Boundary

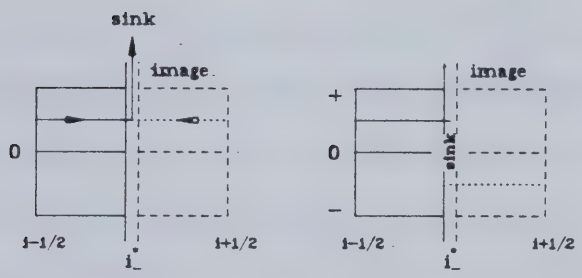


Solvent Flow

Boundary Conditions

$(\partial u_x/\partial x)_i = 0$

$(\partial C/\partial x)_i = 0$



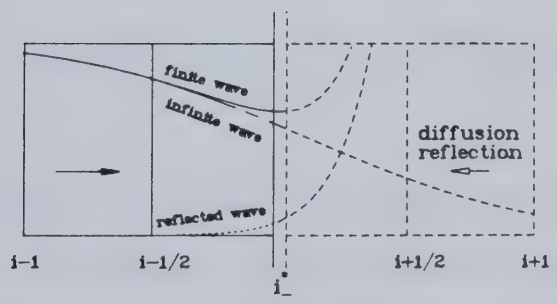
Velocity Superposition

Reflection Conditions

$u_{x\ i+1/2} = -u_{x\ i-1/2}$

$u_{x\ i} = u_{x\ i-1/2}$

distributed sink $= 2u_{x\ i}\rho_s C_i/\Delta x$

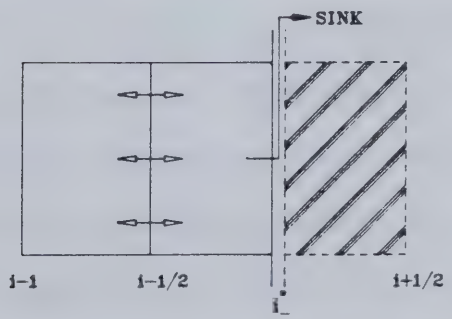


Concentration Waves

Reflection Conditions

$D_{xx\ i+1/2} = D_{xx\ i-1/2}$

$C_{i+1} = C_{i-1}$



Solvent Transmission

Transmissibility Conditions

$(DFS)_{x\ i+1/2} = 0$

$(NMR)_{x\ i+1/2} = 0$

$(CNV)_{x\ i+1/2} = 0$

SINK $= \omega_{x\ i}$

$$\left\{\begin{array}{ll} \left.\dfrac{\partial u_y}{\partial y}\right|_{ij^*} = 0 & u_{y_{i,j^*_{\mp}}} = u_{y_{i,j^*_{\mp}\pm\frac{1}{2}}} \\ & \Rightarrow \\ \left.\dfrac{\partial C}{\partial y}\right|_{ij^*} = 0 & C_{i,j^*+1} = C_{i,j^*-1} \\ \text{IMAGE FLOW:} & u_{y_{i,j^*+\frac{1}{2}}} = -u_{y_{i,j^*-\frac{1}{2}}} \\ \text{SINK DENSITY:} & -\dfrac{2}{\Delta y}(u_y C)_{ij^*} \end{array}\right\} \quad P_{ij^*} \in \{\textstyle\sum_{OUT}\} \qquad 3.6(19)$$

The corresponding outlet transmission conditions allow solvent to accumulate at the outlet face, as if impermeable to flow [3.6(17)]. The inclusion of a solvent sink equivalent to the rate of solvent outflow provides the necessary fluid removal where diffusion out of the porous region is fully damped. The sink, distributed over the outlet volume element,

$$SINK_{ij}^{n+\frac{1}{2}} = -\left(A_{x_j} u_{x_{ij}}^{n+\frac{1}{2}} + A_{y_i} u_{y_{ij}}^{n+\frac{1}{2}}\right) C_{ij}^{n+\frac{1}{2}}; \quad P_{ij} \in \{\textstyle\sum_{OUT}\} \qquad 3.6(20)$$

is included on the right-hand side of the associated difference equation. The factor "two" in the sink density of 3.6(19), arises from the half- and quarter-blocks on the perimeter.

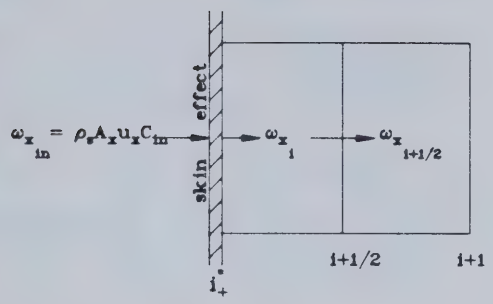
Fluid, with solvent concentration C_{IN}, is injected into the interior through all inlet points. The skin effect, includes an accumulation term distributed over the inlet surface, proportional to the solvent diffusing into the interior. The effective solvent source depends on the diffusivity of the inlet surface, which is quantified by the skin factor. Reflection conditions, with a superimposed

negative flow field and an effective solvent source density, resolves the fluid singularity at these inlet points [cf. Figure 3.6-3]. A concentration discontinuity may exist at the inlet surface, where the external concentration is fixed at C_{IN}, and a non-zero gradient just within the interior. Reflection conditions which infer the impermeability of the external surface, in conjunction with the skin accumulation term, satisfy the non-zero gradient internal boundary condition. In this manner, the external source is an isolated singularity and gradients may exist along an injection path, be it the dimensions of a well bore or on the microscopic scale of the grain size.

$$\left\{ \begin{array}{l} \left.\dfrac{\partial u_x}{\partial x}\right|_{i^*j} = 0 \quad \Rightarrow \quad u_{x_{i^*_{\mp},j}} = u_{x_{i^*_{\mp}\pm\frac{1}{2},j}} \\ \\ \left.\dfrac{\partial C}{\partial x}\right|_{i^*j} = -\left(\dfrac{u_x}{D_{xx}}\right)_{i^*j} \dfrac{[C_{IN}-C_{i^*j}]}{(1-\alpha_s)} \\ \\ \text{IMAGE FLOW:} \left\{ \begin{array}{l} u_{x_{i^*+\frac{1}{2},j}} = -u_{x_{i^*-\frac{1}{2},j}} \\ \\ C_{i^*+1,j} = C_{i^*-1,j} \end{array} \right. \\ \\ \text{SOURCE DENSITY:} \quad \dfrac{2}{\Delta x}\left[u_x C_{IN} - \alpha_s D_{xx} \dfrac{\partial C}{\partial x}\right]_{i^*j} \end{array} \right\} P_{i^*j} \in \{\Sigma_{IN}\}$$

3.6(21)

Figure 3.6-3 : Inlet Source Boundary

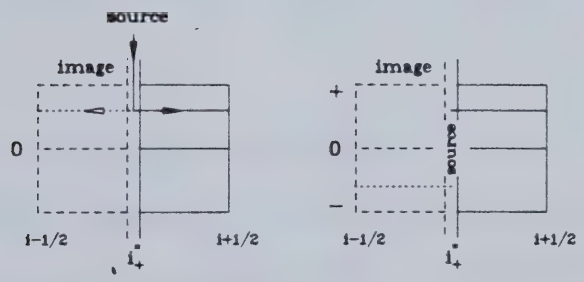


Solvent Flow

Boundary Conditions

$$\left(\partial u_x/\partial x\right)_i = 0$$

$$\left(\partial C/\partial x\right)_i = -\left(u_x/[D_{xx}(1-\alpha_s)]\right)_i \left[C_{in} - C_i\right]$$



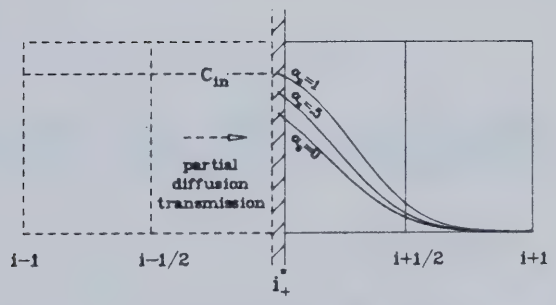
Velocity Superposition

Reflection Conditions

$$u_{x_{i+1/2}} = -u_{x_{i-1/2}}$$

$$u_{x_i} = u_{x_{i+1/2}}$$

$$\text{distributed source} = 2u_{x_i}\rho_s C_{in}/\Delta x$$



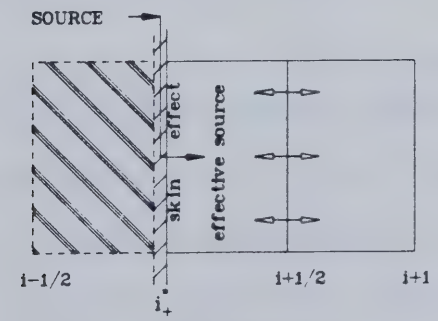
Concentration Waves

Reflection Conditions

$$D_{xx_{i+1/2}} = D_{xx_{i-1/2}}$$

$$C_{i+1} = C_{i-1}$$

$$\text{distributed skin accumulation} = 2\alpha_s\left(\rho_s D_{xx}\partial C/\partial x\right)_i/\Delta x$$



Solvent Transmission

Transmissibility Conditions

$$(DFS)_{x_{i-1/2}} = 0$$

$$(NMR)_{x_{i-1/2}} = 0$$

$$(CNV)_{x_{i-1/2}} = 0$$

$$\text{EFFECTIVE SOURCE} = \omega_{x_{in}} - \alpha_s A_x\left(\rho_s D_{xx}\partial C/\partial x\right)_i$$

$$\left\{\begin{array}{l} \left.\dfrac{\partial u_y}{\partial y}\right|_{ij^*} = 0 \Rightarrow u_{y_{i,j^*_{\mp}}} = u_{y_{i,j^*_{\mp}\pm\frac{1}{2}}} \\ \left.\dfrac{\partial C}{\partial y}\right|_{ij^*} = -\left(\dfrac{u_y}{D_{yy}}\right)_{ij^*} \dfrac{[C_{IN}-C_{ij^*}]}{(1-\alpha_s)} \\ \text{IMAGE FLOW:} \left\{\begin{array}{l} u_{y_{i,j^*+\frac{1}{2}}} = -u_{y_{i,j^*-\frac{1}{2}}} \\ C_{i,j^*+1} = C_{i,j^*-1} \end{array}\right. \\ \text{SOURCE DENSITY:} \quad \dfrac{2}{\Delta y}\left[u_y C_{IN} - \alpha_s D_{yy} \dfrac{\partial C}{\partial y}\right]_{ij^*} \end{array}\right\} P_{ij^*} \in \{\textstyle\sum_{IN}\}$$

3.6(21)

The transmission conditions for the inlet are those of the impermeable boundary [3.6(17)] with an effective solvent source allowing for the partial diffusive transmission from an external reservoir. The effective source, distributed over the inlet volume element,

$$\text{SOURCE}_{ij}^{n+\frac{1}{2}} = \left\{\left(A_{x_j} u_{x_{ij}}^{n+\frac{1}{2}} + A_{y_i} u_{y_{ij}}^{n+\frac{1}{2}}\right)\left[C_{IN}^{n+\frac{1}{2}} + \frac{\alpha_s}{(1-\alpha_s)}\left(C_{IN}^{n+\frac{1}{2}} - C_{ij}^{n+\frac{1}{2}}\right)\right]\right\};$$

$$P_{ij} \in \{\textstyle\sum_{IN}\} \qquad 3.6(22)$$

is included on the right-hand side of the associated difference equation.

The concept of "skin effect" provides mathematical flexibility, in which the Dirichlet condition is a limiting case. Diffusion of source solvent in a point configuration, representing an injection well, may be negligible for a large field yielding a virtually non-existent skin effect. In contrast, a line source representing fluid injection

into a linear core, has significant surface area open to diffusion and consequently a diffusion source must be included.

An initial surface concentration discontinuity may exist at all inlets if the internal solvent distribution differs from the external solvent concentration to be injected. The discontinuity is resolved by designating the initial surface concentration, C^{0^+}, as the arithmetic mean of the initial block concentration, C^{0^-}, and that of the concentration to be injected.

$$C_{ij}^{0^+} = \frac{1}{2}\left(C_{IN} + C_{ij}^{0^-}\right) \qquad 3.6(23)$$

The limiting Dirichlet case requires,

$$\lim_{\alpha_s \to 1} C_{ij}^{n+1} = C_{IN}^{n+1} \qquad 3.6(24)$$

and the mid-time injected concentration follows deductively.

$$\lim_{\alpha_s \to 1} C_{ij}^{n+\frac{1}{2}} = C_{IN}^{n+\frac{1}{2}} = \frac{1}{2}\left(C_{IN}^{n+1} + C_{ij}^{n}\right) \qquad 3.6(25)$$

All inlet faces must exhibit high diffusivities to successfully apply these limiting assumptions to a physical problem. The injected concentration C_{IN}^{n+1} is assumed to be constant for all times, however the mid-time injected concentration $C_{IN}^{n+\frac{1}{2}}$ remains dependent on the current surface concentration, C_{ij}^{n}. In this manner, temporal stability is maintained as the surface concentration approaches the injected concentration. Stiffness of the inlet condition is ensured for skin factors approaching unity, however smaller skin factors may generate

either asymptotic or oscillatory responses depending on the inlet Peclet number.

3.7. Direct Solver

Each state vector has an associated difference equation for each point in the mesh centered grid. Both pressure and concentration include spatial difference equations with the standard form,

$$B_{ij}X_{i,j-1} + D_{ij}X_{i-1,j} + E_{ij}X_{ij} + F_{ij}X_{i+1,j} + H_{ij}X_{i,j+1} = Q_{ij} \qquad 3.7(1)$$

The associated difference system, ADS, is the system of N difference equation with N scalar unknowns, each corresponding to the central mesh value of the dependent variable.

$$N = N_x N_y \qquad 3.7(2)$$

The natural ordering index, ij, maps a two-dimensional mesh point onto a one-dimensional array vectored sequentially along consecutive sweeps of the grid [cf. Figure 3.7-1].

$$ij = i + N_x(j-1) \qquad 3.7(3)$$

The ADS is a vector equation,

$$A_{nat}X_{nat} = Q_{nat} \qquad 3.7(4)$$

where the non zero elements along each row of the $N \times N$ coefficient matrix corresponds to the associated difference coefficients about each natural mesh point.

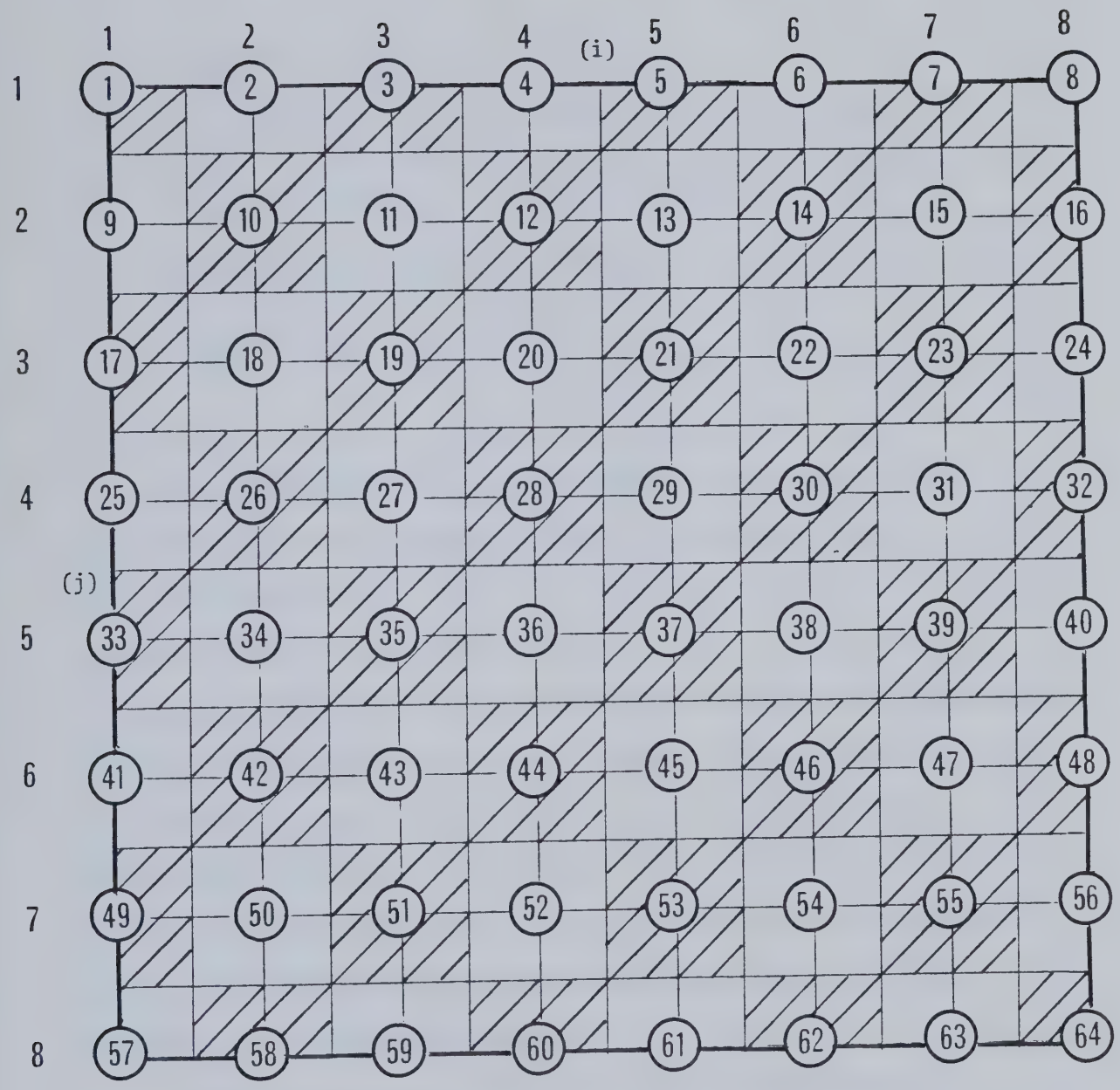


Figure 3.7-1 : Natural Ordering

$$A_{nat}(ij,ij) = E_{ij}$$

$$A_{nat}(ij,ij+1) = F_{ij} \; ; \quad \text{if} \quad \{i \neq N_x\} \sim \{\text{mod}(ij,N_x) \neq 0\}$$

$$A_{nat}(ij,ij-1) = D_{ij} \; ; \quad \text{if} \quad \{i \neq 1\} \sim \{\text{mod}(ij,N_x) \neq 1\}$$

$$A_{nat}(ij,ij+N_x) = H_{ij} \; ; \quad \text{if} \quad \{j \neq N_y\} \sim \{ij \leq (N-N_x)\}$$

$$A_{nat}(ij,ij-N_x) = B_{ij} \; ; \quad \text{if} \quad \{j \neq 1\} \sim \{ij > N_x\}$$

3.7(5)

The rectilinear constraints confine the numerical system within the spatial bounds of the physical grid. The modulus operator converts the global position to a local sweep value where the equivalent natural conditions ensure a square matrix.

Conventional Gaussian elimination techniques require the storage of all elements and the execution of numerous row operations to reduce the coefficient matrix into row echelon form, before a backward substitution can generate the solution. Better resolution requires excess mesh points forcing the augmented matrix to grow exponentially. Gaussian elimination becomes time consuming and clumsy, with many operations involving zero elements.

With the structure of the matrix map well established, an efficient solution algorithm is constructed. The scheme utilizes symbolic mappings to minimize the work necessary to generate a solution, while simultaneously reducing the storage by accomodating nonzero elements only.

By reordering the grid along alternate diagonals[43] [cf. Figure 3.7-2], the coefficient matrix partitions into well defined quadrants.

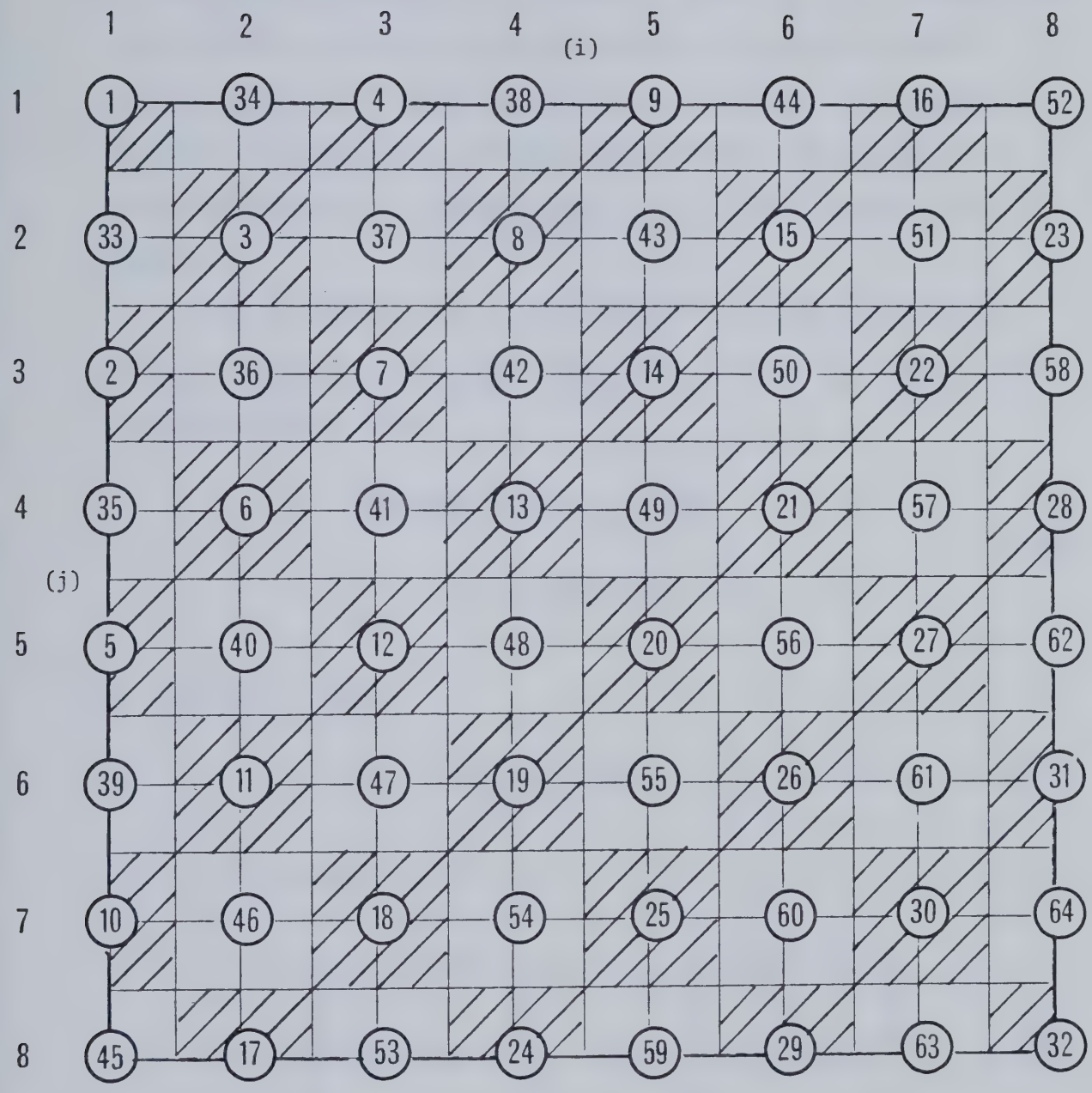


Figure 3.7-2 : Alternate Diagonal Ordering

This partitioning nature of D_4 ordering, allows an L-R decomposition to be applied with relative ease. A coupled recursive procedure requires minimal work space to unravel the upper and lower triangular matrices. By first using a forward substitution to determine an intermediate vector, a backward substitution follows to obtain the solution.

The D_4 map assigns a pointer array which maps each natural index to its corresponding D_4 index. The inverse D_4 mapping uses a separate pointer array.

$$\begin{aligned} D_4\langle ij\rangle &: \text{maps } ij_{i,j} \rightarrow D_{4_{ij}} \\ D_4^{-1}\langle D_4\langle ij\rangle\rangle &= ij \end{aligned} \qquad 3.7(6)$$

The equivalent ADS,

$$A_{D_4}\, X_{D_4} = Q_{D_4} \qquad 3.7(7)$$

with the vector quantities,

$$X_{D_4} = \begin{bmatrix} X(D_4^{-1}\langle 1\rangle) \\ \vdots \\ X(D_4^{-1}\langle ij\rangle) \\ \vdots \\ X(D_4^{-1}\langle N\rangle) \end{bmatrix} \qquad Q_{D_4} = \begin{bmatrix} Q(D_4^{-1}\langle 1\rangle) \\ \vdots \\ Q(D_4^{-1}\langle ij\rangle) \\ \vdots \\ Q(D_4^{-1}\langle N\rangle) \end{bmatrix} \qquad 3.7(8)$$

has a transformed coefficients matrix whose nonzero elements scatter into well defined quadrants.

Each row of the transformed coefficient matrix will have new associated coefficients which must abide by the equivalent D_4 conditions.

$$A_{D_4}(ij,ij) = E(D_4^{-1}\langle ij\rangle)$$

$$A_{D_4}(ij,D_4\langle D_4^{-1}\langle ij\rangle + 1\rangle) = F(D_4^{-1}\langle ij\rangle);$$
$$\text{if } \left\{\text{mod}(D_4^{-1}\langle ij\rangle, N_x) \neq 0\right\}$$

$$A_{D_4}(ij,D_4\langle D_4^{-1}\langle ij\rangle - 1\rangle) = D(D_4^{-1}\langle ij\rangle);$$
$$\text{if } \left\{\text{mod}(D_4^{-1}\langle ij\rangle, N_x) \neq 1\right\}$$

$$A_{D_4}(ij,D_4\langle D_4^{-1}\langle ij\rangle + N_x\rangle) = H(D_4^{-1}\langle ij\rangle);$$
$$\text{if } \left\{D_4^{-1}\langle ij\rangle \leq N - N_x\right\}$$

$$A_{D_4}(ij,D_4\langle D_4^{-1}\langle ij\rangle - N_x\rangle) = B(D_4^{-1}\langle ij\rangle);$$
$$\text{if } \left\{D_4^{-1}\langle ij\rangle > N_x\right\} \qquad 3.7(9)$$

A specific example for the (5×3) grid is shown in Figure 3.7-3 to illustrate the partitioning nature of the D_4 transformation. The general form of the transformed coefficient matrix has four submatrices [cf. Figure 3.7-4], with the upper left and lower right quadrants diagonal.

An L-R decomposition of A_{D_4} will yield upper and lower triangular matrices,

$$A_{D_4} = LR \qquad 3.7(10)$$

with the general forms illustrated in Figure 3.7-5. The lower triangular matrix, L, has diagonal elements of unity. The L-R decomposition can be equivalently expressed in terms of the component submatrices.

NATURAL ORDERING

NX= 5
NY= 3

J/I	1	2	3	4	5
1	1	2	3	4	5
2	6	7	8	9	10
3	11	12	13	14	15

MATRIX A:

E1	F1	0	0	0	H1	0	0	0	0	0	0	0	0	0
D2	E2	F2	0	0	0	H2	0	0	0	0	0	0	0	0
0	D3	E3	F3	0	0	0	H3	0	0	0	0	0	0	0
0	0	D4	E4	F4	0	0	0	H4	0	0	0	0	0	0
0	0	0	D5	E5	0	0	0	0	H5	0	0	0	0	0
B6	0	0	0	0	E6	F6	0	0	0	H6	0	0	0	0
0	B7	0	0	0	D7	E7	F7	0	0	0	H7	0	0	0
0	0	B8	0	0	0	D8	E8	F8	0	0	0	H8	0	0
0	0	0	B9	0	0	0	D9	E9	F9	0	0	0	H9	0
0	0	0	0	B10	0	0	0	D10	E10	0	0	0	0	H10
0	0	0	0	0	B11	0	0	0	0	E11	F11	0	0	0
0	0	0	0	0	0	B12	0	0	0	D12	E12	F12	0	0
0	0	0	0	0	0	0	B13	0	0	0	D13	E13	F13	0
0	0	0	0	0	0	0	0	B14	0	0	0	D14	E14	F14
0	0	0	0	0	0	0	0	0	B15	0	0	0	D15	E15

VECTOR X:

X1	X2	X3	X4	X5	X6	X7	X8	X9	X10	X11	X12	X13	X14	X15

VECTOR O:

O1	O2	O3	O4	O5	O6	O7	O8	O9	O10	O11	O12	O13	O14	O15

D4 ORDERING

NX= 5
NY= 3

J/I	1	2	3	4	5
1	1	10	4	13	7
2	9	3	12	6	15
3	2	11	5	14	8

MATRIX A:

E1	0	0	0	0	0	0	0	H1	F1	0	0	0	0	0
0	E11	0	0	0	0	0	0	B11	0	F11	0	0	0	0
0	0	E7	0	0	0	0	0	D7	B7	H7	F7	0	0	0
0	0	0	E3	0	0	0	0	0	D3	0	H3	F3	0	0
0	0	0	0	E13	0	0	0	0	0	D13	B13	0	F13	0
0	0	0	0	0	E9	0	0	0	0	0	D9	B9	H9	F9
0	0	0	0	0	0	E5	0	0	0	0	0	D5	0	H5
0	0	0	0	0	0	0	E15	0	0	0	0	0	D15	B15
B6	H6	F6	0	0	0	0	0	E6	0	0	0	0	0	0
D2	0	H2	F2	0	0	0	0	0	E2	0	0	0	0	0
0	D12	B12	0	F12	0	0	0	0	0	E12	0	0	0	0
0	0	D8	B8	H8	F8	0	0	0	0	0	E8	0	0	0
0	0	0	D4	0	H4	F4	0	0	0	0	0	E4	0	0
0	0	0	0	D14	B14	0	F14	0	0	0	0	0	E14	0
0	0	0	0	0	D10	B10	H10	0	0	0	0	0	0	E10

VECTOR X:

X1	X11	X7	X3	X13	X9	X5	X15	X6	X2	X12	X8	X4	X14	X10

VECTOR O:

O1	O11	O7	O3	O13	O9	O5	O15	O6	O2	O12	O8	O4	O14	O10

Figure 3.7-3 : D_4 Transformation

$$\begin{bmatrix} A_{11} & A_{12} \\ (N_1 , N_1) & (N_1 , N_2) \\ \hline A_{21} & A_{22} \\ (N_2 , N_1) & (N_2 , N_2) \end{bmatrix}$$

$$\left.\begin{aligned} N_1 &= \frac{N+1}{2} \\ N_2 &= \frac{N-1}{2} \end{aligned}\right\} \quad \text{if N odd}$$

$$\left.\begin{aligned} N_1 &= \frac{N}{2} \\ N_2 &= \frac{N}{2} \end{aligned}\right\} \quad \text{if N even}$$

Figure 3.7-4 : General Form of A_{D_4}

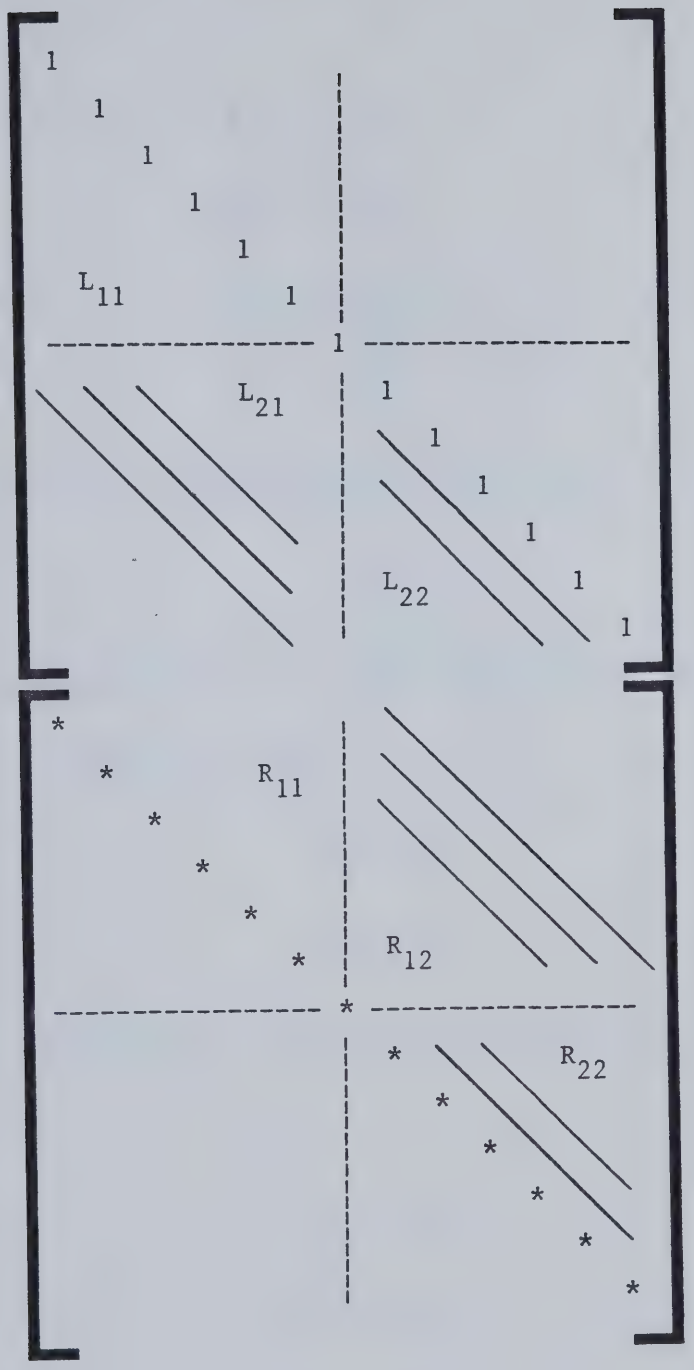


Figure 3.7-5 : General Forms of Upper and Lower Matrices

$$A_{11} = L_{11}R_{11}$$

$$A_{12} = L_{11}R_{12}$$

$$A_{21} = L_{21}R_{11}$$

$$A_{22} = L_{21}R_{12} + L_{22}R_{22} \qquad 3.7(11)$$

Since L_{11} is the identity matrix,

$$L_{11} = I \qquad 3.7(12)$$

it follows directly that the upper submatrices of R, are identical to the upper submatrices of A_{D_4}.

$$R_{11} = A_{11}$$

$$R_{12} = A_{12} \qquad 3.7(13)$$

With R_{11} identical to the diagonal submatrix, A_{11}, L_{21} follows deductively.

$$A_{21} = L_{21}A_{11}$$

$$A_{11}^{T} = A_{11} \qquad 3.7(14)$$

$$L_{21} = A_{21}A_{11}^{-1}$$

Inverse diagonal matrices pose no difficulties to evaluate and the row-wise elements of L_{21} are determined with relative ease.

for $ij = N_2 + 1, N$

$$L(ij,ij) = 1$$

$$L(ij, D_4\langle D_4^{-1}\langle ij\rangle + 1\rangle) = \frac{F(D_4^{-1}\langle ij\rangle)}{E(D_4^{-1}\langle ij\rangle + 1)} \quad ; \quad \text{if} \quad (i \neq N_x)_{D_4}$$

$$L(ij, D_4\langle D_4^{-1}\langle ij\rangle - 1\rangle) = \frac{D(D_4^{-1}\langle ij\rangle)}{E(D_4^{-1}\langle ij\rangle - 1)} \quad ; \quad \text{if} \quad (i \neq 1)_{D_4}$$

$$L(ij, D_4\langle D_4^{-1}\langle ij\rangle + N_x\rangle) = \frac{H(D_4^{-1}\langle ij\rangle)}{E(D_4^{-1}\langle ij\rangle + N_x)} \quad ; \quad \text{if} \quad (j \neq N_y)_{D_4}$$

$$L(ij, D_4\langle D_4^{-1}\langle ij\rangle - N_x\rangle) = \frac{B(D_4^{-1}\langle ij\rangle)}{E(D_4^{-1}\langle ij\rangle - N_x)} \quad ; \quad \text{if} \quad (j \neq 1)_{D_4}$$

3.7(15)

The remaining submatrices L_{22} and R_{22} are somewhat more complicated to isolate.

$$L_{22}R_{22} = A_{22} - L_{21}R_{12} \qquad 3.7(16)$$

The forms of these submatrices [cf. Figure 3.7-6] are also upper and lower triangular. Each consecutive nonzero diagonal for the respective submatrix can be mapped onto a specific workspace location.

$$L_\ell(ij) = L(ij, ij - \ell) \qquad ij = N_2 + \ell + 1,\ N$$
$$R_\ell(ij) = R(ij, ij + \ell) \qquad ij = N_2 + 1,\ N - \ell \qquad 3.7(17)$$

An algorithm is constructed for the isolation of L_{22} and R_{22}, on the basis of the grouping patterns of specific combinations of associated

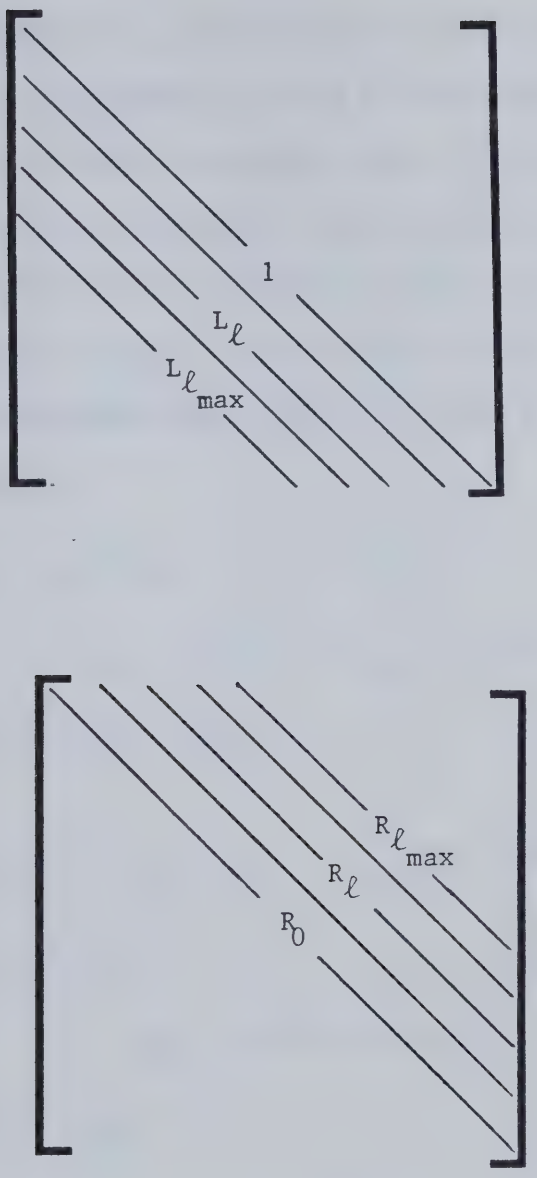


Figure 3.7-6 : General Forms of L_{22} and R_{22} Submatrices

difference coefficients, and the manner in which they scatter into the workspace. The development is based on inspectional pattern recognition, with a sequence of tests assigning groups to specific locations. An unravelling procedure recursively restructures the workspace, to be used in conjunction with both forward and backward substitutions.

The lower triangular submatrix has diagonal L_0 whose elements are unity. Intermediate quantities, L^* and R^*, are defined in terms of known submatrices.

for $ij = N_2 + 2, N$

$$M_{min} = \max\{(N_2 + 1 + \ell_{max} - ij), 0\}$$

for $\ell = 1, \ell_{max} - M_{min}$

$$L^*_\ell(ij) = A_{D_4}(ij, ij - \ell) - \sum_{k=1}^{N_2} L(ij,k)R(k, ij - \ell)$$

for $ij = N_2 + 1, N$

$$M_{max} = \min\{(N-ij), \ell_{max}\}$$

for $\ell = 0, M_{max}$

$$R^*_\ell(ij) = A_{D_4}(ij, ij + \ell) - \sum_{k=1}^{N_2} L(ij,k)R(k, ij + \ell)$$

It is noted upon inspection, that the diagonal elements along R^*_0 have contributions from four groups of associated difference coefficients.

for $ij = N_2 + 1, N$

$$R_0^*(ij) = E(D_4^{-1}<ij>)$$

$$- \left\{ F(D_4^{-1}<ij>) \frac{D(D_4^{-1}<ij>+1)}{E(D_4^{-1}<ij>+1)} \right\}, \quad \text{if} \quad (i \neq N_x)_{D_4}$$

$$- \left\{ D(D_4^{-1}<ij>) \frac{F(D_4^{-1}<ij>-1)}{E(D_4^{-1}<ij>-1)} \right\}, \quad \text{if} \quad (i \neq 1)_{D_4}$$

$$- \left\{ H(D_4^{-1}<ij>) \frac{B(D_4^{-1}<ij>+N_x)}{E(D_4^{-1}<ij>+N_x)} \right\}, \quad \text{if} \quad (j \neq N_y)_{D_4}$$

$$- \left\{ B(D_4^{-1}<ij>) \frac{H(D_4^{-1}<ij>-N_x)}{E(D_4^{-1}<ij>-N_x)} \right\}, \quad \text{if} \quad (j \neq 1)_{D_4}$$

3.7(19)

Furthermore, a maximum of four other combinations are possible for the remaining nonzero entries of R_ℓ^*. These combinations, and a similar set for L_ℓ^*, are listed in Table 3.7-1. Each combination has an associated test which generates a value of ℓ for the current index ij. If this value for ℓ is between designated limits, the corresponding combination successfully occupies the unique position (ℓ, ij). No two combinations can occupy the same position. Table 3.7-2 lists these tests.

Combination (1) appears in the outermost non zero diagonal.

$$\ell_{max} = \max \left\{ \left[D_4 < D_4^{-1} < ij > + 2 > - ij \right] ; \quad ij = N_2 + 1, N - 1 \right\}$$

3.7(20)

Each test is executed sequentially {for $ij = N_2 + 1, N - 1$} to fill the

COMBINATION	R_ℓ^*	L_ℓ^*
(1)	$FE^{-1}F$	$DE^{-1}D$
(2)	$FE^{-1}H$, $HE^{-1}F$	$DE^{-1}B$, $BE^{-1}D$
(3)	$HE^{-1}H$	$BE^{-1}B$
(4)	$FE^{-1}B$, $BE^{-1}F$	$DE^{-1}H$, $HE^{-1}D$

Table 3.7-1: Possible Entry Combinations for R_ℓ^* and L_ℓ^*

NO.	TEST	OUTCOME
①	$\ell = D_4\langle D_4^{-1}\langle ij\rangle+2\rangle - ij$ if $\{1 \leq \ell \leq \ell_{max} \wedge \ell \leq (N-ij)\}$	$R_\ell^*(ij) = -F(D_4^{-1}\langle ij\rangle)\left[\frac{F(D_4^{-1}\langle ij\rangle+1)}{E(D_4^{-1}\langle ij\rangle+1)}\right]$; if $(i \neq N_x)_{D_4}$ $L_\ell^*(ij+\ell) = -D(D_4^{-1}\langle ij+\ell\rangle)\left[\frac{D(D_4^{-1}\langle ij+\ell\rangle-1)}{E(D_4^{-1}\langle ij+\ell\rangle-1)}\right]$; if $(i \neq N_x)_{D_4}$
②	$\ell = D_4\langle D_4^{-1}\langle ij\rangle+N_x+1\rangle - ij$ if $\{1 \leq \ell \leq \ell_{max} \wedge \ell \leq (N-ij)\}$	$R_\ell^*(ij) = -F(D_4^{-1}\langle ij\rangle)\left[\frac{H(D_4^{-1}\langle ij\rangle+1)}{E(D_4^{-1}\langle ij\rangle+1)}\right]$; if $(i \neq N_x)_{D_4}$ $-H(D_4^{-1}\langle ij\rangle)\left[\frac{F(D_4^{-1}\langle ij\rangle+N_x)}{E(D_4^{-1}\langle ij\rangle+N_x)}\right]$; if $(j \neq N_y)_{D_4}$ $L_\ell^*(ij+\ell) = -D(D_4^{-1}\langle ij+\ell\rangle)\left[\frac{B(D_4^{-1}\langle ij+\ell\rangle-1)}{E(D_4^{-1}\langle ij+\ell\rangle-1)}\right]$; if $(i \neq N_x)_{D_4}$ $-B(D_4^{-1}\langle ij+\ell\rangle)\left[\frac{D(D_4^{-1}\langle ij+\ell\rangle-N_x)}{E(D_4^{-1}\langle ij+\ell\rangle-N_x)}\right]$; if $(j \neq N_y)_{D_4}$

Table 3.7-2: Entry Assignment Tests for R_ℓ^* and L_ℓ^*

NO.	TEST	OUTCOME
(3)	$\ell = D_4\langle D_4^{-1}\langle ij\rangle + 2N_x\rangle - ij$ if $\{1 \leq \ell \leq \ell_{max} \wedge \ell \leq (N-ij)\}$	$R^*_\ell(ij) = -H(D_4^{-1}\langle ij\rangle)\left[\frac{H(D_4^{-1}\langle ij\rangle + N_x)}{E(D_4^{-1}\langle ij\rangle + N_x)}\right]$; if $(j \neq N_y)_{D_4}$ $L^*_\ell(ij+\ell) = -B(D_4^{-1}\langle ij+\ell\rangle)\left[\frac{B(D_4^{-1}\langle ij+\ell\rangle - N_x)}{E(D_4^{-1}\langle ij+\ell\rangle - N_x)}\right]$; if $(j \neq N_y)_{D_4}$
(4)	$\ell = D_4\langle D_4^{-1}\langle ij\rangle - N_x + 1\rangle - ij$ if $\{1 \leq \ell \leq \ell_{max} \wedge \ell \leq (N-ij)\}$	$R^*_\ell(ij) = -F(D_4^{-1}\langle ij\rangle)\left[\frac{B(D_4^{-1}\langle ij\rangle + 1)}{E(D_4^{-1}\langle ij\rangle + 1)}\right]$; if $(i \neq N_x)_{D_4}$ $-B(D_4^{-1}\langle ij\rangle)\left[\frac{F(D_4^{-1}\langle ij\rangle - N_x)}{E(D_4^{-1}\langle ij\rangle - N_x)}\right]$; if $(j \neq 1)_{D_4}$ $L^*_\ell(ij+\ell) = -D(D_4^{-1}\langle ij+\ell\rangle)\left[\frac{H(D_4^{-1}\langle ij+\ell\rangle - 1)}{E(D_4^{-1}\langle ij+\ell\rangle - 1)}\right]$; if $(i \neq N_x)_{D_4}$ $-H(D_4^{-1}\langle ij+\ell\rangle)\left[\frac{D(D_4^{-1}\langle ij+\ell\rangle + N_x)}{E(D_4^{-1}\langle ij+\ell\rangle + N_x)}\right]$; if $(j \neq 1)_{D_4}$

Table 3.7-2: Entry Assignment Tests for R^*_ℓ and L^*_ℓ

workspace of R^*_ℓ and L^*_ℓ. With R^*_ℓ and L^*_ℓ fully evaluated, a coupled recursive procedure restructures the workspace to unravel both R_ℓ and L_ℓ.

for $\ell = 0, \ell_{max}$; $R_\ell(N_2+1) = R^*_\ell(N_2+1)$

for $ij = N_2 + 2, N$

$$M_{min} = \max\{(N_2+1+\ell_{max}-ij),0\}$$

$$M_{max} = \min\{(N-ij),\ell_{max}\}$$

for $\ell = M_{min}, \ell_{max} - 1$

$$L_{\ell_{max}-\ell}(ij) = \frac{L^*_{\ell_{max}-\ell}(ij)}{R_0(ij-\ell_{max}+\ell)} - \left\{\left[\frac{1}{R_0(ij-\ell_{max}+\ell)} \sum_{k=1}^{\ell} L_{\ell_{max}-\ell+k}(ij)R_k(ij-\ell_{max}+\ell-k)\right]\ ;\ \text{if } \ell \neq M_{min}\right\}$$

for $\ell = 0, M_{max}$

$$\ell_k = (\ell_{max} - M_{min})$$

$$R_\ell(ij) = R^*_\ell(ij) - \left\{\left[\sum_{k=1}^{\ell_k} L_k(ij)R_{\ell+k}(ij-k)\right]\ ;\ \text{if } \ell \neq \ell_{max}\right\}$$

$$\ell_k = \min\{\ell_k, (\ell_{max} - \ell)\} \qquad 3.7(21)$$

With the coefficient matrix fully decomposed into upper and lower triangular matrices, the solution of the ADS, 3.7(7), can be obtained by a sequential forward substitution to determine an intermediate vector Y,

$$LY = Q_{D_4}$$

for $ij = 1, N_2$; $\quad Y(ij) = Q(D_4^{-1}\langle ij\rangle)$

for $ij = N_2 + 1, N$

$$M_{max} = \min\{[ij - (N_2+1)], \ell_{max}\}$$

$$Y(ij) = Q(D_4^{-1}\langle ij\rangle)$$

$$- \left\{ \frac{F(D_4^{-1}\langle ij\rangle) Y(D_4 < D_4^{-1}\langle ij\rangle + 1 >)}{E(D_4^{-1}\langle ij\rangle + 1)} \right\}, \quad \text{if} \quad (i \neq N_x)_{D_4}$$

$$- \left\{ \frac{D(D_4^{-1}\langle ij\rangle) Y(D_4 < D_4^{-1}\langle ij\rangle - 1 >)}{E(D_4^{-1}\langle ij\rangle - 1)} \right\}, \quad \text{if} \quad (i \neq 1)_{D_4}$$

$$- \left\{ \frac{H(D_4^{-1}\langle ij\rangle) Y(D_4 < D_4^{-1}\langle ij\rangle + N_x >)}{E(D_4^{-1}\langle ij\rangle + N_x)} \right\}, \quad \text{if} \quad (j \neq N_y)_{D_4}$$

$$- \left\{ \frac{B(D_4^{-1}\langle ij\rangle) Y(D_4 < D_4^{-1}\langle ij\rangle - N_x >)}{E(D_4^{-1}\langle ij\rangle - N_x)} \right\}, \quad \text{if} \quad (j \neq 1)_{D_4}$$

$$- \left\{ \sum_{\ell=1}^{M_{max}} L_\ell(ij) Y(ij - \ell) \right\}, \quad \text{if} \quad (ij \neq N_2 + 1)$$

3.7(22)

followed by a sequential backward substitution for the dependent variable.

$$RX_{D_4} = Y$$

for $ij = N, N_2 + 1$

$$M_{max} = \min\{(N-ij), \ell_{max}\}$$

$$X(D_4^{-1}<ij>) = \frac{Y(ij)}{R_0(ij)}$$

$$- \frac{1}{R_0(ij)} \left\{ \sum_{\ell=1}^{M_{max}} R_\ell(ij) X(D_4^{-1}<ij+\ell>) \right\}, \text{ if } (ij \neq N)$$

for $ij = N_2, 1$

$$X(D_4^{-1}<ij>) = \frac{Y(ij)}{E(D_4^{-1}<ij>)}$$

$$- \left\{ \frac{F(D_4^{-1}<ij>)}{E(D_4^{-1}<ij>)} X(D_4^{-1}<ij>+1) \right\}, \quad \text{if} \quad (i \neq N_x)_{D_4}$$

$$- \left\{ \frac{D(D_4^{-1}<ij>)}{E(D_4^{-1}<ij>)} X(D_4^{-1}<ij>-1) \right\}, \quad \text{if} \quad (i \neq 1)_{D_4}$$

$$- \left\{ \frac{H(D_4^{-1}<ij>)}{E(D_4^{-1}<ij>)} X(D_4^{-1}<ij>+N_x) \right\}, \quad \text{if} \quad (j \neq N_y)_{D_4}$$

$$- \left\{ \frac{B(D_4^{-1}<ij>)}{E(D_4^{-1}<ij>)} X(D_4^{-1}<ij>-N_x) \right\}, \quad \text{if} \quad (j \neq 1)_{D_4}$$

The outlined solution scheme was originally developed for the general three-dimensional system of coupled difference systems for multi-variable state vectors. The general approach involves associated block matrices for the coupling coefficients and parallels the development

for this scalar two-dimensional case.

3.8. Successive Substitution

A leap-frog type solution procedure, similar to that suggested by Peaceman and Rachford,[12] is used to update the state variables for each successive time node.

The initial iterates of concentration and particle radius for the next successive (new) time node is set to their current (old) values. The next iterate for the new particle radius is determined pointwise to establish the new fluid saturation. The current iterate for the mid-time pressure field is obtained from the direct solution of the pressure associated difference system based on the current iterates for both concentration and particle radius. The mid-time velocities and diffusion coefficients are subsequently used in the concentration associated difference system to generate the next iterate for the new concentration. A convergence test completes the current iteration cycle with a comparison between new and old concentration iterates. The next iteration cycle restarts with updated iterates. The last iteration cycle of successive substitution is marked by the convergence of the concentration profile within the limits of a specified tolerance.

The nested iteration loop with iteration index m is flow charted in Figure 3.8-1 to illustrate the successive leap-frog substitution. For line sources, a discrete Newton-Raphson iterates the mid-time inlet pressure required to sustain the desired injection rate. The Newton-Raphson iteration loop (k) is flow charted in Figure 3.8-2 using the injection rates calculated from iteration loop (m).

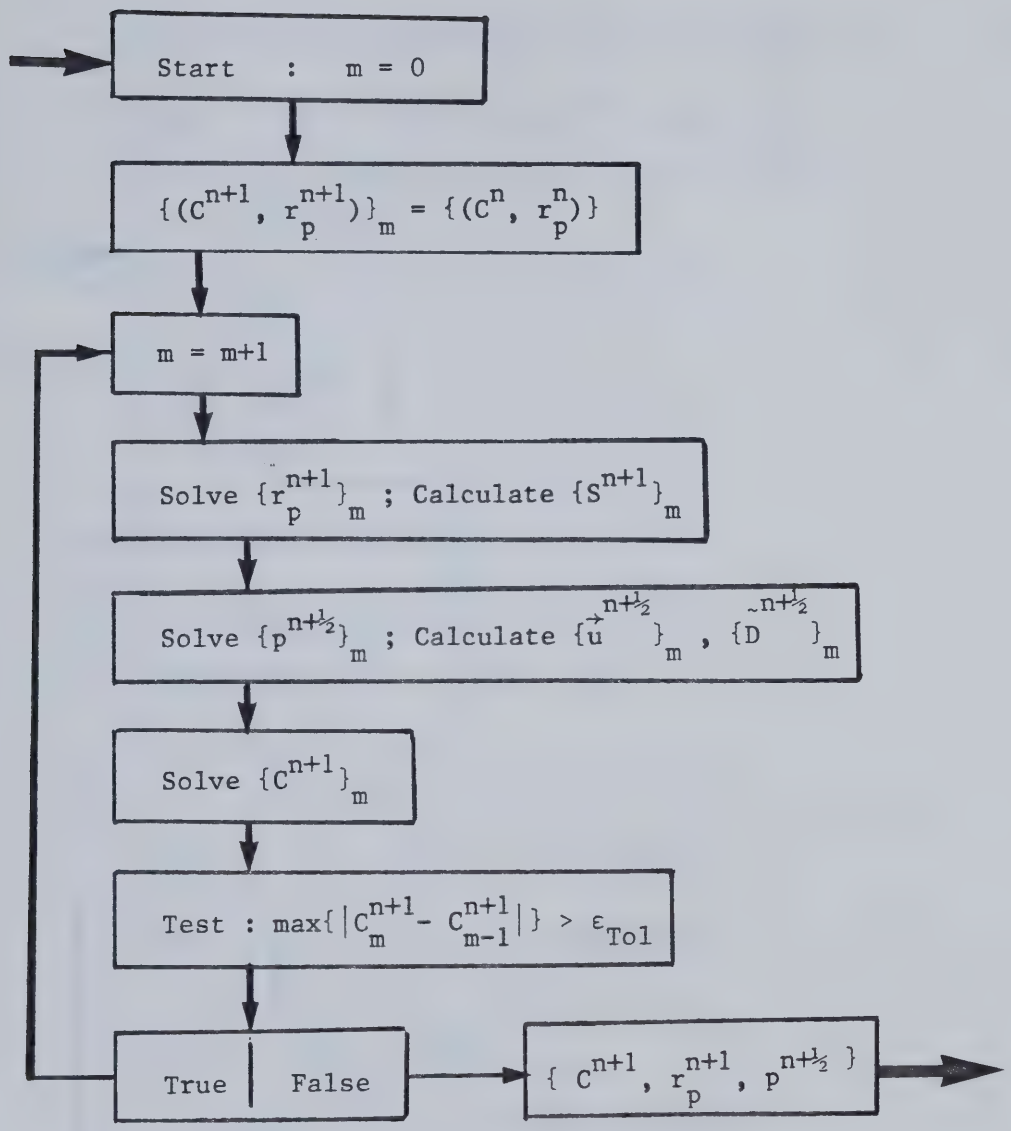


Figure 3.8-1 : Leap-Frog Iteration Loop (m)

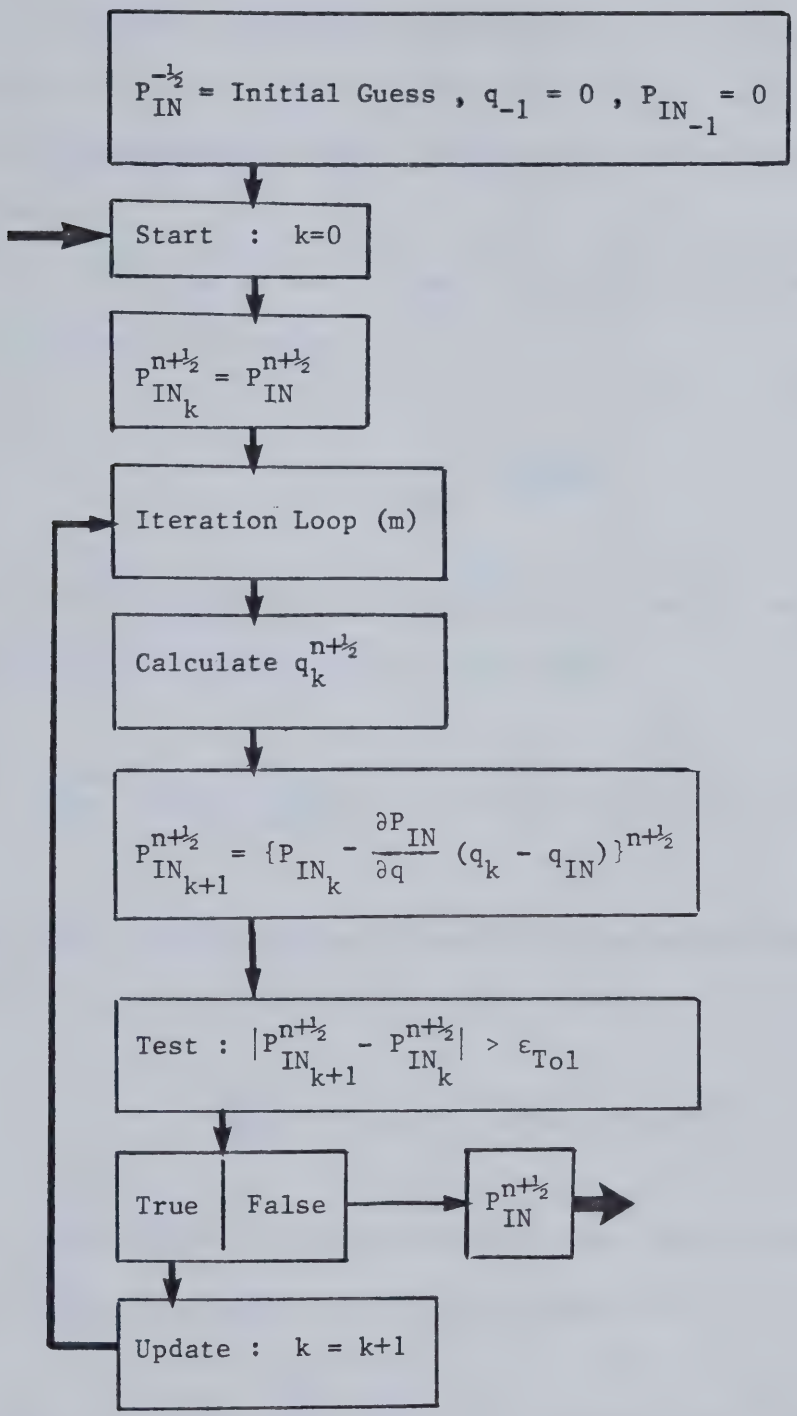


Figure 3.8-2 : Newton-Raphson Iteration Loop (k)

At each time node, both differential and cumulative solvent balance indicators monitor gross computational errors. The indicators are obtained directly from global mass balances executed over discrete time steps.

The total solvent volume, S, in the fluid stream at any time is the sum over all blocks.

$$S = \sum_{ij=1}^{N} \{\phi_m SC\Delta V_b\}_{ij} \qquad 3.8(1)$$

The total solvent volume injected into the porous region, S_{IN}, over a time step is the sum over all inlet blocks.

$$S_{IN}^{n+\frac{1}{2}} = \Delta t_{n+\frac{1}{2}} \sum_{IN} \left\{(A_x u_x + A_y u_y)\left[C_{IN} + \frac{\alpha_s}{(1-\alpha_s)}(C_{IN} - C)\right]\right\}^{n+\frac{1}{2}} \qquad 3.8(2)$$

The total solvent volume produced from the porous region, S_{OUT}, over a time step is the sum over all outlet blocks.

$$S_{OUT}^{n+\frac{1}{2}} = \Delta t_{n+\frac{1}{2}} \sum_{OUT} \{(A_x u_x + A_y u_y)C\}_{ij}^{n+\frac{1}{2}} \qquad 3.8(3)$$

The total solvent volume transferred into the solid phase, S_{SOL}, over each time step is the sum over all blocks.

$$S_{SOL}^{n+\frac{1}{2}} = 4\pi \sum_{ij=1}^{N} \left\{N_p (r_p^{n+\frac{1}{2}})^2 \left[C^*(r_p^{n+1} - r_p^n) + \Delta t_{n+\frac{1}{2}} \alpha_s (C^{n+\frac{1}{2}} - C^*)\right]\right\}_{ij} \qquad 3.8(4)$$

A differential mass balance over each time step equates solvent accumulation in the fluid phase to injection, production and solvent

transfer into the solid phase.

$$(S^{n+1} - S^{n}) = (S_{IN} - S_{OUT} - S_{SOL})^{n+\frac{1}{2}} \qquad 3.8(5)$$

Similarily, a cumulative mass balance monitors solvent flow over the total time elapsed.

$$(S^{n+1} - S^{0}) = \sum_{n_c=0}^{n} (S_{IN} - S_{OUT} - S_{SOL})^{n_c+\frac{1}{2}} \qquad 3.8(6)$$

Both differential and cumulative balances are rearranged and expressed in terms of mass balance indicators.

$$MB_d = \left\{ \frac{(S^{n+1}-S^{n}) + S_{OUT}^{n+\frac{1}{2}} + S_{SOL}^{n+\frac{1}{2}}}{S_{IN}^{n+\frac{1}{2}}} \right\}$$

$$MB_c = \left\{ \frac{(S^{n+1}-S^{0}) + \sum_{n_c=0}^{n} (S_{OUT}+S_{SOL})^{n_c+\frac{1}{2}}}{\sum_{n_c=0}^{n} S_{IN}^{n_c+\frac{1}{2}}} \right\} \qquad 3.8(7)$$

For perfect mass balances, both the differential indicator, MB_d, and the cumulative indicator, MB_c, must equate to unity. These indicators monitor gross computational errors only, such that unit indicators do not necessarily ensure the correctness of predicted state vectors.

The time-advance loop (n) is flow charted in Figure 3.8-3 to illustrate the overall solution procedure for updating the state variables.

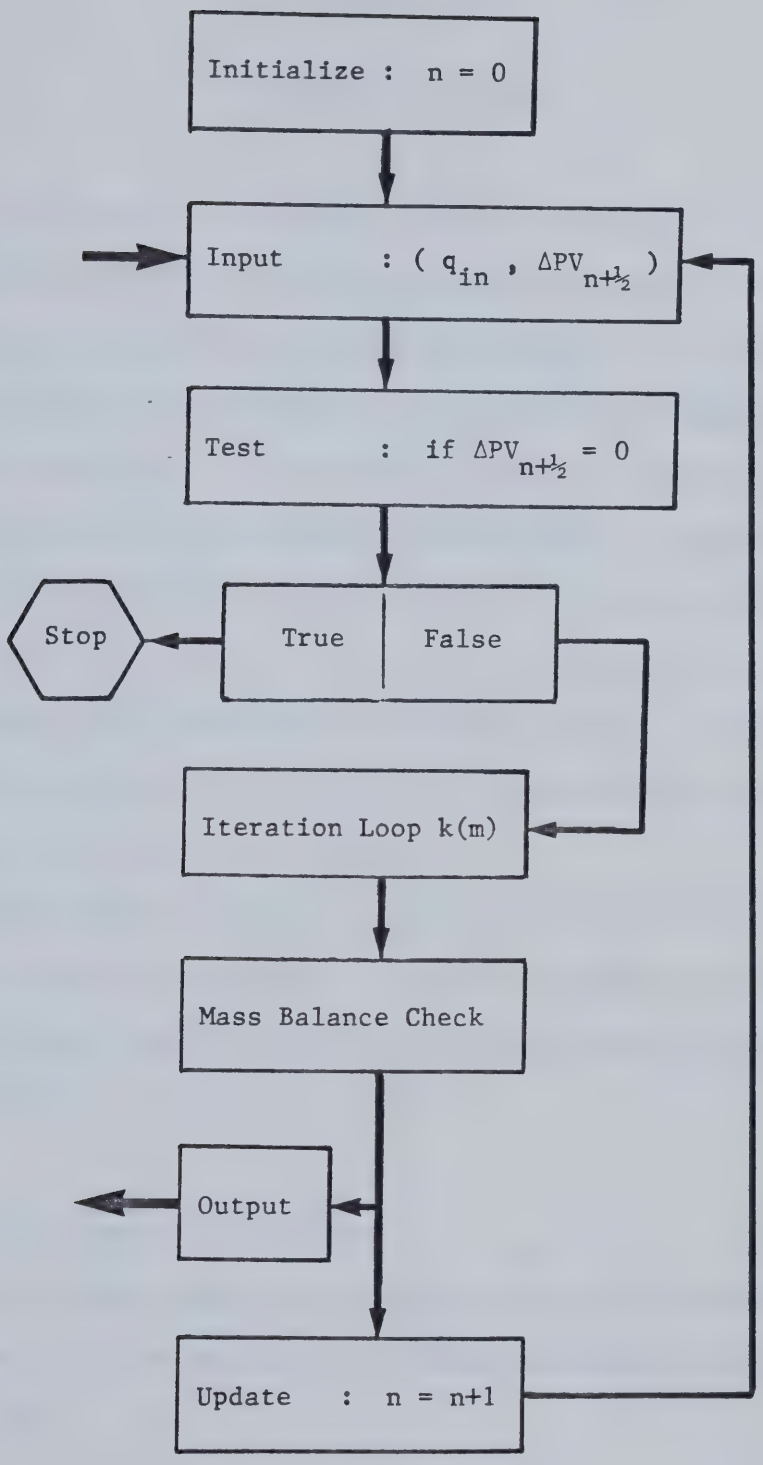


Figure 3.8-3 : Time Advance Loop (n)



CHAPTER FOUR

MISCIBLE DISPLACEMENT

The absence of interphase solvent transfer and consequently a constant fluid saturation determines the special case of the miscible displacement of an initial bitumen distribution. Under these conditions, the solid phase becomes inert and the permeability time independent.

The analytical solution for the linear problem provides the means for testing the accuracy of numerical methods. The degree of convergence of the finite difference solution to the exact solution is governed by the characteristic ratio of convection to diffusion rates and the ratio of a dimensionless time step to the normalized cell length. Stable two-dimensional concentration surfaces are predicted using the guidelines established from the linear problem.

Unfavourable displacements generate grid orientation and adverse mobility related instabilities. Realistic concentration fronts can be predicted using compatible mobility approximations for specific grid orientations.

4.1. Linear Convective Diffusion

The relevant equations describing miscible phenomena are the convective-diffusion and Darcy-continuity equations for the state vector (p,C).

$$\frac{\partial}{\partial x_i}\left\{D_{ij}\frac{\partial C}{\partial x_j} - u_i C\right\} = \phi_m \frac{\partial C}{\partial t}$$

$$\frac{\partial}{\partial x_i}\left\{\frac{\rho k_i}{\mu}\frac{\partial}{\partial x_i}(p + \rho g h)\right\} = \phi_m \frac{\partial \rho}{\partial t} \qquad 4.1(1)$$

For a linear homogeneous horizontal system with unit viscosity and density ratios, the fluid velocity becomes constant. The miscible displacement of an initially uniform bitumen distribution in this linear system is described by the one-dimensional constant-coefficient convective-diffusion equation with a Dirichlet condition at the inlet (unit skin factor), and a Neumann condition for the outlet.

$$D_{xx}\frac{\partial^2 C}{\partial x^2} - u_x \frac{\partial C}{\partial x} = \phi_m \frac{\partial C}{\partial t}$$

$$\left.\begin{aligned} C(x > 0,\ t = 0) &= 0 \\ C(x = 0,\ t > 0) &= 1 \\ \left.\frac{\partial C}{\partial x}\right|_{x=L} &= 0,\ t > 0 \end{aligned}\right\} \qquad 4.1(2)$$

By defining the dimensionless variables,

$$\xi = \frac{x}{L}$$

$$\tau = \frac{u_x t}{\phi_m L} \qquad 4.1(3)$$

$$N_{Pe} = \frac{u_x L}{D_{xx}}$$

the transformed convective-diffusion equation has the dimensionless form,

$$\frac{1}{N_{Pe}} \frac{\partial^2 C}{\partial \xi^2} - \frac{\partial C}{\partial \xi} = \frac{\partial C}{\partial \tau}$$

$$\left.\begin{aligned} C(\xi > 0,\ \tau = 0) &= 0 \\ C(\xi = 0,\ \tau > 0) &= 1 \\ \left.\frac{\partial C}{\partial \xi}\right|_{\xi=1} &= 0,\ \tau > 0 \end{aligned}\right\} \qquad 4.1(4)$$

where the Peclet number, N_{Pe}, is the characteristic ratio of convection to diffusion rates and the dimensionless time, τ, corresponds to the fractional pore volume of injected fluid.

The exact solution to this one-dimensional problem is obtained using the method of Laplace transform in Appendix C. The analytical solution has the form of an infinite series of error functions where the successive terms arise from superimposed diffusion reflections at the outlet. The series converges rapidly for the Peclet numbers and times of interest, and can be accurately approximated by the first three terms.

$$\begin{aligned} C(\xi,\tau) = \frac{1}{2}\Bigg\{ & \operatorname{erfc}\left[\frac{1}{2}\sqrt{\frac{N_{Pe}}{\tau}}\,(\xi-\tau)\right] + e^{N_{Pe}\xi} \operatorname{erfc}\left[\frac{1}{2}\sqrt{\frac{N_{Pe}}{\tau}}\,(\xi+\tau)\right]\Bigg\} \\ & + \Bigg\{\left[\frac{N_{Pe}}{2}\,(2-\xi+\tau)+1\right] e^{N_{Pe}} \operatorname{erfc}\left[\frac{1}{2}\sqrt{\frac{N_{Pe}}{\tau}}\,(2-\xi+\tau)\right] \\ & - \sqrt{\frac{N_{Pe}\,\tau}{\pi}} \exp\left(\frac{-N_{Pe}}{4}\left[\frac{(2-\xi)^2}{\tau} - 2\xi + \tau\right]\right)\Bigg\} \\ & - \Bigg\{\left[\frac{N_{Pe}}{2}\,(2+\xi+\tau)+1\right] e^{N_{Pe}} \operatorname{erfc}\left[\frac{1}{2}\sqrt{\frac{N_{Pe}}{\tau}}\,(2+\xi+\tau)\right] \\ & - \sqrt{\frac{N_{Pe}\,\tau}{\pi}} \exp\left(\frac{-N_{Pe}}{4}\left[\frac{(2+\xi)^2}{\tau} - 2\xi + \tau\right]\right)\Bigg\} \end{aligned} \qquad 4.1(5)$$

Figure 4.1-1 illustrates the lower limit at which the truncated series solution is valid. It is shown that for a unit Peclet number, convergence is sluggish and more terms may be necessary at larger dimensionless times.

The successive terms are a consequence of the region being finite. The first term is recognized as the solution to the semi-infinite analog, with the outlet at infinity. Figure 4.1-2 shows the convergence characteristics at higher Peclet numbers. The deviation of the finite solution from the semi-infinite case is shown. At high Peclet numbers, the deviation is small and for intermediate times, the concentration profiles may be represented by the first term only.

The effect of Peclet number is graphed for the family of concentration profiles at the half-pore volume injection time in Figure 4.1-3. The curves illustrate the formation of a sharp front at higher Peclet numbers.

4.2. Numerical Response and Tracking

The second-order correct central-difference scheme (CDS) and the truncation cancellation procedure (TCP) have been proposed as solution techniques. Both schemes stem from term by term central difference discretization. Other schemes, including the operator compact implicit[17] method (OCI) and the single-cell high order scheme[18] (SCHOS), use constraints based on the highest-order accuracy possible on the smallest difference-star, to determine suitable weighting coefficients. OCI derives a spatial operator for the combined convective and diffusive terms using Taylor series. SCHOS, based on the

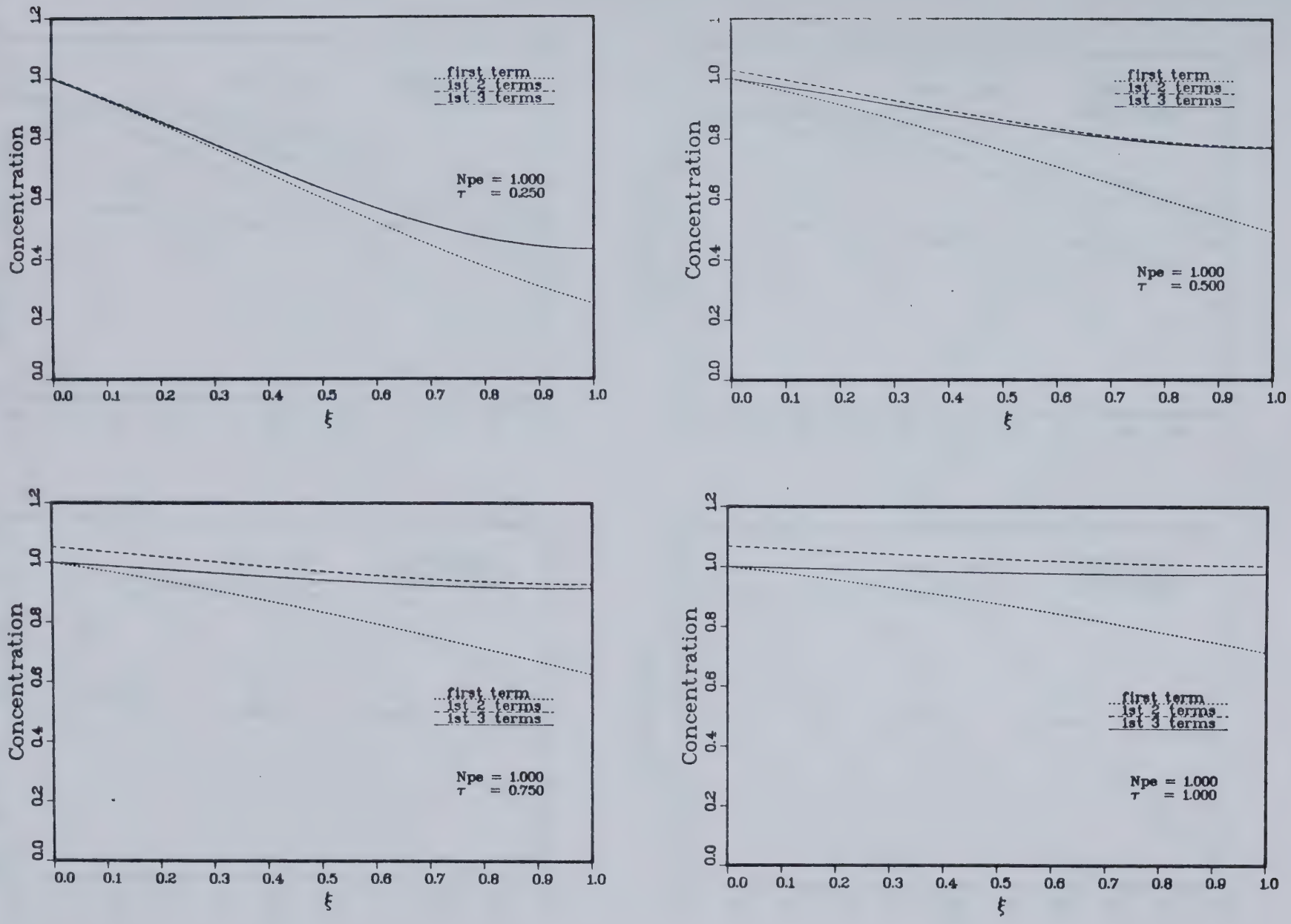


Figure 4.1-1 : Series Solution - Lower Convergence Limit

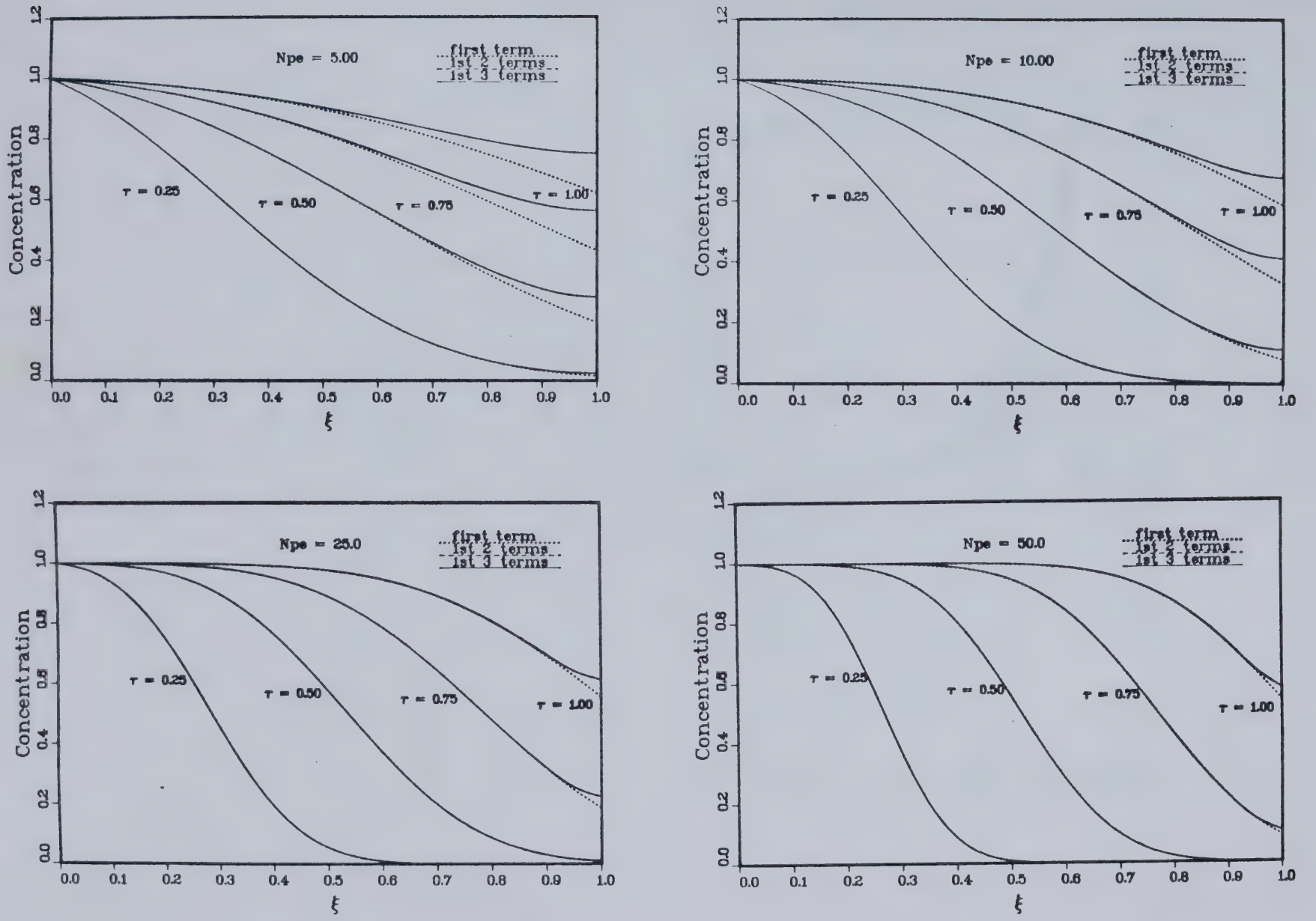


Figure 4.1-2 : Series Solution - Convergence Characteristics

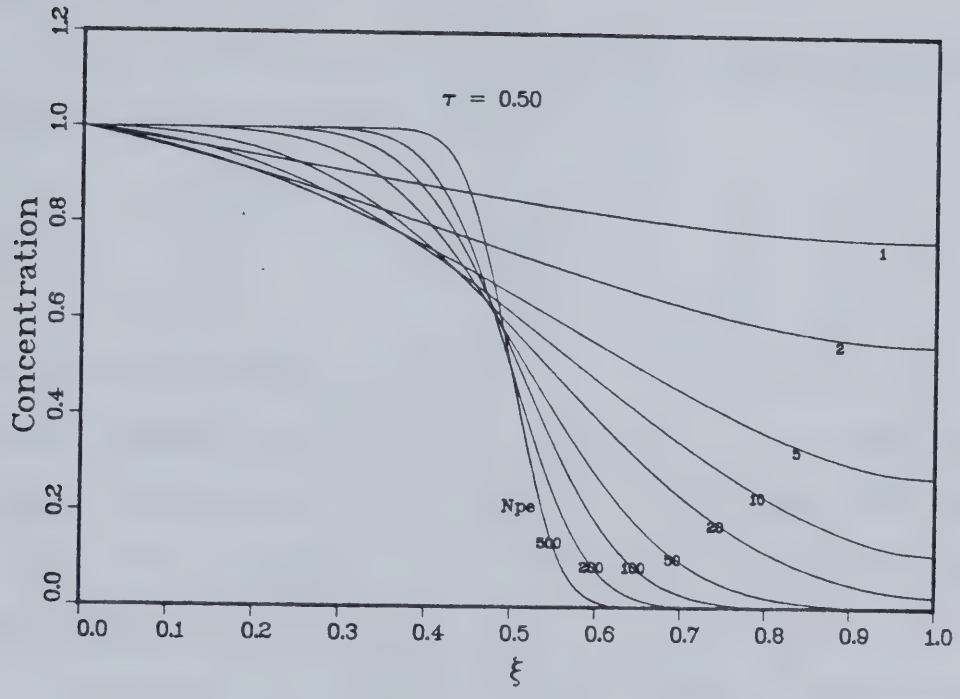


Figure 4.1-3 : Peclet Effects - The Linear Problem

local power-series solution, is intrinsically multi-dimensional and a one-dimensional analog is not available. OCI is outlined in Appendix D for the linear problem, such that comparison with an alternative approach is possible.

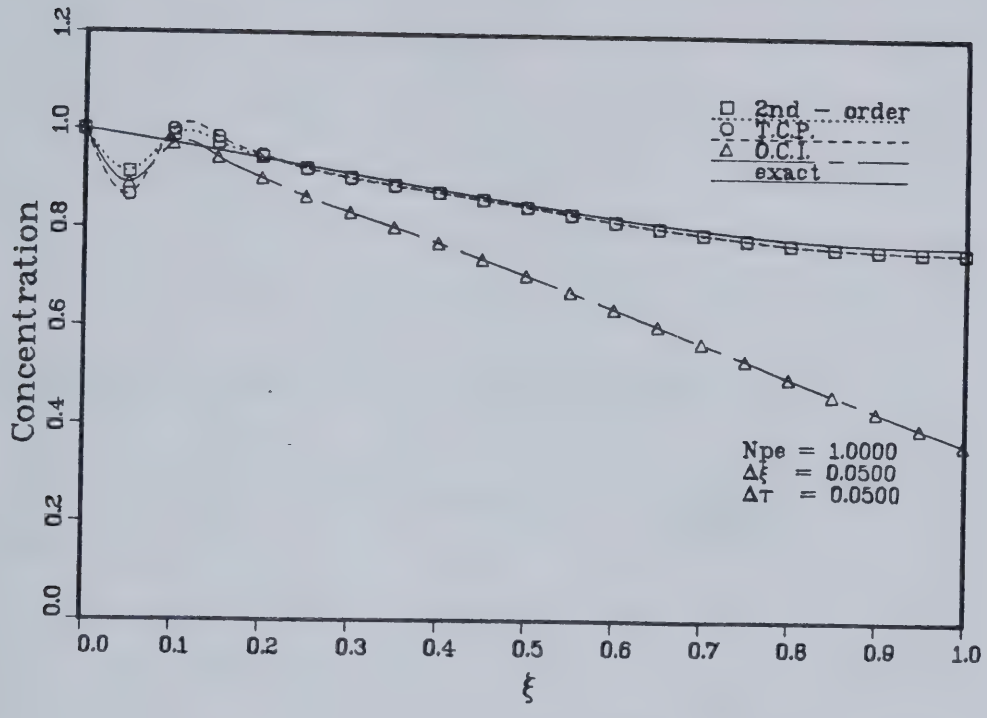
In a two-dimensional nonlinear problem, variable velocities give rise to a range of cell-Peclet numbers, N_{Ce}.

$$N_{Ce} = \frac{u_x \Delta x}{D_{xx}} \qquad 4.2(1)$$

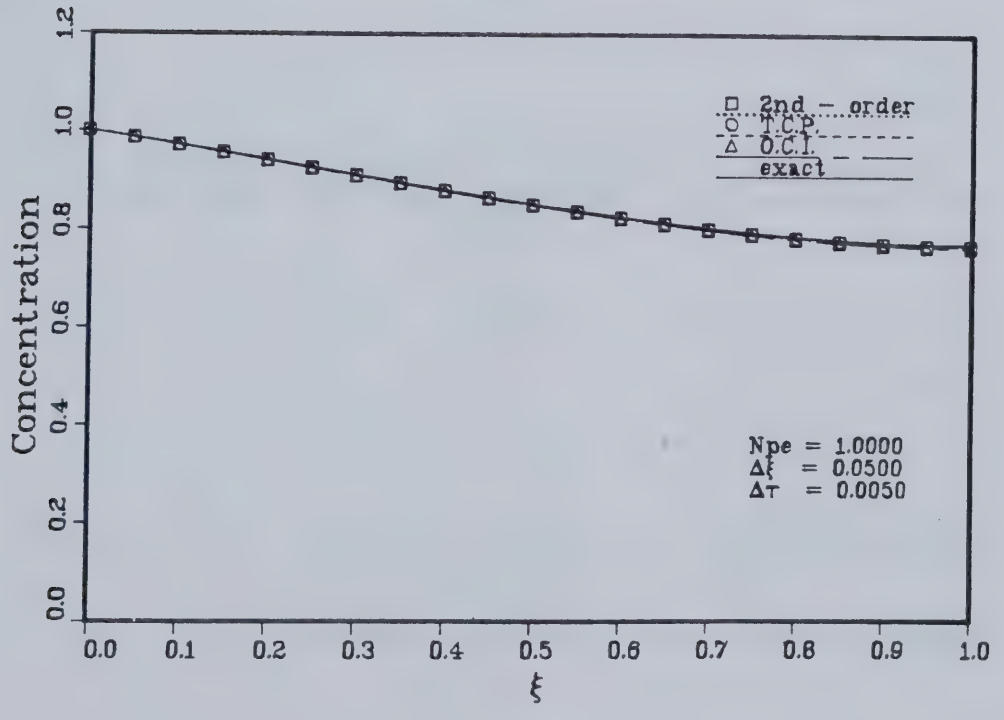
The behaviour of numerical methods for the linear problem will yield valuable insight into the expected performance for two-dimensional problems. The numerical solution to the linear problem using CDS, TCP and OCI are compared to the exact series solution for a range of Peclet numbers. Time steps are varied.

Figure 4.2-1 illustrates the damping effect of smaller time steps on an inherent source oscillation at low cell-Peclet numbers, $N_{Ce} = 0(.1)$. The oscillation originates from the initial concentration step function and is localized about the source at low convection rates. Both CDS and TCP track the exact solution adequately, however gross deviations are apparent for OCI at larger time steps. It is anticipated this deviation will cause OCI methods to predict lower concentrations at the stagnant pockets encountered in a two-dimensional displacement. At these low Peclet numbers, the CDS method provides the best overall accuracy.

These oscillations disappear at moderate cell-Peclet numbers, $N_{Ce} = 0(1.0)$, and dimensionless time steps not exceeding the normalized

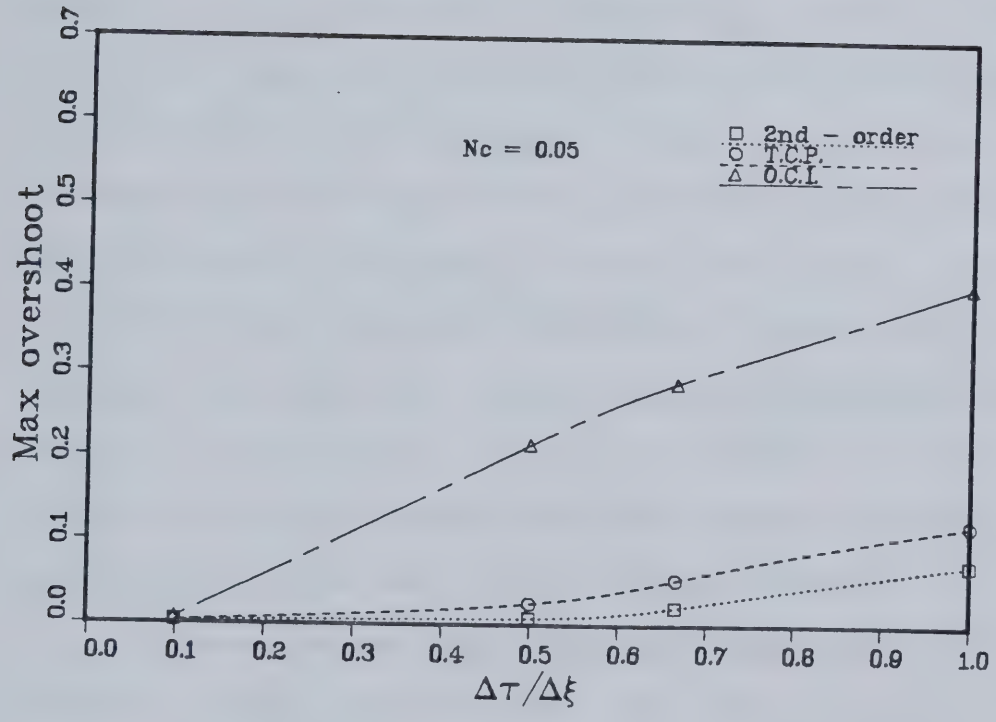


(a)



(b)

Figure 4.2-1 (a),(b)



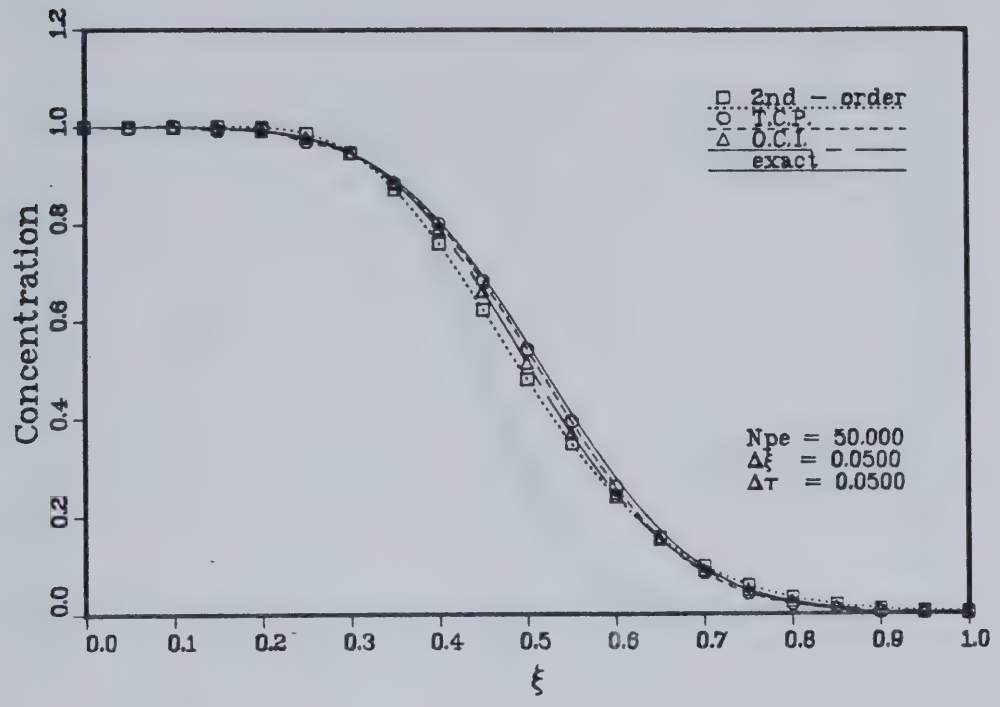
(c)

Figure 4.2-1 : Numerical Solutions - Low Cell-Peclet Numbers
(a),(b) Concentration Profiles
(c) Maximum Deviation from the Exact Solution

cell length. All schemes track the exact solution accurately with TCP and OCI errors approaching zero [cf. Figure 4.2-2]. It is expected that all three methods will exhibit a well-behaved, accurate representation of the two-dimensional concentration surface for displacements simulated at moderate cell-Peclet numbers.

Gross errors are encountered with the OCI method at cell numbers above the invertibility criterion, $N_{Ce} = 3.464$ [cf. Appendix D]. Figure 4.2-3 shows the result of overstepping this criterion with the onset of gross spatial instability. Figure 4.2-4 illustrates the existence of an upper bound to the instability interval with the revival in OCI marked by the damping of temporal oscillations. A stability analysis by Ciment, Leventahl and Weinberg[30] predicts such an instability interval, above which OCI has an oscillatory convergence to the exact solution. Caution must be exercised in applying OCI methods to two-dimensional nonlinear problems, where the critical cell-Peclet interval need not be identical with that of the linear problem.

A convective-dominant oscillation is characteristic of difference solutions at higher Peclet numbers. The oscillation originates from the source and grows with a propagating front. In Figure 4.2-5, the response of the solution methods to high Peclet numbers is illustrated. A bounded oscillation persists with the second-order CDS for all possible time steps, consequently lower concentrations are predicted at the front. Reduction in time step provides temporal damping for OCI schemes, giving an adequate representation of the front with only a slight ripple. The TCP method was originally derived for convective-dominant problems, and in this one-dimensional case gives high accuracy



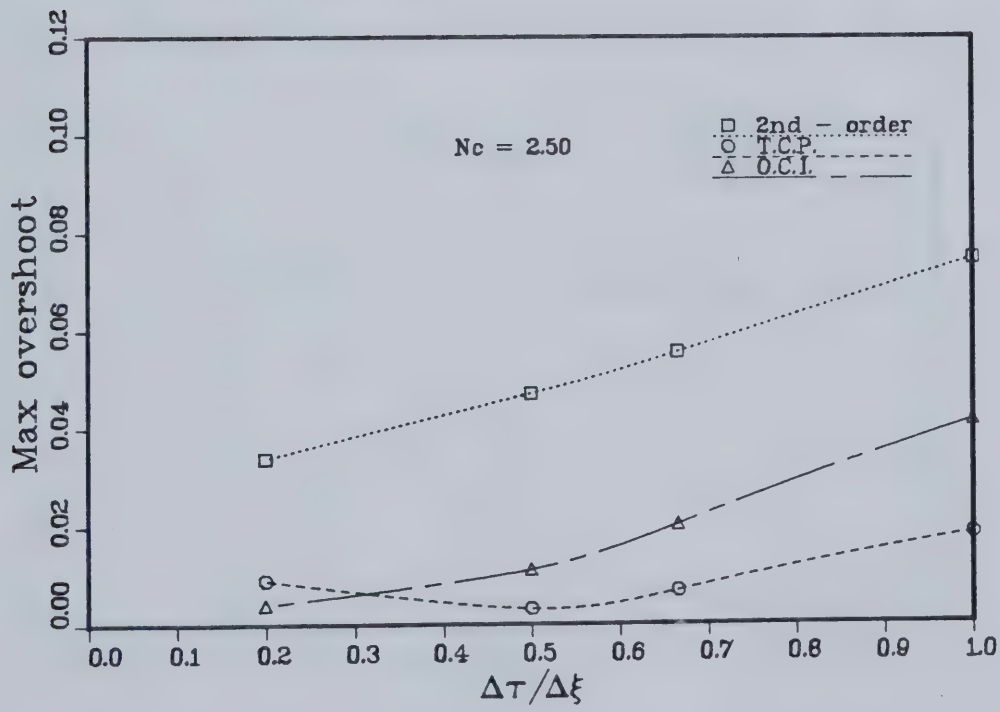
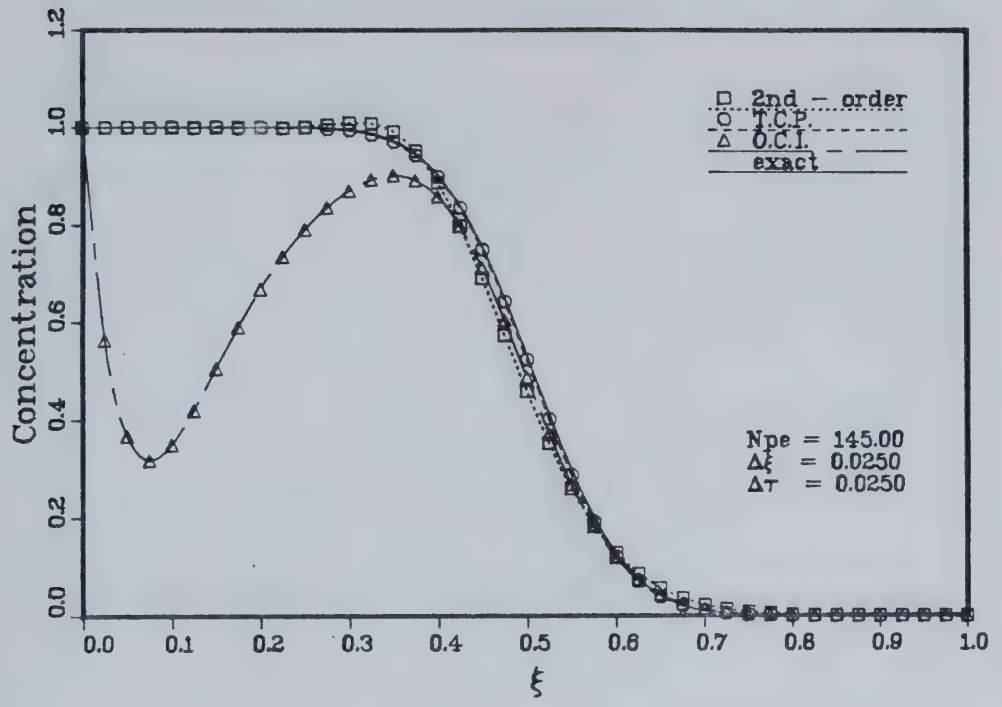


Figure 4.2-2 : Numerical Solutions - Moderate Cell-Peclet Numbers





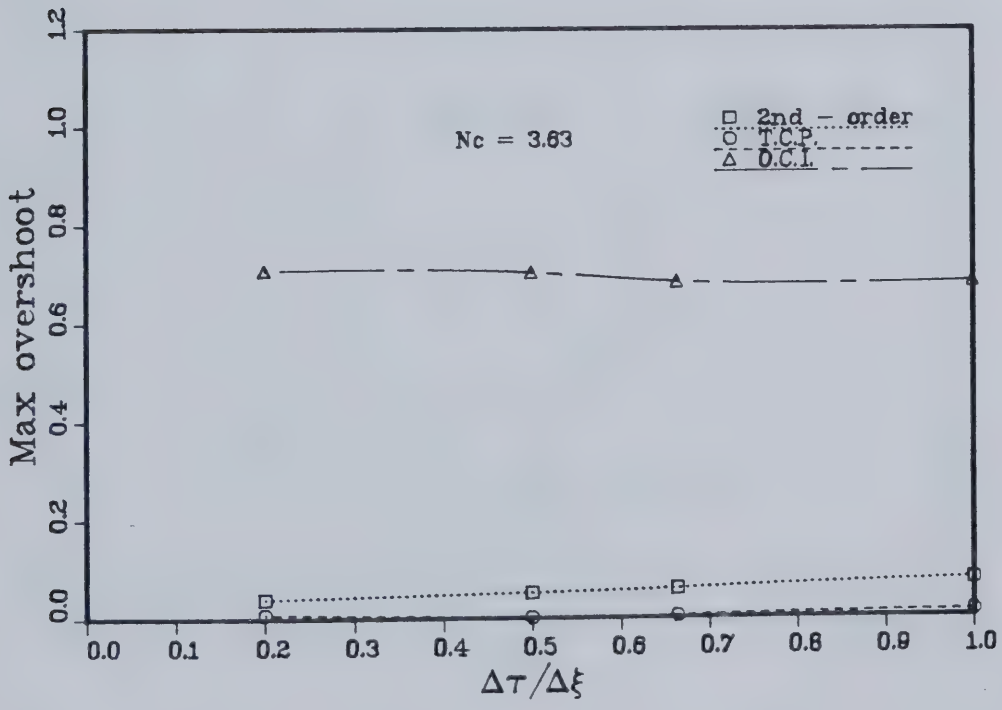
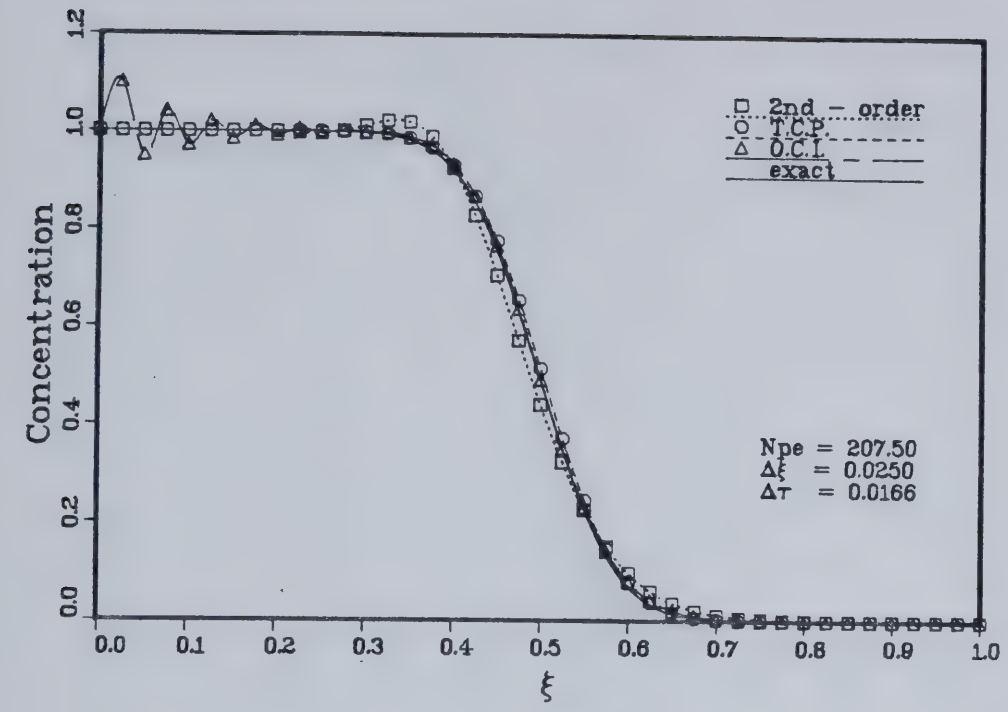


Figure 4.2-3 : OCI Instability - Lower Limit







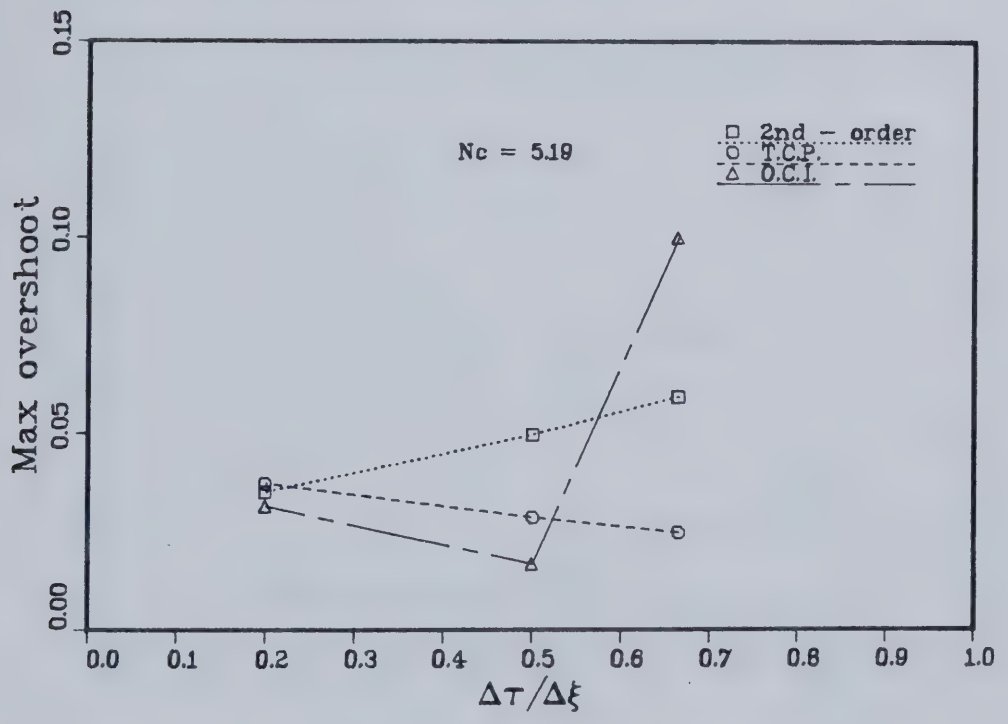
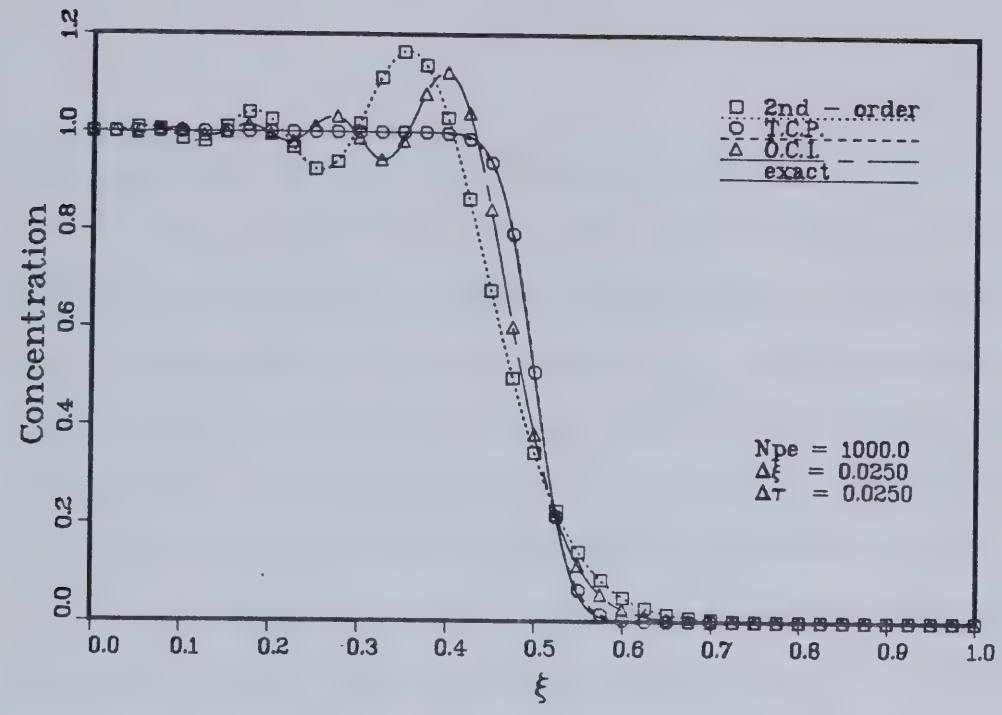


Figure 4.2-4 : OCI Instability - Upper Limit





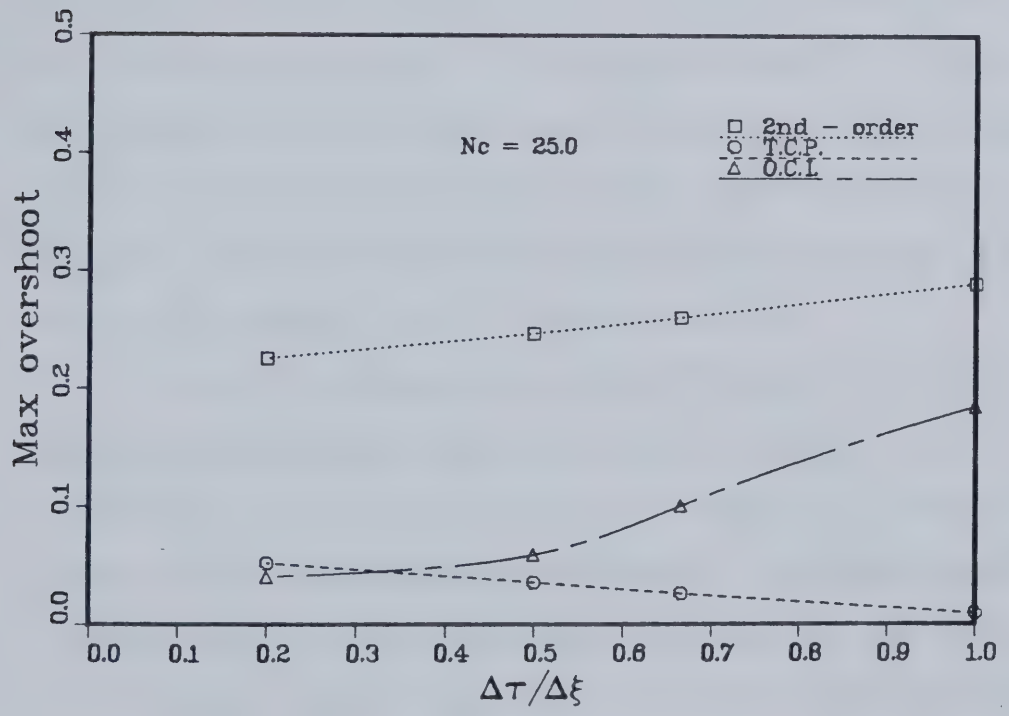
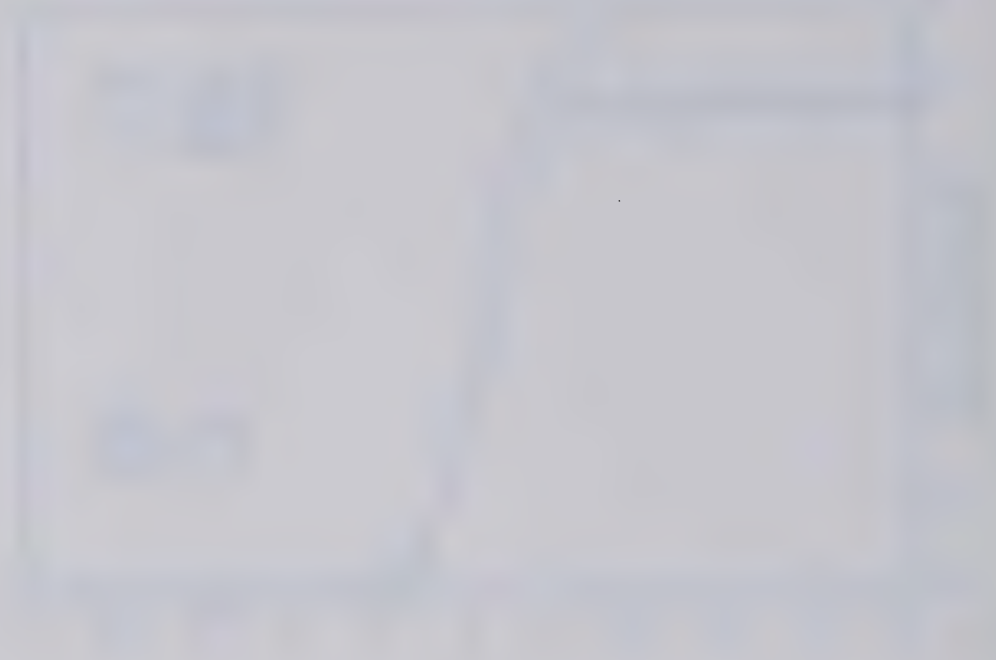


Figure 4.2-5 : Numerical Solutions - High Cell-Peclet Numbers





for a unit time-step to cell-dimension ratio.

These general observations are valid for finer grids. Finer grids provide a means to simulate at higher flow Peclet numbers, N_{Pe}, for a fixed stable cell-Peclet number, N_{Ce}. Mesh refinement improves the accuracy for all three methods, however at the expense of smaller time steps. A minimum grid density is required for OCI to function properly, whereas no set restriction is imposed for CDS and TCP.

All methods may exhibit small-time deviation. For convective dominant problems, this small-time behaviour results in concentrations predicted outside the physically acceptable bounds. The small-time effect is a numerical response to the initial discontinuities in the discrete representation of the propagating solvent-oil contact surface. All methods show similar small-time periods over which the numerical solution evolves into the stable profiles which track the exact solution. Tampering with small-time evolutionary process by truncating the overshoot will definitely produce erroneous results.

For this one-dimensional analysis the cell-Peclet number is the similarity group which governs convergence behaviour — be it absolute, oscillatory or divergent. The ratio of dimensionless time-step to normalized cell length governs the relative error from the exact solution where the absolute minimum error is set by the grid density.

A simple rule of thumb for the operating numerical conditions necessary to produce confident two-dimensional results can be established. The physical problem will produce flow-Peclet numbers for the geometries considered. An operating maximum component cell-Peclet number is chosen such that the specific method has absolute convergence for the

associated linear problem. The grid density required for simulation follows from the operating cell-Peclet number which in turn sets the upper bound for the dimensionless time step.

4.3. The Five Spot

Current simulation problems deal with multiwell flooding patterns for optimal recoveries. The five-spot pattern is the basis for many of these flooding projects. The quarter section element of symmetry may be mathematically represented by a point source and a point sink placed on the opposite corners of a square region bounded by an impermeable perimeter.

Spatial variations in the velocity field and the anisotropy of dispersion make it virtually impossible for any one scalar group to govern displacement similarity. Furthermore, nonlinearities would render a general Peclet tensor surface ineffective in scaling the multi-dimensional convective-diffusion equation. Since a general similarity group is not available, dimensionless subgroups influencing displacement must be isolated.

In order to define a dimensionless ratio of convection to diffusion rates, a characteristic length is essential. Normal cell-Peclet numbers may be defined pointwise using the grid partition. The relative magnitude of individual cell numbers depend on both block size and position, while endpoint velocities determine an absolute maximum.

For a fixed grid partition, the injection rate governs velocity maxima. An inlet cell-Peclet number follows readily from a symmetric partition.

$$N_{Ce_{IN}} = \left(\frac{u_x \Delta x}{D_{xx}}\right)_{IN} = \frac{q_{IN}}{D_{xx} \Delta z} \qquad 4.3(1)$$

Flow similarity requires partition independence and an inlet number is defined with the physical field dimension as the characteristic scaling length.

$$N_{Pe_{IN}} = \frac{q_{IN}}{D_{xx} \Delta z} (N_x - 1) \qquad 4.3(2)$$

The major factor influencing the shape of the velocity field and subsequently the Peclet curvature is the fluid mobility. An incompressible fluid with constant mobility flows along the streamlines of a Laplacian pressure field. For a homogeneous medium, the concentration dependent viscosity determines the fluid mobility. The ratio of component viscosities in the binary mixture provides a parametric measure for the mobility-induced departure from a Laplacian pressure field, and its effect on displacement similarity.

As the grain size approaches zero, dispersion diminishes leaving diffusion isotropic and constant. Dispersion effectively increases the apparent diffusion proportionately with the local velocity magnitude. The Peclet surface responds to dispersion by a global drop in magnitude with pronounced reduction about the local maxima.

A longitudinal Peclet number,

$$N_{Pe_\ell} = \frac{uL}{\left(\frac{D_0}{Fr} + \frac{1}{2} \sigma d_p u\right)} \qquad 4.3(3)$$

can be decomposed into molecular and dispersive counterparts.

$$N_{Pe_0} = \frac{uL}{(D_0/Fr)} \; ; \quad N_{Pe_u} = \frac{2L}{\sigma dp}$$

$$N_{Pe_\ell} = \frac{1}{\frac{1}{N_{Pe_0}} + \frac{1}{N_{Pe_u}}} \qquad 4.3(4)$$

The longitudinal number asymptotically saturates with increasing velocity magnitude. Higher injection rates elevate global velocity magnitudes such that local contributions from the molecular number become negligible, and the constant dispersion counterpart determines displacement similarity.

A laboratory scale model with the physical properties listed in Table 4.3-1 has been chosen as a basis for simulation. The dimensionless time, τ, corresponds to the pore volumes of fluid injected into the square region.

$$\tau = \frac{q_{IN}t}{\phi_m L^2 \Delta z} \qquad 4.3(5)$$

Figure 4.3-1 illustrates the effects of injection rate on displacement similarity in a Laplacian field with isotropic diffusion. Each grey-level frame represents the concentration distribution with solvent (white) displacing oil (black) at the corresponding injection time, τ. At low injection rates, diffusion dominates with marked radial propagation at both inlet and outlet. Higher injection rates bring forth convective dominance with the formation of a sharp front in the concentration surface. The radial advance in the early stages is succeeded by the delayed breaking of the solvent front to the sink.

L	= 30 cm
W	= 30 cm
Δz	= 5 cm
ϕ	= .33
k_x	= 1 darcy
k_y	= 1 darcy
μ_s	= 1 cp
ρ_s	= 1 gm/cm^3
ρ_o	= 1 gm/cm^3
D_0	= $10^{-5} cm^2/sec$
F_r	= 4
σ	= 3.5

Table 4.3-1: Miscible Displacement Simulation

Data Set 1

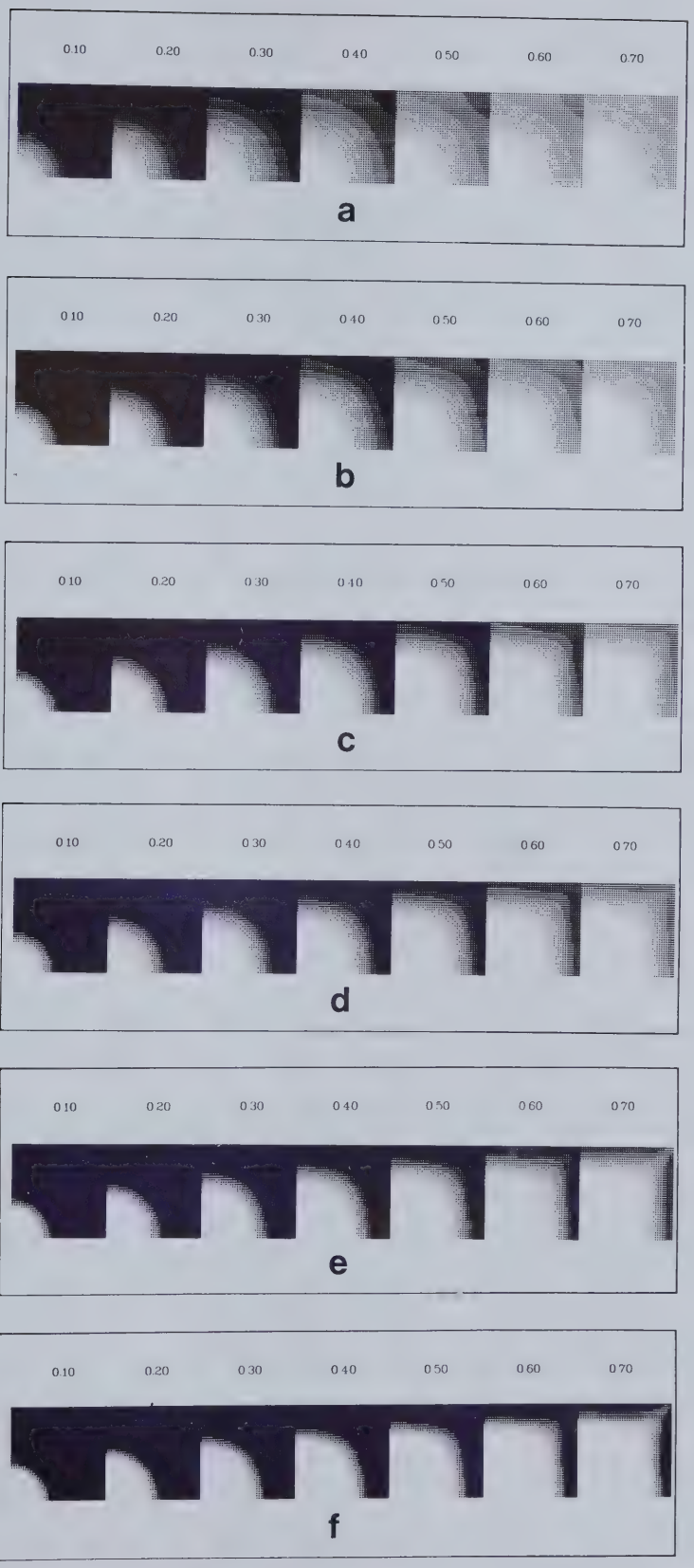


Figure 4.3-1 : Displacement Similarity - Injection Rate Effects

	q_{IN} (cm^3/sec)	(N_x, N_y)	$N_{Pe_{IN}}$
a)	$.5*10^{-4}$	(11,11)	40
b)	$1*10^{-4}$	(11,11)	80
c)	$1*10^{-4}$	(21,21)	160
d)	$2*10^{-4}$	(21,21)	320
e)	$4*10^{-4}$	(21,21)	640
f)	$8*10^{-4}$	(21,21)	1280

Table 4.3-2 : Displacement Similarity - Injection Rate Effects

(cf. Table 4.3-1 ; $d_p = 0$, $\mu_o/\mu_s = 1$)

Higher convection rates reduce the sweep efficiency with larger oil deposits remaining at breakthrough.

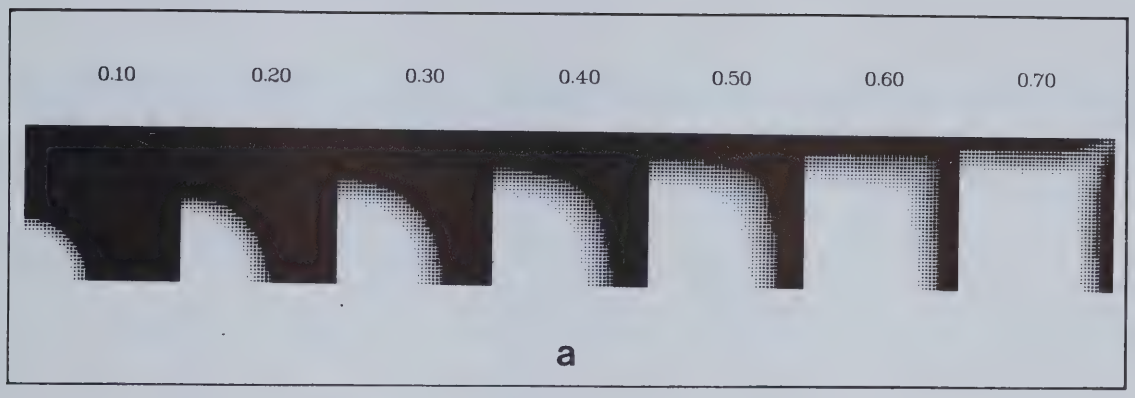
With the injection rate fixed for convective dominance, Figure 4.3-2 illustrates the effect of dispersion. Increasing the particle diameter instigates the formation of a sharp cusp at the leading edge of the front, prior to breakthrough. Further increase in injection rate, sharpens the cusp till asymptotic similarity prevails [cf. Figure 4.3-3].

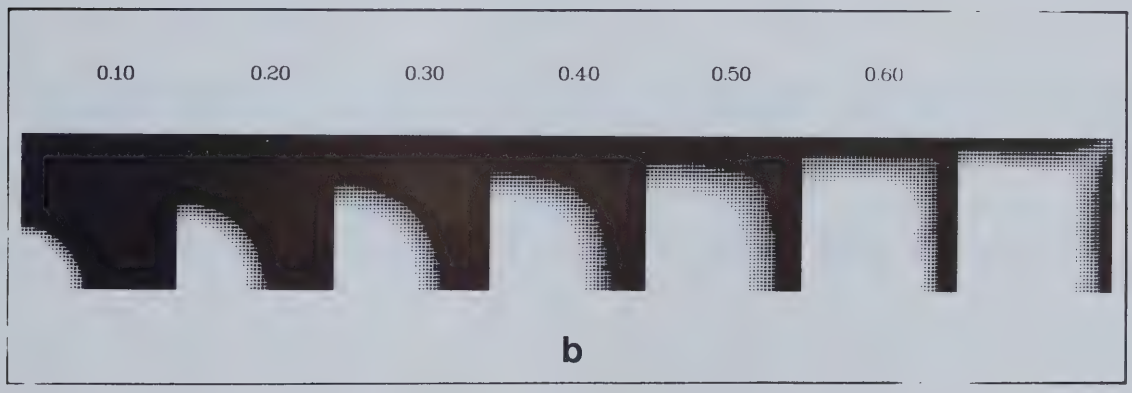
Solvent injection of .0025 pore volumes over each time step was used for the (21×21) partitions. Figure 4.3-4 shows the TCP predicted concentration surface for a convective dominant displacement, prior to breakthrough. Small-time oscillations were completely damped within the first few time steps to give this stable representation.

4.4. Grid Orientation and Viscosity Effects

A diagonal grid represents the quarter section element of symmetry with the injector-producer geodesic along the square diagonal, oriented at $45°$ to the grid lines. The physically identical flow system can also be represented by a parallel grid, with the grid lines either parallel or perpendicular to the injector-producer geodesic. The parallel grid corresponds to one half of a five spot pattern, where the grid boundaries map onto the symmetry planes defined by the geodesics [cf. Figure 4.4-1].

The nonuniqueness of finite difference solutions for different grid orientations was first demonstrated by Todd et al.[15]. Finer grid definition does not necessarily alleviate the grid orientation problem,





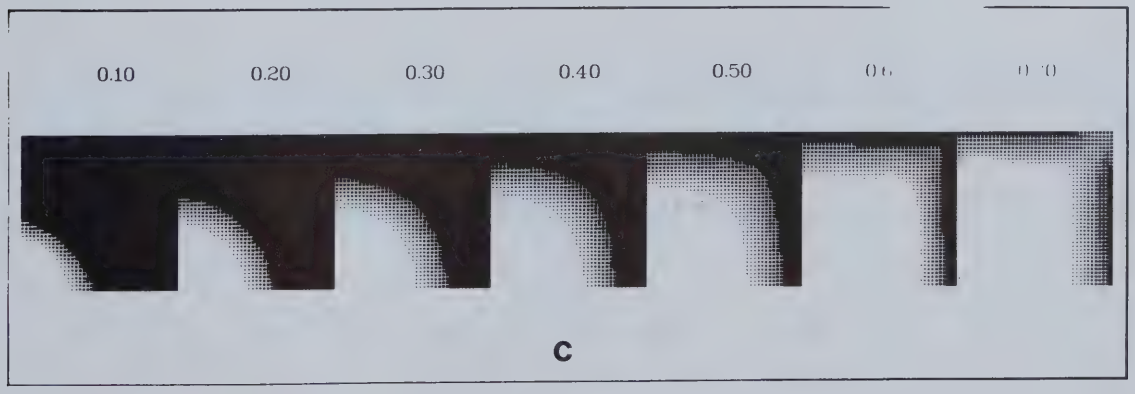
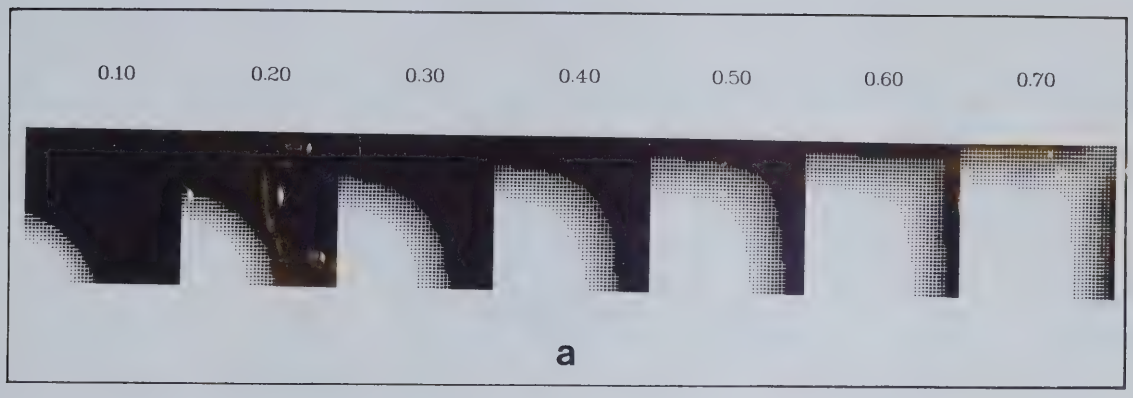


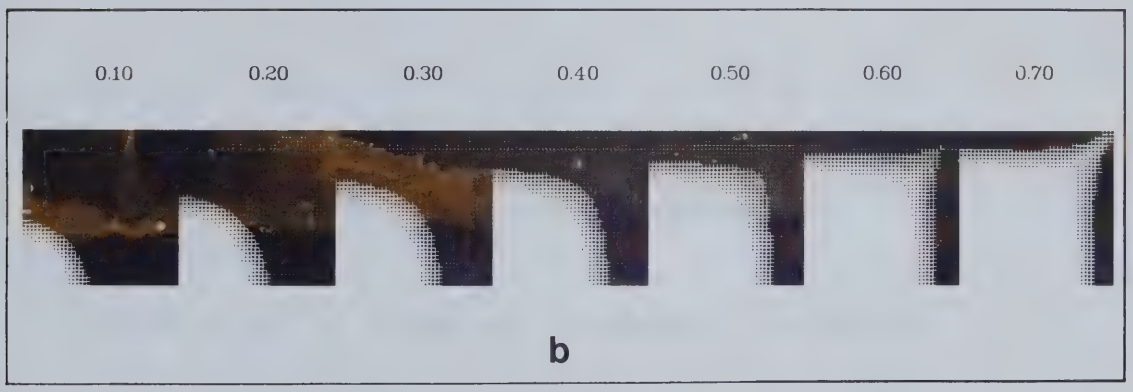
Figure 4.3-2 : Displacement Similarity - Dispersion Effects

	d_p (cm)	(N_x, N_y)	$N_{Pe_{IN}}$
a)	.0	(21,21)	1280.
b)	.02	(21,21)	513.
c)	.2	(21,21)	80.

Table 4.3-3 : Displacement Similarity - Dispersion Effects

(cf. Table 4.3-1 ; $q_{IN} = 8.*10^{-4} cm^3/sec$, $\mu_o/\mu_s = 1$)





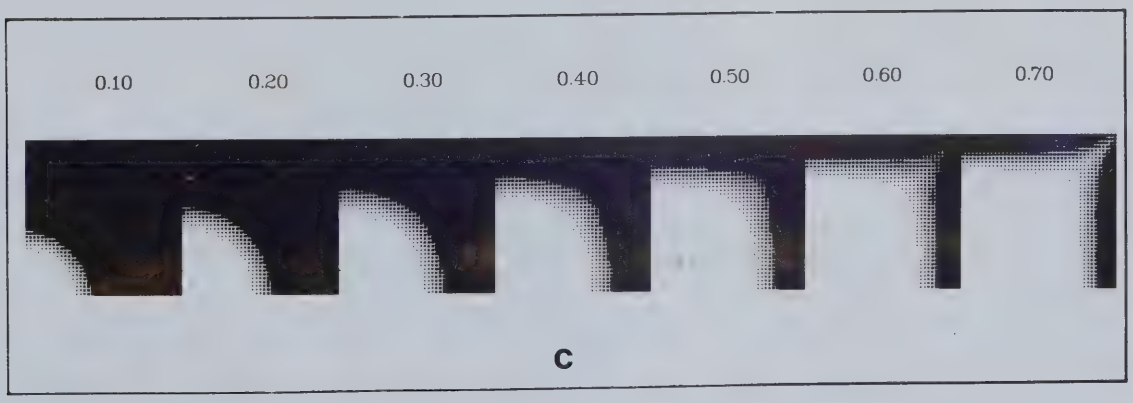
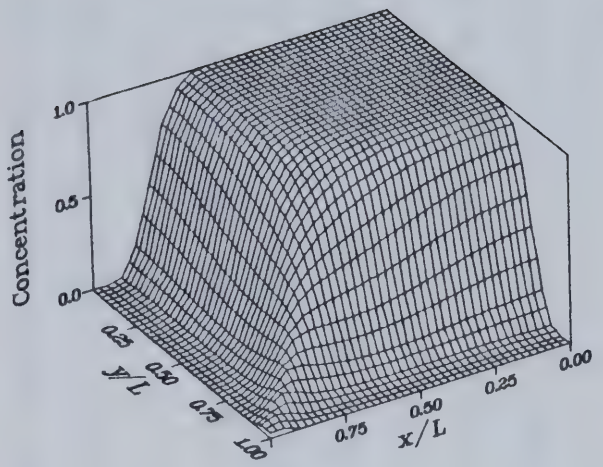


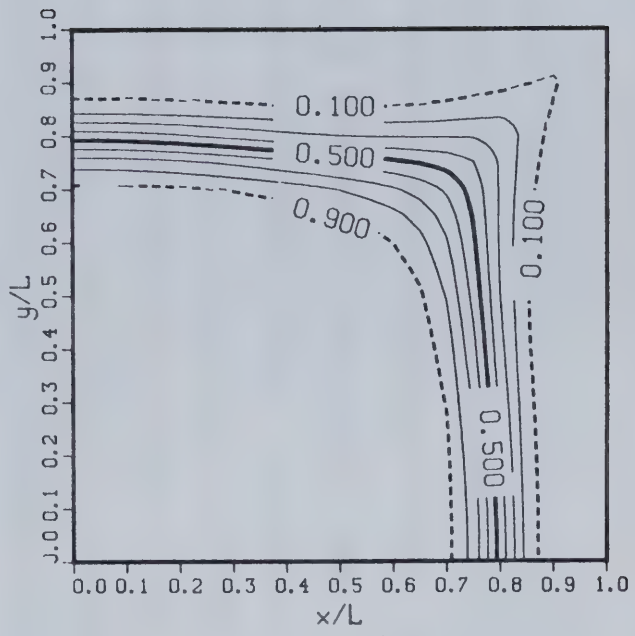
Figure 4.3-3 : Asymptotic Displacement Similarity

	q_{IN} (cm^3/sec)	(N_x,N_y)	$N_{Pe_{IN}}$
a)	$8.*10^{-4}$	(21,21)	80.3
b)	.025	(21,21)	85.5
c)	1.0	(21,21)	85.7

Table 4.3-4 : Asymptotic Displacement Similarity

(cf. Table 4.3-1 ; d_p= .2 cm , μ_o/μ_s= 1)





Injected Solvent = 0.6 pore volumes

Figure 4.3-4 : The Stable TCP Solution for Convective Dominant Displacements



with diagonal and parallel simulations predicting two different displacement histories. Adverse mobility ratios aggravate the deviation, which is most apparent in five-point finite difference schemes.

Numerous attempts have been made to eliminate the grid orientation effect, none of which is entirely satisfactory.[36] All five-point schemes experience orientation problems at higher viscosity ratios, independent of the mobility approximation used.

Aside from the nonuniqueness, frontal instabilities may develop in either orientation. An early indentation of the leading displacement edge may evolve into numerical fingers [cf. Figure 4.4-2]. Mild numerical fingering produces an inverted cusp which may disappear if diffusion is sufficiently large to equalize transverse gradients. As convective forces dominate, numerical fingers develop about the symmetry plane, leaving unswept oil along the diagonal geodesic. These anomalies are not exclusive to five-point schemes, and similar finger-like features have been reported for nine-point methods.[34]

When diffusion is small, different modes of numerical fingering can be observed [cf. Figure 4.4-3]. The solvent preferentially moves along the confining walls, with multiple secondary fingers at higher viscosity ratios, bypassing the central oil in place.

The unstable phenomenon was generated with arithmetic approximations for mean mobilities and diffusivities on a diagonal grid. Similar effects can be observed on a parallel grid with breakthroughs predicted earlier for a wider stability range. Parallel grids are more attractive for moderately adverse viscosity ratios, however instabilities

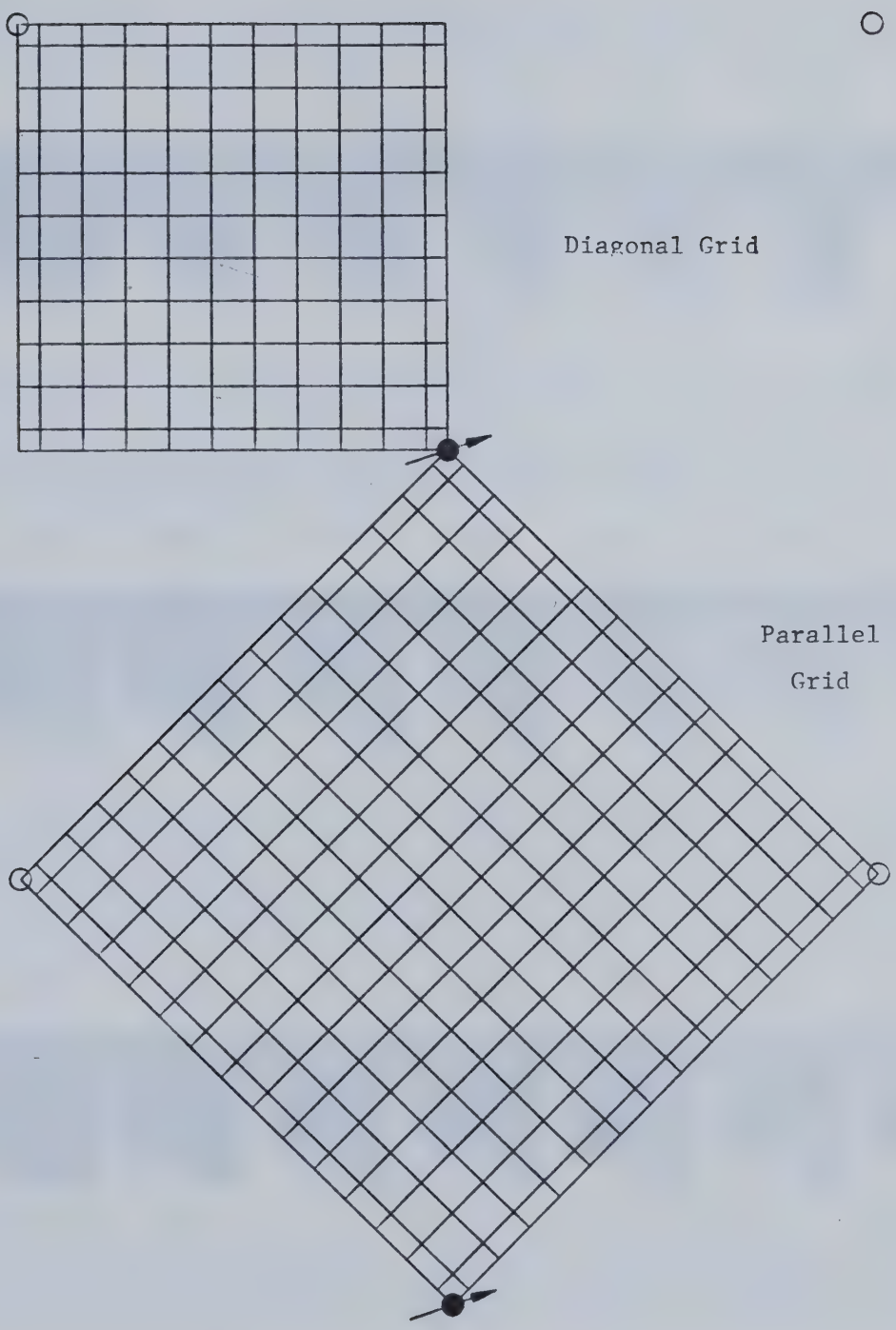


Figure 4.4-1 : Diagonal and Parallel Grids

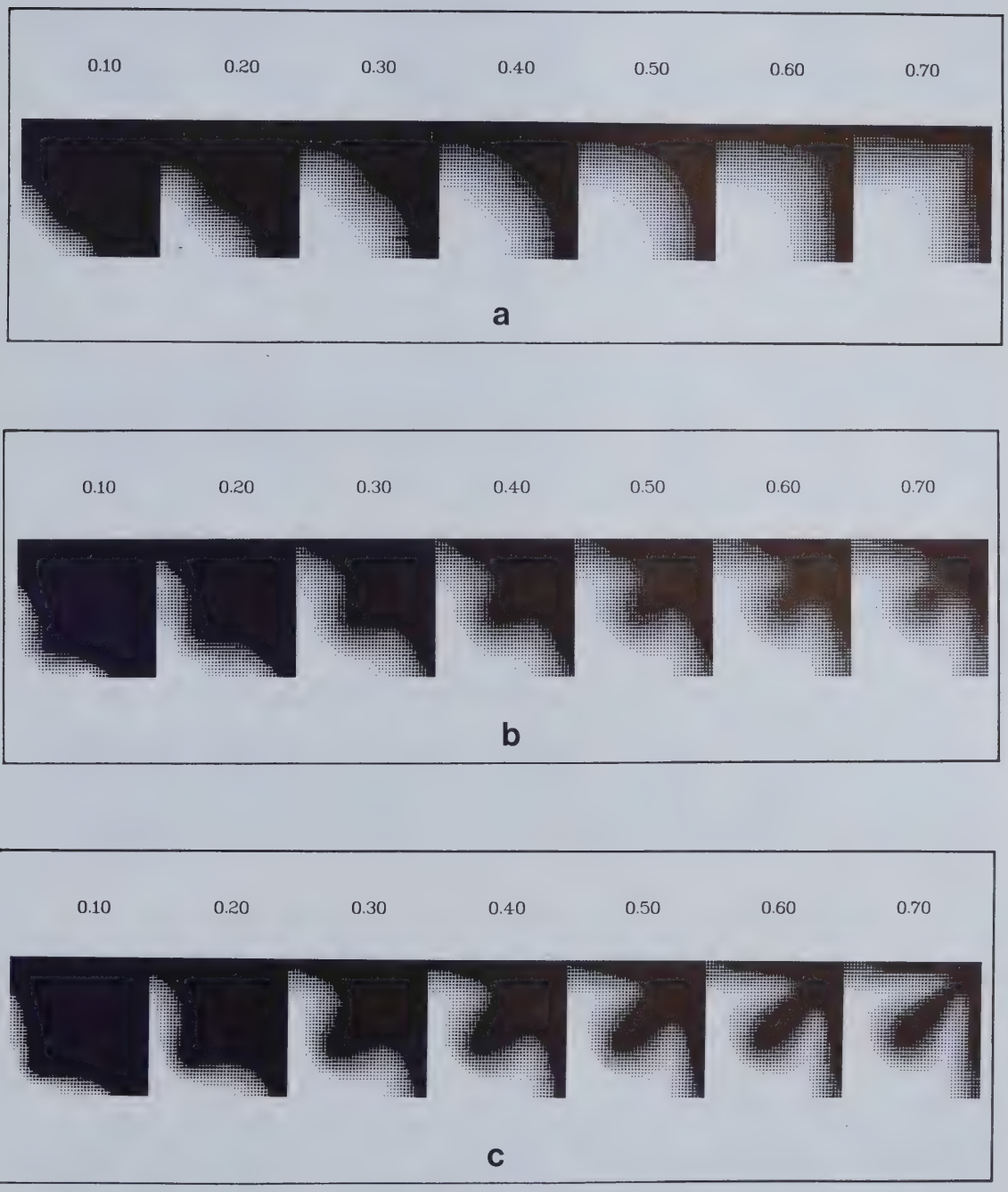


Figure 4.4-2 : Numerical Fingering

	q_{IN} (cm^3/sec)	(N_x, N_y)	$N_{Pe_{IN}}$
a)	$1*10^{-4}$	(21,21)	13.5
b)	$4*10^{-4}$	(21,21)	36.6
c)	$8*10^{-4}$	(21,21)	51.3

Table 4.4-1 : Numerical Fingering

(cf. Table 4.3-1 ; $D_0 = 10^{-4} cm^2/sec$, $d_p = .2$ cm , $\mu_o/\mu_s = 100$)

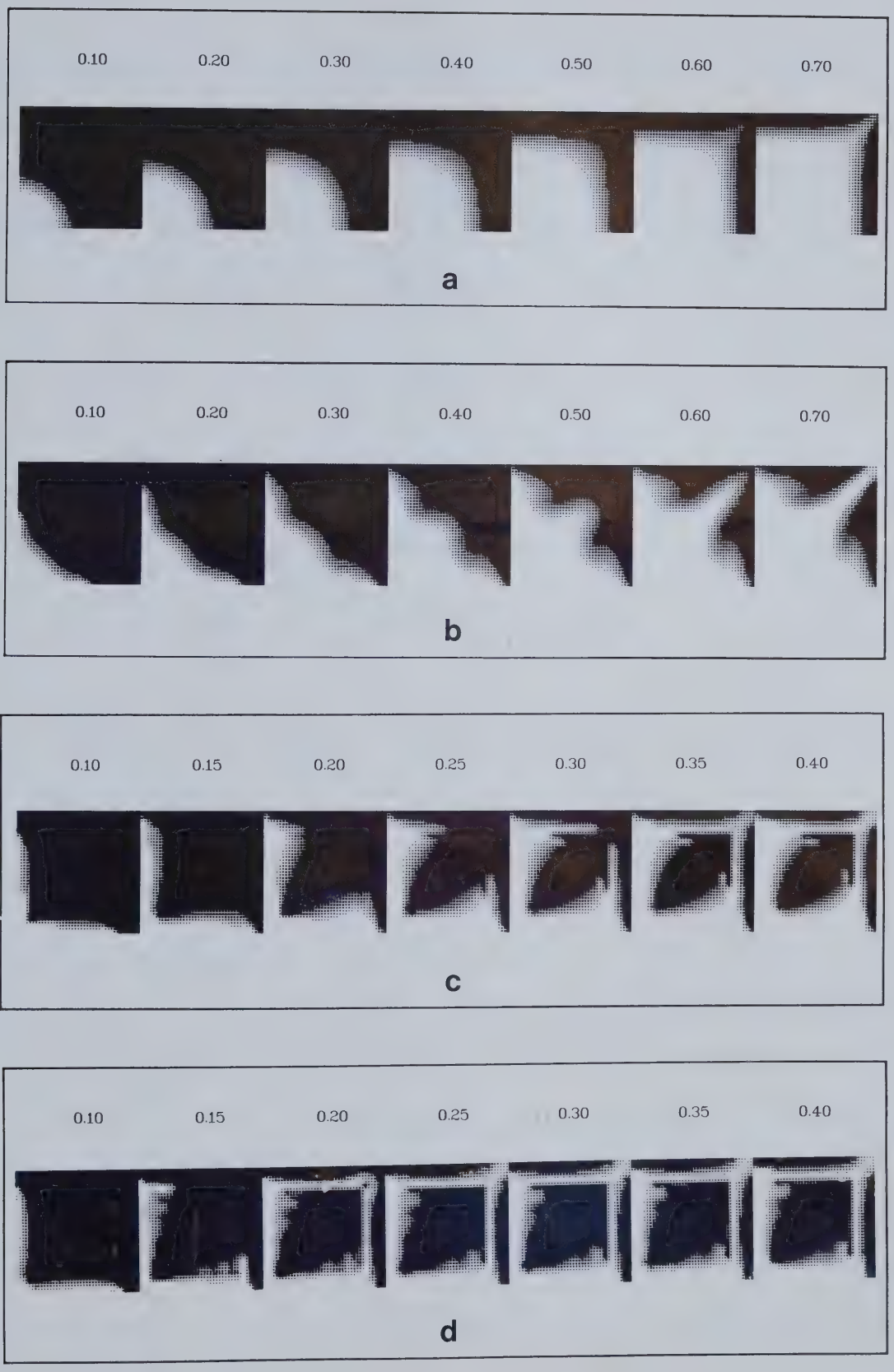


Figure 4.4-3 : Modes of Numerical Fingering

	μ_o/μ_s	(N_x,N_y)	$N_{Pe_{IN}}$
a)	1	(21,21)	85.5
b)	10	(21,21)	85.5
c)	100	(21,21)	85.5
d)	1000	(21,21)	85.5

Table 4.4-2 : Modes of Numerical Fingering

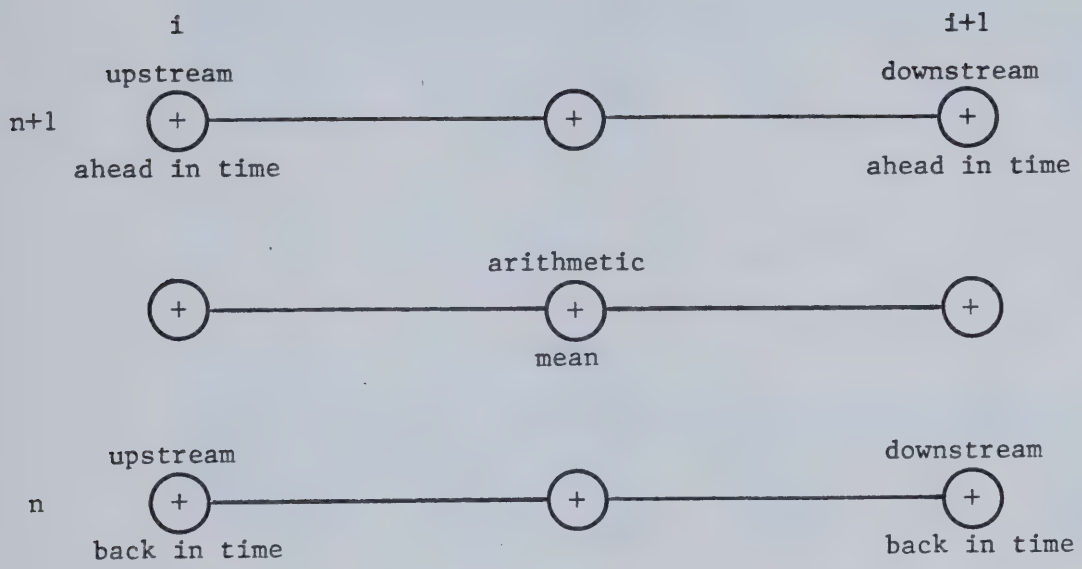
(cf. Table 4.3-1 ; d_p = .2 cm , q_{IN} = .025 cm^3/sec)

render arithmetic mobilities ineffective for realistically predicting grossly unfavourable displacements.

Mobility-diffusivity approximations, compatible with the grid orientation, are sought for the realistic predication of displacement fronts over a range of viscosity ratios, extending into the tar sand regime. The "realistic" criterion excludes any displacement whose leading edge deviates from the fastest streamline, defined by the minimum energy geodesic connecting injector to producer. Simply, the occurrence of any frontal instability resulting in numerical fingering is rejected.

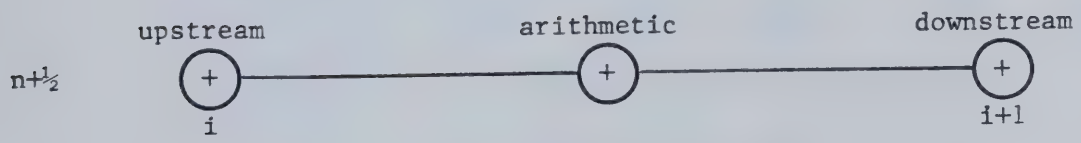
Mathematically, midpoint mobilities evaluated at the midtimes are allowed to take on any value within a bounded uncertainty interval $(\Delta x,\Delta t)$ [cf. Figure 4.4-4]. Similarly, midpoint diffusivities lie within a spatial uncertainty interval fixed at the mid-time. Suitable weightings are required to relate mid-values to existing grid points in space-time. Many options are available, with specific weightings labelled in Figure 4.4-4.

Numerical experimentation isolated the downstream, back in time approximation with diagonal grid orientation as the only compatible configuration for realistic displacements, over the desired range of viscosity ratio. Any other weighting, or change in grid orientation, resulted in some anomaly for the displacement conditions investigated. The compatible approximation predicts stable fronts with channel formation at extreme ratios [cf. Figure 4.4-5]. Realistic displacements show diminishing sweep efficiencies, with advanced breakthroughs, at higher viscosity ratios.



Mobility Uncertainty





Diffusivity Uncertainty

Figure 4.4-4 : Mobility-Diffusivity Approximations

L	= 21.2. cm
W	= 21.21 cm
Δz	= 5 cm
ϕ	= .33
k_x	= 1 darcy
k_y	= 1 darcy
μ_s	= 1 cp
ρ_s	= 1 gm/cm^3
ρ_o	= 1 gm/cm^3
D_0	= $10^{-4} cm^2/sec$
F_r	= 4
σ	= 3.5

Table 4.4-3: Miscible Displacement Simulation

Data Set 2

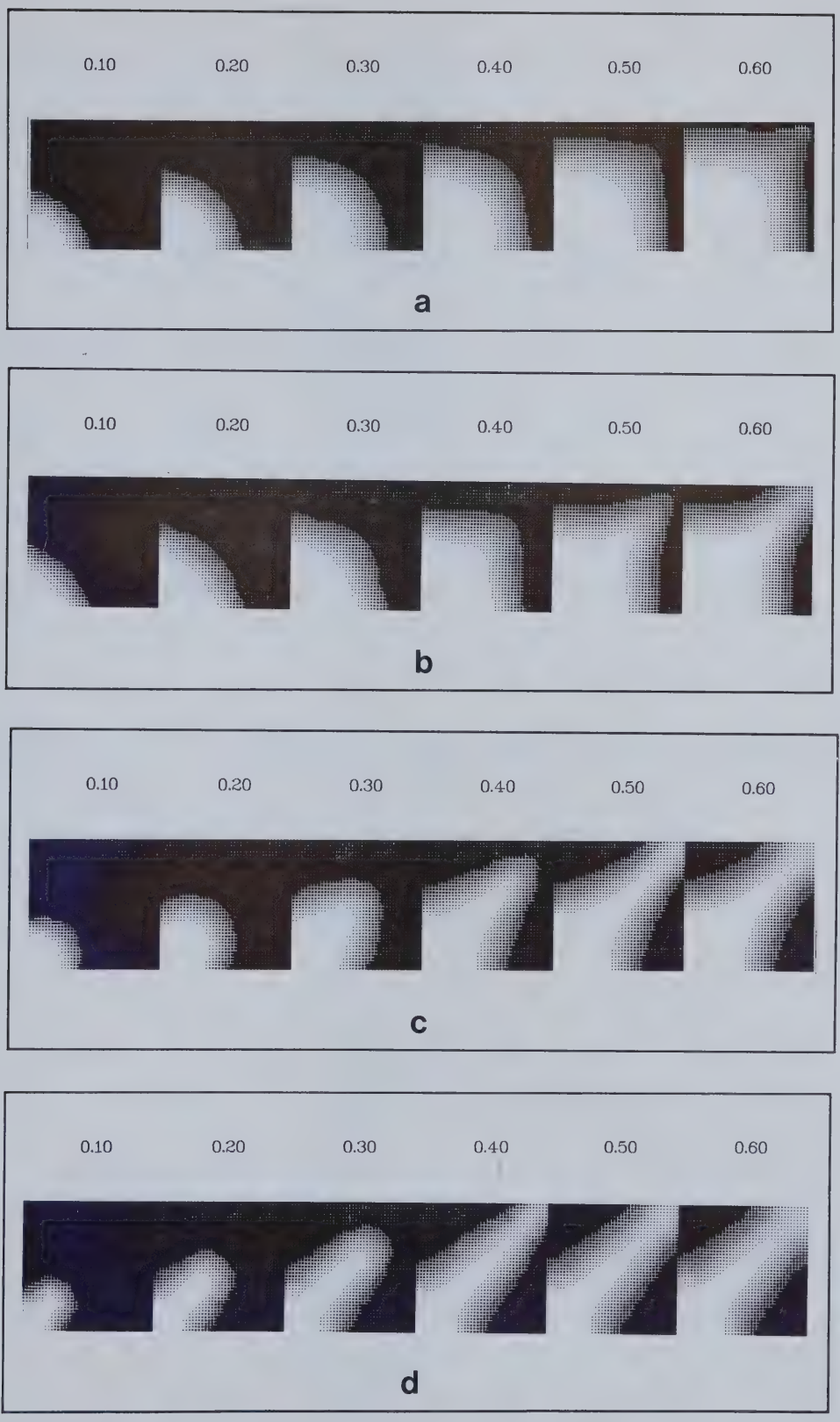


Figure 4.4-5 : Displacement Similarity - Viscosity Effects

	μ_o/μ_s	(N_x,N_y)	$N_{Pe_{IN}}$
a)	1	(11,11)	52.6
b)	10^2	(11,11)	52.6
c)	10^4	(11,11)	52.6
d)	10^6	(11,11)	52.6

Table 4.4-4 : Displacement Similarity - Viscosity Effects

(cf. Table 4.4-3 ; d_p = .2 cm , q_{IN} = .005 cm^3/sec)

Figure 4.4-6 illustrates realistic viscous fingers at lower diffusion rates. Fingers develop early in the displacement with the central finger outgrowing the others. Once the finger develops, it does not grow to a point but forms a rather blunt front. The same statements are quoted by Habermann[44] for an experimental study conducted in 1960. Although the simulation model-characteristics differ, the predicted results have definite similarities to specific experimental runs at considerably lower mobility ratios. Of these similarities, the most prominent is the early separation of the fingers from the confining walls.

Even though stable fronts are predicted, the existence of a single approximation compatible with a specific orientation does not guarantee the validity of simulated results. One must keep in mind, these are approximate solutions only, and simulated results must be scrutinized thoroughly, before acceptance.

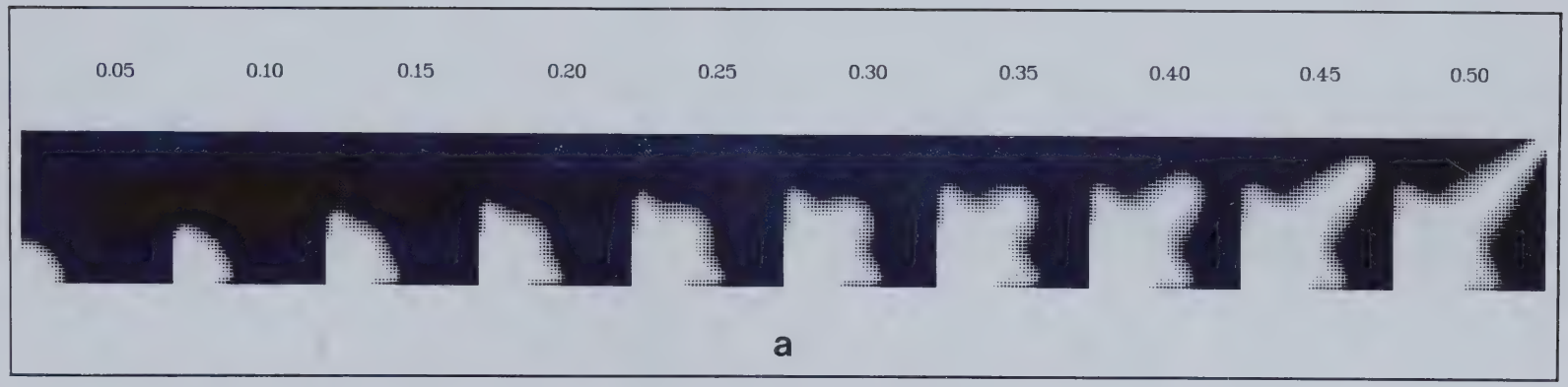


Figure 4.4-6 : Viscous Fingering

	μ_o/μ_s	q_{IN} (cm^3/sec)	(N_x,N_y)	$N_{Pe_{IN}}$
a)	100	.005	(21,21)	60.5

Table 4.4-5 : Viscous Fingering

(cf. Table 4.4-3 ; $D_0 = 10^{-5} cm^2/sec$, $d_p = .2$ cm)

CHAPTER FIVE

LEACHING

Single-cell dissolution provides insight into the phase behaviour of the closed solid-liquid system. Two mechanisms govern dissolution kinetics — solvent adsorption and solvent absorption. Adsorption is the surface phenomenon responsible for the driving force behind dissolution. Absorption is internal, solid-phase, solvent accumulation, and may produce an initial swelling.

Solid-phase activity competes with miscible displacement for leaching status. The leaching process is initially dominated by dissolution, followed by a progressive miscible drive. Time scaling dissolution with displacement is crucial for simulation. Simulation predicts increased leaching efficiency for solvents with higher adsorption coefficients.

5.1. Single-Cell Dissolution

The special case of uniform sphere radii in a liquid with initial concentration, C_0, devoid of convection currents, constitutes the single cell dissolution of bitumen. The fluid pressure is constant, and dispersion rapid, such that spatial dependence disappears leaving the state vector (C,r_p) with time dependence only. The system void of solvent sources can be modelled by the radial dissolution equation coupled with the adsorption equation.

$$C^* \frac{\partial}{\partial t} \left\{ r_0 F(t) + \int_0^t \dot{r}_p(\tau) F(t-\tau) d\tau \right\} - 4\pi r_p^2 [C\dot{r}_p + \alpha(C-C^*)] = 0$$

$$(\phi_m - \frac{4\pi}{3} N_p r_p^3) \frac{\partial C}{\partial t} + 4\pi r_p^2 N_p [\alpha(C-C^*)] = 0 \qquad 5.1(1)$$

By introducing the dimensionless variables,

$$t_d = \frac{D_s t}{r_0^2}$$

$$r_d = \frac{r_p}{r_0} \qquad 5.1(2)$$

$$F_d = \frac{F}{4\pi r_0^2}$$

the transformed dissolution and adsorption equations have the respective dimensionless forms,

$$r_d^2 \left[r_d C + N_{Da}(C-C^*) \right] - C^* \frac{\partial}{\partial t_d} \left\{ F_d + \int_0^{t_d} \dot{r}_d(\tau) F_d(t_d-\tau) d\tau \right\} = 0$$

$$[1 - (1-S_0) r_d^2] \frac{\partial C}{\partial t_d} + 3(1-S_0) r_d^2 N_{Da}(C-C^*) = 0 \qquad 5.1(3)$$

where S_0 is the initial liquid saturation and the Damköhler number, N_{Da}, is the characteristic ratio of the solvent adsorption rate from the liquid phase to the solvent diffusion rate into the interior of the solid.

$$N_{Da} = \frac{\alpha r_0}{D_s} \qquad 5.1(4)$$

The state vector (C,r_p) determines the phase behaviour of the closed system for a given initial liquid saturation. Dissolution kinetics are governed by two mechanisms — solvent absorption and solvent adsorption.

The accumulation term of the radial dissolution equation determines solvent absorption from the liquid phase with the critical concentration, C*, as the capacitance. In the absence of adsorption $(N_{Da} = 0)$, absorption will yield an increase in solid mass as a result of internal solvent diffusion bounded by the critical $(C_s \leq C^*)$. The swelling characteristics of solvent absorption are shown in Figure 5.1-1, as a function of the capacitance. The saturation asymptotes reflect a solvent saturated solid to full capacity. The constant concentration signifies the absence of bitumen desorption. A maximum swell capacitance is determined from the lower bound to the equilibrium saturation, S_e,

$$C^* = \left(\frac{S_0 - S_e}{1 - S_e}\right) C_0 \qquad 5.1(5)$$

above which, pore space is not available to accomodate full solid expansion and the absorption process must be truncated at the zero liquid saturation.

Adsorption is the driving mechanism for the dissolution process. As solvent is adsorbed into the solid, the local concentration is forced above the critical. That portion above the critical undergoes a non-reversible phase change resulting in the dissolution of solid material. As dissolution proceeds, the liquid concentration drops indicating

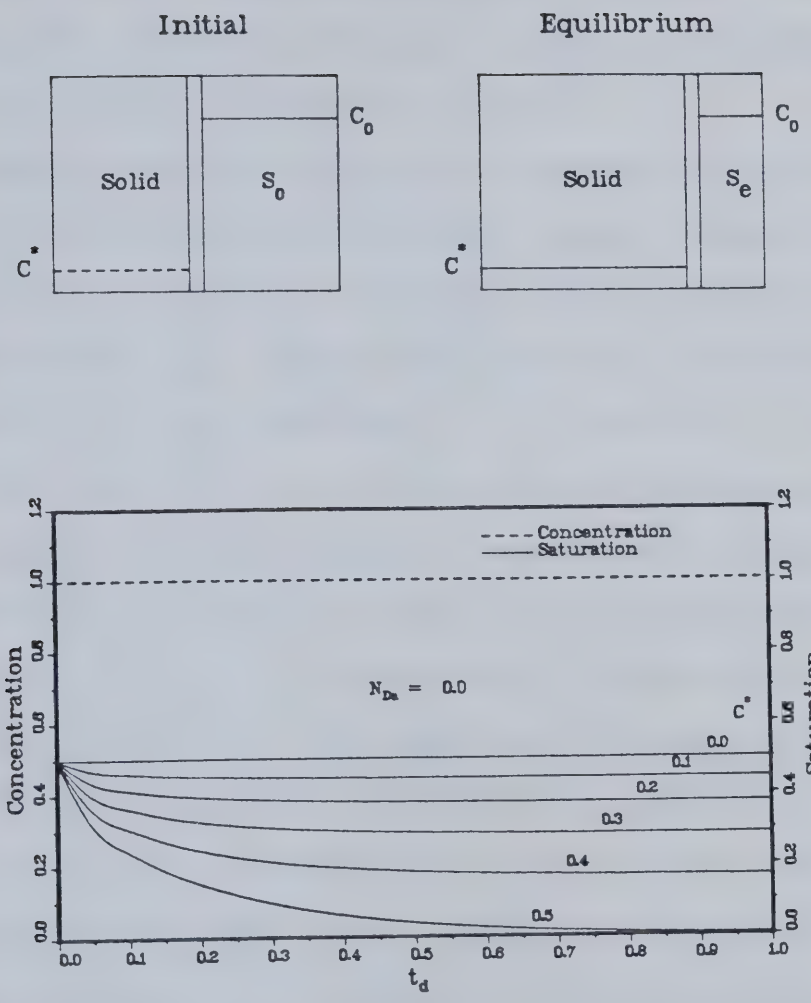


Figure 5.1-1 : Swelling - Solvent Absorption

bitumen desorption (solvent adsorption). An equilibrium concentration is reached when the solid phase is completely dissolved. Figure 5.1-2 illustrates the dissolution curves as a function of the Damköhler number in the absence of absorption ($C^* = 0$).

When the absorption rate exceeds the adsorption rate, an initial swelling is followed by rapid dissolution. Rapid dissolution is a consequence of the adsorption-perturbed absorption-elevated concentration level within the solid. Figures 5.1-3 (a) and (b) illustrate this phenomenon for non zero capacitance, $C^* = .2$ and $C^* = .4$, respectively.

The linear adsorption assumption poses difficulties about the zero radius. Dissolution must terminate at the zero radius, hence the integro-differential equation is valid only while solid material exists. After the dissolution of all solid material, a zero radius must prevail. The overshoots observed in these figures are a response of the curve fitting routine to the imposed dissolution discontinuity.

The slightest perturbation of a solvent saturated solid will create an avalanching phase change. Figure 5.1-4 illustrates such dissolution avalanches, for a low initial saturation with high capacitance. Adsorption decreases rapidly as the liquid concentration approaches the critical, leaving absorption to elevate internal concentration levels to the critical. Further adsorption "tips the balance" resulting in a massive dissolution drive.

Single-cell dissolution involves a closed system without additional solvent sources, which may be physically interpretted as the dissolution of tar sand in a laboratory beaker. Leaching, however, incorporates a multitude of interconnected cells with some local solvent

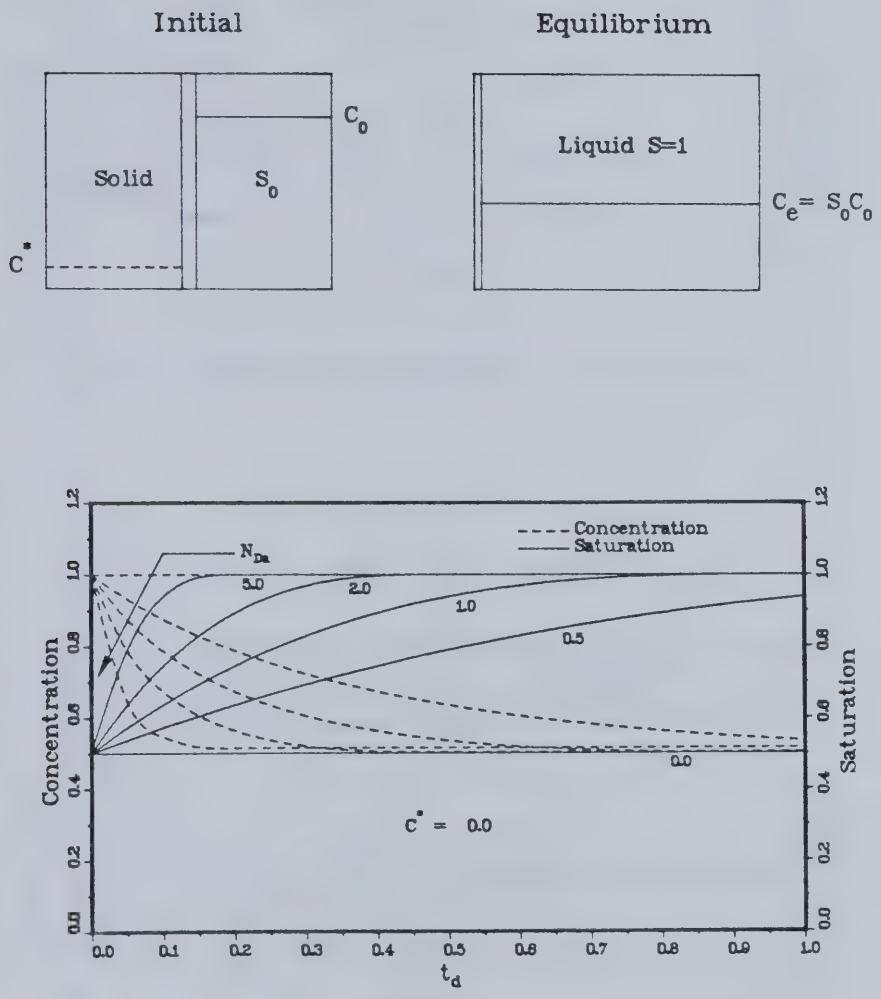
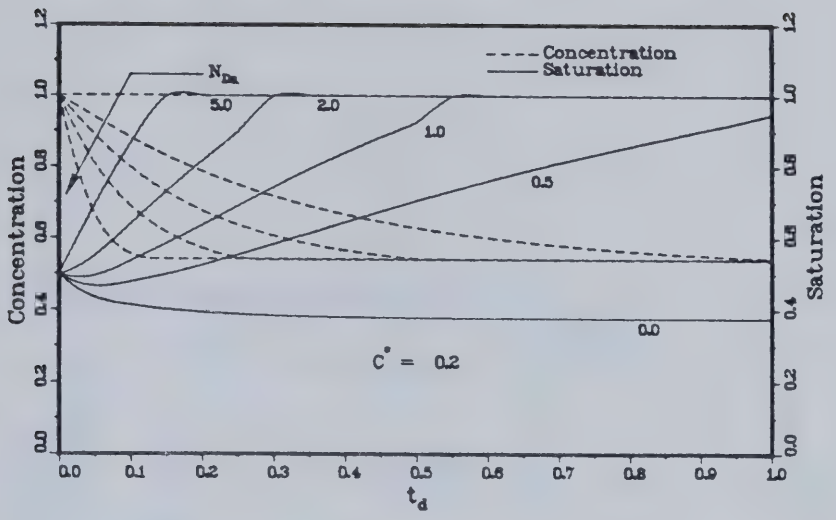


Figure 5.1-2 : Dissolution - Solvent Adsorption



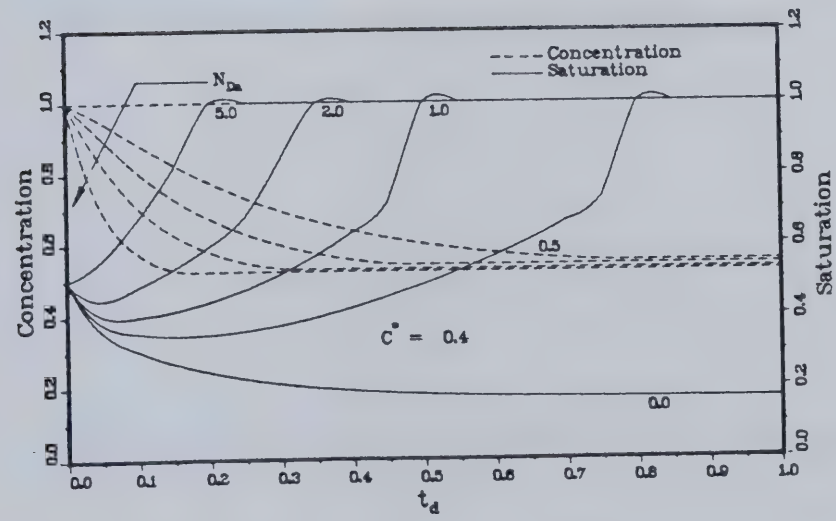


Figure 5.1-3 : Dissolution - Combined Adsorption with Absorption

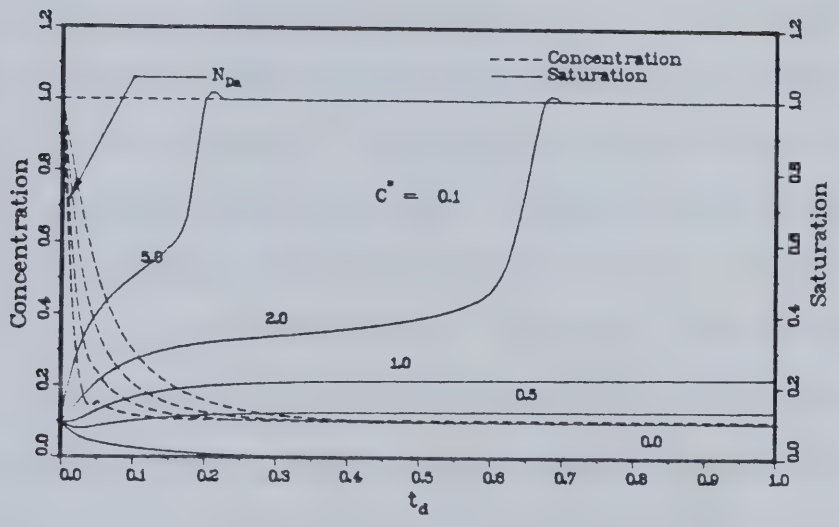


Figure 5.1-4 : Dissolution Avalanching - High Capacitance

source being dissipated by both convective and dispersive mechanisms.

5.2. Damköhler Effects

Solid phase activity competes with miscible displacement for solvent. Initially constricted flow within the bitumen saturated sands allows rapid solvent absorption into the solid. After a short period of initial swelling, a dissolution driven non-reversible phase change increases liquid pore space. The upstream constrictions are gradually relieved, and freshly injected solvent accumulates upstream while fluid transport carries dissolved bitumen downstream. A dissolution wave trails the sluggish displacement, creating a high porosity zone with increased mobility. Upstream dissolution is driven by adsorption while absorption elevates downstream solid-phase concentration levels. Downstream solid activity responds to the fresh upstream solvent with accelerated rapid dissolution ultimately equalizing the saturation gradient. A burst of dissolved bitumen becomes apparent in the effluent, and dissolution terminates with the completion of total phase inversion. A progressive miscible drive follows to displace the remaining bitumen in solution.

Pressures peak high in response to initially low injectivities. As dissolution proceeds, the pressures drop exponentially raising the injectivities by several orders of magnitude.

Many factors influence the leaching process. Time scaling dissolution with displacement is crucial for resolution of the saturation history. The dimensionless time ratio,

$$\frac{t_d}{\tau} = \frac{D_s \phi_m LW\Delta z}{r_0^2 \, q_{IN}} \qquad 5.2(1)$$

relates the dissolution time scale to the pore volumes of solvent injected, giving an upper bound for the simulation time necessary to resolve saturation histories.

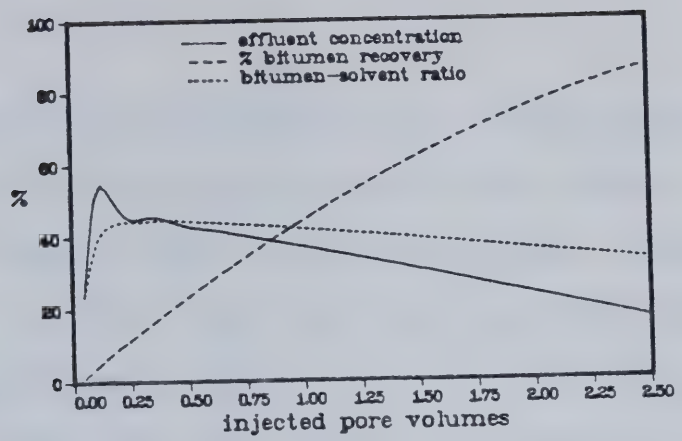
A laboratory scale five-spot model whose characteristics are listed in Table 5.2-1 is chosen as a basis for simulation, giving a dimensionless time ratio $(t_d/\tau = .3)$ sufficient to resolve dissolution within the first pore volume of injection.

An initial solvent invasion saturation is chosen as $S_0 = .05$, such that a maximum swell capacitance can be fixed accordingly to $C^* = .05$. Simulations were executed at different adsorption rates, showing the Damköhler effect on the leaching process. Figure 5.2-1 graphs predicted production data for (a) $N_{D_a} = 1$, (b) $N_{D_a} = 2$ and (c) $N_{D_a} = 5$. All three runs illustrate a sharp increase in effluent bitumen as a result of initial dissolution, followed by a gentle decline due to displacement. The first peak represents a stabilized system where the miscible drive balances bitumen desorption. As dissolution progresses, increased upstream porosity causes solvent to accumulate in the liquid phase. This accumulation drives downstream dissolution to completion, producing a second ripple in the effluent bitumen.

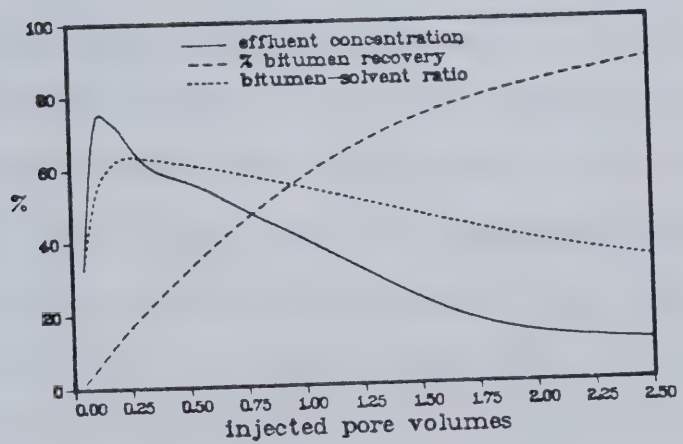
As the desorption rate increases with Damköhler number, rapid bitumen accumulation in the effluent causes a lower relative displacement activity. This is reflected by the higher peaks in the effluent

$L = 30$ cm	$D_0 = 10^{-4}$ cm^2/sec
$\Delta z = 5$ cm	$d_p = .2$ cm
$\phi_m = .33$	$F_r = 4.0$
$k_{x_0} = k_{y_0} = 10$ darcy @ $\phi_0 = \phi_m$	$\sigma = 3.5$
$\rho_s = \rho_o = 1$ gm/cm^3	$D_s = 10^{-8}$ cm^2/sec
$\mu_s = 1$ cp	$r_0 = .1$ cm
$\mu_o = 10^6$ cp	$C^* = .05$
$q_{IN} = .005$ cm^3/sec	= (a) 10^{-7} cm/sec
	(b) 2×10^{-7} cm/sec
	(c) 5×10^{-7} cm/sec

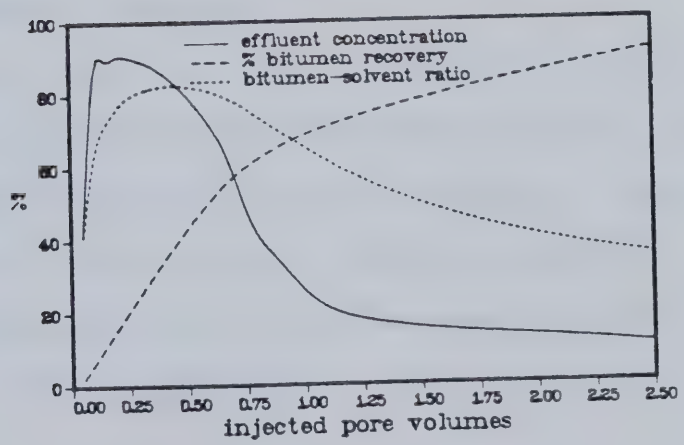
Table 5.2-1: Leaching Simulation Data Set



(a) $N_{Da} = 1$



(b) $N_{Da} = 2$



(c) $N_{Da} = 5$

Figure 5.2-1 : Leaching - Damköhler Effects on Production

bitumen observed with increased Damköhler number. Simultaneously, solid depletion is accelerated and the miscible drive advanced. This is apparent in the steeper slopes of the bitumen decline. Higher cumulative bitumen to solvent ratios with larger recoveries suggest increased leaching efficiency. Economic efficiency also depends on the bitumen to solvent slope, such that a termination time may be predicted when production no longer supports leaching economics.

A (6×6) diagonal grid was sufficiently large to damp any gross oscillation generated from numerical instability. Initial adsorption was significantly large such that TCP weights could not be obtained, and the second-order correct central difference scheme had to be adopted. The concentration surface was sufficiently smooth and diffusion sufficiently large to dissipate any convective oscillations. An initial indentation of the concentration front, similar to mild grid orientation, developed about the inlet but gradually disappeared as the miscible drive progressively dominated.

The grid size was chosen small in order to reduce the enormous time of evaluating the series-solution of the Stephan problem, and the subsequent calculation of pointwise convolution integrals. Convergence by successive substitution was slow while dissolution prevailed. Problems were encountered about the zero radius where dissolution about singular points were forced to completion.

CHAPTER SIX

CONCLUSION

An overall discussion summarizes both theoretical model and the numerical simulator. Limitations are established, and leaching viability addressed.

Achieved objectives are recognized with further proposals directed towards future research.

6.1. Discussion

The nonequilibrium leaching model predicts instantaneous porosity and saturation-dependent adsorption, in comparison to previous investigations for solution mining, limited to small porosity change with first-order reaction. An integro-differential absorption term keeps track of the solvent accumulated in the solid over the total time elapsed. Together with first-order adsorption, the instantaneous saturation follows from material balance. The solid phase spatial concentration distribution is implicit in the analytical solution of the nonstationary Stephan problem, and only the critical surface concentration at the spherical solid-liquid interface is needed a priori.

Symmetry is essential for predicting similar dissolution fronts. Non-spherical particles experiencing radial dissolution will require a separate relationship for the dynamic geometry of the dissolving particle surface. Boundary layer effects may distort radial dissolution with accelerated upstream erosion at the leading particle edge.

The model confines each particle to its respective pore for all times of its dissolution history. However, fluid inertia may carry the particle intact, to some new location downstream.

Local uniformity of the particle, in conjunction with a number density, relates the microscopic dissolution of individual particles to the bulk solvent transfer. For a large variance in regional particle size, a statistical extension to the integro-differential process must provide the macroscopic transfer rate.

First-order adsorption assumes a linear concentration drop across the solid-liquid interface, with the ambient fluid concentration approximated by the local macroscopic average. The model assumes a constant adsorption coefficient, and rapid interstitial mixing to equalize local concentrations. In the absence of absorption, linear first-order adsorption predicts asymptotic saturation histories. When combined with absorption, dissolution predicts finite particle-life times with a marked discontinuity at the zero radius. The critical surface concentration determines the particle capacity for solvent absorption, and extremely sensitive systems may result in highly accelerated dissolution from an avalanching phase change, terminating the particle.

The linearity of adsorption creates problems in the presence of nonlinear absorption, with a singular equation about the zero radius. The linear model inherently assumes the ambient fluid concentration to be greater than the critical solid concentration for adsorption to proceed in the positive sense. Furthermore, accumulation within the transition zone is neglected. A more rigorous approach might model the individual pore-particle system, accounting for the microscopic variations in fluid

solvent to predict nonlinear adsorption. Fluid solvent would accumulate in a laminar boundary layer to yield a sharp spike in the normal concentration profile at the solid liquid contact surface. The non-reversible phase change would liberate heat locally about the dissolution site to be subsequently dissipated by the streaming ambient solution.

An initial liquid continuity is essential for the model to function properly. The initial conditions investigated establish solvent to uniformly saturate the medium throughout. Such uniform sweeps do not accurately represent breakthrough conditions, and without better knowledge of the fingering mechanisms involved, the fully invaded medium becomes a basic mathematical device for initialization.

The system responds to the uniformity of the initial conditions by adjusting to a stabilized state, where dissolution equalizes displacement at every point in the flow field. The stabilized concentration and saturation surfaces reflect a natural equilibrium state, characteristic of the flow geometry. As dissolution drives saturations higher, the increase in liquid pore space allows displacement to progressively dominate. Competition for solvent between absorption and displacement trigger rippling oscillations throughout the concentration surface. Bursts of bitumen appear in the effluent as the ripples migrate downstream.

The extent of rippling depends not only on the physical system, but also on the choice of initial conditions. If one could initiate leaching from the moment of solvent injection, fingering displacement mechanisms would determine the course of diffusing species, and the non-uniformity of the etched fluid paths would enhance pulsating of the

effluent bitumen.

The leaching model has a closed form solution approximated with finite differences. The leaching simulator developed uses a five-point scheme for simplicity of implementation. Numerical limitations at high viscosity ratios become apparent when convection dominates. The partial differential equations become locally hyperbolic, where the finite-difference solution is unable to uniquely track the self-sharpening front. Mobility and diffusivity nonlinearities are approximated downstream (and back in time) to yield realistic miscible displacement on a diagonal grid. The shape of the predicted concentration surfaces are well represented, with channel formation at the extreme viscosity ratios associated with tar sand.

Miscible similarity is controlled by the Peclet number, depending on the injection rate, grid partition, grain size and viscosity ratio in two dimensional displacements. The Damköhler number governs dissolution kinetics with the critical concentration as the absorptive capacity. Time scaling dissolution with displacement is crucial for the resolution of saturation histories. Dissolution is scaled by a characteristic dimensionless time dependent on both molecular diffusion rate in the solid and initial particle radius. A dimensionless time ratio relates the dissolution time scale to the pore volumes of injected fluid to estimate the simulation time necessary to resolve particle lifetimes.

Simulation predicts increasing leaching efficiency for solvents with higher adsorption coefficients. Hot solvent injection is a viable procedure to increase adsorptivity, and enhance dissolution. However, a thermal model must be developed including a heat diffusivity equation

to determine temperature distributions. Hot solvents may invade tar sands more evenly, dissipating heat to effectively increase downstream mobilities.

6.2. Further Study

The thesis has presented an isothermal model for the in situ solvent leaching of tar sand. A two-dimensional, two-phase, two-component compositional simulator was developed to approximate the differential system. Analysis of simulated results identified parametric scaling effects providing insight for large-scale operations.

Future work may investigate the thermal-compositional effects in a three-dimensional, multicomponent system with multi-fluid phases. A nonlinear adsorption model may be developed. High-accuracy numerical techniques may be implemented.

REFERENCES

1. Danby, A.: Natural Rock Asphalts and Bitumens, London, Constable and Company Limited, (1913).

2. Hekim, Y. and Fogler, H.S.: "On the Movement of Multiple Reaction Zones in Porous Media," A.I.Ch.E.J. (May 1980) 403-444.

3. Hekim, Y., Fogler, H.S., McCune, C.C.: "The Radial Movement of Permeability Fronts and Multiple Reaction Zones in Porous Media," (Tech. Paper SPE9495), Soc. Pet. Eng. J. (Feb. 1982) 99-107.

4. Schechter, R.S. and Gidley, J.L.: "Change in Pore Size Distribution from Surface Reaction in Porous Media," A.I.Ch.E.J. (May 1969) 339-350.

5. Glover, M.C. and Guin, J.A.: "Dissolution of a Homogeneous Porous Medium by Surface Reaction," A.I.Ch.E.J. (Nov. 1973) 1190-1195.

6. Crank, J: The Mathematics of Diffusion, Oxford Clarendon Press (1956).

7. Carslaw, H.S. and Jaeggar, J.C.: Conduction of Heat in Solids, Oxford Clarendon Press (1959).

8. Readey, D.W. and Cooper, A.R., Jr.: "Molecular Diffusion with a Moving Boundary and Spherical Symmetry," Chem. Eng. Sci. 21[10], 917-922 (1966).

9. Crank, J. and Park, G.S.: Diffusion in Polymers, Academic Press, London (1968).

10. Rosner, D.E. and Epstein, M.: "Effects of Interface Kinetics, Capillarity, and Solute Diffusion on Bubble Growth Rates in Highly Saturated Liquids," Chem. Eng. Sci. 27, 69-88 (1972).

11. Perrine, R.L.: "The Development of Stability Theory for Miscible Liquid-Liquid Displacement," Soc. Pet. Eng. J. (March 1961) 17.

12. Peaceman, D.W. and Rachford, H.H.,Jr.: "Numerical Calculation of Multidimensional Miscible Displacement," Soc. Pet. Eng. J. (Dec. 1962) 327-339.

13. Chaudhari, N.M.: "An Improved Numerical Technique for Solving Multidimensional Miscible Displacement," Soc. Pet. Eng. J. (Sept. 1971) 277-284.

14. Chaudhari, N.M.: "A Numerical Solution with Second-Order Accuracy for Multicomponent Compressible Stable Miscible Flow," Soc. Pet. Eng. J. (April 1973) 81-91.

15. Todd, M.R., O'Dell, P.M. and Hirasaki, G.J.: "Methods for Increased Accuracy in Numerical Simulation," Soc. Pet. Eng. J. (1972) 515-530.

16. Price, H.S., Varga, R.S. and Warren, J.E.: "Application of Oscillation Matrices to Diffusion Convection Equations," J. of Math. and Phys. (Sept. 1966) Vol. 45, 301-311.

17. Laumbach, D.D.: "A High-Accuracy Finite-Difference Technique for Treating the Convection-Diffusion Equation," Soc. Pet. Eng. J. (Dec. 1975) 517-531.

18. Peaceman, D.W. and Rachford, H.H., Jr.: "Numerical Calculation of Parabolic and Elliptic Differential Equations," J. Soc. Ind. App. Math. (1955) Vol. 3, 28-41.

19. Larson, R.G.: "Controlling Numerical Dispersion by Variably Times Flux Updating in One Dimension," Soc. Pet. Eng. J. (June 1982) 399-408.

20. Larson, R.G.: "Controlling Numerical Dispersion by Variably Timed Flux Updating in Two Dimensions," Soc. Pet. Eng. J. (June 1982) 409-419.

21. Settari, A., Price, H.S., Dupont, T.: "Development and Application of Variational Methods for Simulation of Miscible Displacement in Porous Media," Soc. Pet. Eng. J. (June 1977) 228-246.

22. Young, L.C.: "A Finite-Element Method for Reservoir Simulation," Soc. Pet. Eng. J. (Feb. 1981) 115-128.

23. Price, H.S., Cavendish, T.C. and Varga, R.S.: "Numerical Methods of Higher Order Accuracy for the Diffusion-Convection Equation," Soc. Pet. Eng. J., Vol. 8 (1968) 293-303.

24. Cavendish, T.C., Price, H.S. and Varga, R.S.: "Galerkin Methods for the Numerical Solution of Boundary Value Problems," Soc. Pet. Eng. J. (June 1969) 204-220.

25. Garder, A.D., Jr., Peaceman, D.W., Pozzi, A.I., Jr.: "Numerical Calculation of Multidimensional Miscible Displacement by the Method of Characteristics," Soc. Pet. Eng. J. (March 1964) 26-36.

26. Ewing, R.E., Russel, T.F., Wheeler, M.F.: "Simulation of Miscible Displacement using Mixed Methods and a Modified Method of Characteristics," (SPE 12241) Proceeding of the Seventh SPE Symposium on Reservoir Simulation, San Francisco, California (Nov. 1983).

27. Li, K.M.G.: "Random Choice Method for Creating the Convection-Diffusion Equation," (SPE 12237) Proceeding of the Seventh SPE Symposium on Reservoir Simulation, San Francisco, California (Nov. 1983).

28. Glimm, J.: "Solution in the Large for Nonlinear Hyperbolic System of Equations," Comm. Pure Appl. Math. (1965) 18, 399-408.

29. Chorin, A.J.: "Random Choice Solution of Hyperbolic Systems," J. Comp. Physics (Dec. 1976) 22, 253-272.

30. Ciment, M., Leventhal, S.H., Weinberg, B.C.: "The Operator Compact Implicit Method for Parabolic Equations," J. Comp. Phys. 28 (1978) 135-166.

31. Leventhal, S.H.: "The Operator Compact Implicit Method for Reservoir Simulation," Soc. Pet. Eng. J. (June 1980) 120-128.

32. Manohar, R.P. and Masliyah, J.H.: "Application of a High Order Single Cell Differencing Scheme to Diffusion-Convection Equations," Submitted to Comp. Mech. in Appl. Mech. and Eng.

33. Gupta, M.M., Manohar, R.P., Stephenson, J.W.: "A High Order Finite Difference Method for Fluid Flow Problems," Proceeding of the Tenth IMACS World Congress on System Simulation and Scientific Computation, Montreal, Canada (Aug. 1982) Vol. 1, 212-214.

34. Yanosik, J.L. and McCracken, T.A.: "A Nine Point Finite Difference Reservoir Simulator for Realistic Prediction of Unfavorable Mobility Ratio Displacement," Soc. Pet. Eng. J. (Aug. 1979) 253-262.

35. Robertson, G.E. and Woo, P.T.: "Grid-Orientation Effects and the Use of Orthogonal Curvilinear Coordinates in Reservoir Simulation," Soc. Pet. Eng. J. (Feb. 1978) 13-19.

36. Vinsome, P.K. and Au, A.D.K.: "One Approach to the Grid Orientation Problem in Reservoir Simulation," SPE 8247 Presented at 54th Annual Fall Technical Conference SPE of AIME, Las Vegas, Nevada, Sept 23-26, 1979.

37. Perkins, J.K. and Johnston, O.C.: "A Review of Diffusion and Dispersion in Porous Media," Soc. Pet. Eng. J. (March 1963) 70-84.

38. Scheideggar, A.E.: "General Theory of Dispersion in Porous Media," Jour. Geophys. Research (Oct. 1961) 3273.

39. Peaceman, D.W.: "Improved Treatment of Dispersion in Numerical Calculation of Multidimensional Miscible Displacement," Soc. Pet. Eng. J. (Sept. 1966) 213-216.

40. Hubbert, M.K.: "Darcy's Law and the Field Equations of the Flow of Underground Fluids," Trans. AIME (1956) V. 207, 222-239.

41. Scheideggar, A.E.: The Physics of Flow Through Porous Media, The MacMillan Co., New York City (1957).

42. Petroleum Congress, London (1933).

43. Price, H.S. and Coats, K.H.: "Direct Methods in Reservoir Simulation," Soc. Pet. Eng. J. (June 1974) 14, 295-308.

44. Habermann, B.: "The Efficiency of Miscible Displacement as a Function of Mobility Ratio," Petroleum Transactions, AIME, Vol. 219 (Nov. 1960) 264-272.

45. Hildebrand, F.B.: Advanced Calculus for Applications, Prentice-Hall Inc., New Jersey (1976), Prob. 11.7, p. 672.

46. Crank, J.: The Mathematics of Diffusion, Oxford Clarendon Press (1956), Table 2.2, Item 19.

47. Oberhettinger, F. and Badii, L.: Tables of Laplace Transforms, Springer-Verlag, New York, Heidelberg, Berlin (1973), Sec. 2.5, Item 5.102.

APPENDIX A

THE ANALYTICAL SOLUTION TO THE RADIAL SPHERICAL DIFFUSION EQUATION WITH A TIME DEPENDENT BOUNDARY

The method of Laplace transform is used to obtain the analytical solution to:

$$\frac{D_s}{r^2}\frac{\partial}{\partial r}\left(r^2\frac{\partial C_s}{\partial r}\right) = \frac{\partial C_s}{\partial t}; \qquad 0 \leq r \leq r_p(t) \qquad A(1)$$

satisfying the initial and boundary conditions,

$$r_p(t=0) = r_0 \qquad A(2)$$

$$C_s(r,t=0) = 0 \qquad A(3)$$

$$C_s(r_p,t>0) = C^* \qquad A(4)$$

$$\left.\frac{\partial C_s}{\partial r}\right|_{r=0} = 0 \qquad A(5)$$

The transformed equation,

$$D_s\frac{\partial^2 C}{\partial r^2} = \frac{\partial C}{\partial t}; \qquad 0 \leq r \leq r_p(t) \qquad A(6)$$

with the conditions,

$$C(r,t=0) = 0 \qquad A(7)$$

$$C(\quad,t>0) = C^* \qquad A(8)$$

$$C(\quad,\quad) = 0 \qquad A(9)$$

follow from the change of variable:

$$C = rC_s \qquad A(10)$$

$$C^* = r_p C^* \qquad A(11)$$

Applying the Laplace transform,

$$\mathcal{L}\{C(r,t)\} = \int_0^\infty Ce^{-st}dt = \bar{C}(r,s) \qquad A(12)$$

to equation A(6),

$$D_s \int_0^\infty \frac{\partial^2 C}{\partial r^2} e^{-st}dt - \int_0^\infty \frac{\partial C}{\partial t} e^{-st}dt = 0 \qquad A(13)$$

interchanging the order of integration and differention in the first term,

$$D_s \frac{\partial^2}{\partial r^2} \int_0^\infty Ce^{-st}dt - \int_0^\infty \frac{\partial C}{\partial t} e^{-st}dt = 0 \qquad A(14)$$

and integrating the last term by parts, yields:

$$D_s \frac{\partial^2 \bar{C}}{\partial r^2} - Ce^{-st}\Big|_0^\infty - s\bar{C} = 0 \qquad A(15)$$

By virtue of the initial condition A(7), the middle term vanishes and the Laplace transformed equation becomes the ordinary differential equation,

$$D_s \frac{\partial^2 \bar{C}}{\partial r^2} - s\bar{C} = 0 \qquad A(16)$$

with the boundary conditions:

$$\bar{C}(0) = 0 \qquad A(17)$$

$$\bar{C}(r_p) = \int_0^\infty C^* e^{-st} dt = \bar{C}^* \qquad A(18)$$

The characteristic equation of the O.D.E. A(16),

$$D_s q^2 - s = 0 \qquad A(19)$$

whose roots,

$$|q| = \sqrt{\frac{s}{D_s}} \qquad A(20)$$

determine the general solution,

$$\bar{C} = ae^{-qr} + be^{qr} \qquad A(21)$$

where a and b are constants to be determined by the boundary conditions A(17) and A(18).

Applying these boundary conditions to A(21) gives:

$$\bar{C}(0) = a + b = 0 \qquad A(22)$$

$$\bar{C}(r_p) = ae^{-qr_p} + be^{qr_p} = \bar{C}^* \qquad A(23)$$

Solving for a and b simultaneously yields:

$$a = \frac{\bar{C}^*}{2 \sinh (qr_p)} \qquad A(24)$$

$$b = \frac{-\bar{C}^*}{2 \sinh (qr_p)} \qquad A(25)$$

The particular solution to equation A(21) satisfying the boundary conditions A(17) and A(18) is:

$$\bar{C} = \bar{C}^* \frac{\sinh(qr)}{\sinh(qr_p)} \qquad A(26)$$

The solution to A(6) satisfying the initial and boundary conditions A(7), A(8) and A(9) is the inverse Laplace transform of A(26).

$$C(r,t) = \mathcal{L}^{-1}\{\bar{C}(r,s)\} \qquad A(27)$$

Define $\bar{A}$,

$$\bar{A}(r,s) = \frac{1}{s}\left\{\frac{\sinh(qr)}{\sinh(qr_p)}\right\} \qquad A(28)$$

such that,

$$\bar{C}(r,s) = s\bar{C}^*\bar{A} \qquad A(29)$$

Using the relationship,

$$s\bar{C}^* = \mathcal{L}\left\{\frac{\partial C^*}{\partial t}\right\} + C^*(0) \qquad A(30)$$

gives:

$$\begin{aligned} C(r,t) &= \mathcal{L}^{-1}\{s\bar{C}^*\bar{A}\} \\ &= C^*(0)\mathcal{L}^{-1}\{\bar{A}\} + \mathcal{L}^{-1}\left\{\mathcal{L}\left\{\frac{\partial C^*}{\partial t}\right\}\bar{A}\right\} \end{aligned} \qquad A(31)$$

Define A,

$$A(r,t) = \mathcal{L}^{-1}\{\bar{A}(r,s)\} = \mathcal{L}^{-1}\left\{\frac{1}{s}\left[\frac{\sinh(qr)}{\sinh(qr_p)}\right]\right\} \qquad A(32)$$

From Hildebrand[45],

$$A(r,t) = \frac{r}{r_p}\left\{1 + \frac{2r_p}{\pi r}\sum_{k=1}^{\infty}\frac{(-1)^k}{k}\, e^{-k^2\pi^2 D_s t/r_p^2}\sin\left(\frac{k\pi r}{r_p}\right)\right\} \qquad A(33)$$

The convolution is related to the integral,

$$\mathcal{L}^{-1}\left\{\mathcal{L}\left\{\frac{\partial C^*}{\partial t}\right\}\bar{A}\right\} = \int_0^t \frac{\partial C^*}{\partial t}\Big|_\tau A(r,t-\tau)\,d\tau \qquad A(34)$$

and from A(31):

$$C(r,t) = C^*(0)A(r,t) + \int_0^t \frac{\partial C^*}{\partial t}\Big|_\tau A(r,t-\tau)\,d\tau \qquad A(35)$$

Using the change of variable A(10) and A(11) gives the analytical solution to the radial diffusion equation A(1) satisfying the initial and boundary conditions A(2), A(3), A(4) and A(5).

$$C(r,t) = C^*\left\{r_o f(r,t) + \int_0^t \dot{r}_p(\tau) f(r,t-\tau)\,d\tau\right\}$$

$$f(r,t) = \left\{\frac{1}{r_p} + \frac{2}{\pi r}\sum_{k=1}^{\infty}\frac{(-1)^k}{k}\, e^{-k^2\pi^2 D_s t/r_p^2}\sin\left(\frac{k\pi r}{r_p}\right)\right\} \qquad A(36)$$

APPENDIX B

DIRECTIONAL TRUNCATION CANCELLATION PROCEDURE FOR CONVECTION DOMINANT DISPLACEMENTS

The truncation cancellation procedure, TCP, described herein was developed by the author for direct solution, paralleling the scheme developed by Laumbach[17] for the alternating direction implicit procedure[18] (ADIP). Unlike the ADIP version, the direct TCP involves a transformation of the truncation error into velocity coordinates, where optimal weights suppress a dominant longitudinal error term. The analysis assumes convective dominance, where both adsorption and diffusion are relatively small. This approach deals with the differential form of the convective-diffusion equation and an extension to the integral form follows directly.

The differential form of the convective-diffusion with adsorption (CDA) equation can be written in the form:

$$\nabla \cdot (\tilde{D} \cdot \nabla C) - \nabla \cdot (\vec{u} C) = \phi \frac{\partial C}{\partial t} + 4\pi N_p r_p^2 [\alpha (C - C^*)] \qquad B(1)$$

The CDA equation is discretized about mesh point, P_{ij}, at the mid-time level, $t^{n+\frac{1}{2}}$, using central differences. Let Δ denote the central-difference operator, with (Δ_x, Δ_y) as the component spatial differences and Δ_t as the temporal difference. Let $(\bar{\ })$ denote the arithmetic time average relating the midtime values to the upper and lower time nodes.

The diffusion term is discretized to second-order accuracy in both space and time,

$$\nabla \cdot (\tilde{D} \cdot \nabla C)\Big|_{ij}^{n+\frac{1}{2}} = \Delta_x (D_{xx}\Delta_x \bar{C} + D_{xy}\Delta_y \bar{C})_{ij}^{n+\frac{1}{2}} + \Delta_y (D_{yx}\Delta_x \bar{C} + D_{yy}\Delta_y \bar{C})_{ij}^{n+\frac{1}{2}} + O(h^2) \qquad B(2)$$

with the order of accuracy estimate, h.

$$h = \max(\Delta x, \Delta y, \Delta t) \qquad B(3)$$

The adsorption term is time averaged to second-order accuracy.

The component convective terms are discretized to second-order accuracy in both space and time,

$$\frac{\partial}{\partial x}(u_x C)\Big|_{ij}^{n+\frac{1}{2}} = \frac{1}{4\Delta x}\left\{ u_{x_{i+\frac{1}{2},j}}^{n+\frac{1}{2}} \left[C_{i+1,j}^{n+1} + C_{ij}^{n+1} + C_{i+1,j}^{n} + C_{ij}^{n} \right] - u_{x_{i-\frac{1}{2},j}}^{n+\frac{1}{2}} \left[C_{ij}^{n+1} + C_{i-1,j}^{n+1} + C_{ij}^{n} + C_{i-1,j}^{n} \right] \right\} + E_x$$

$$\frac{\partial}{\partial y}(u_y C)\Big|_{ij}^{n+\frac{1}{2}} = \frac{1}{4\Delta y}\left\{ u_{y_{i,j+\frac{1}{2}}}^{n+\frac{1}{2}} \left[C_{i,j+1}^{n+1} + C_{ij}^{n+1} + C_{i,j+1}^{n} + C_{ij}^{n} \right] - u_{y_{i,j-\frac{1}{2}}}^{n+\frac{1}{2}} \left[C_{ij}^{n+1} + C_{i,j-1}^{n+1} + C_{ij}^{n} + C_{i,j-1}^{n} \right] \right\} + E_y \qquad B(4)$$

with the corresponding second-order correct truncation errors expressed to fourth-order.

$$E_x = -\frac{\Delta t^2}{24}\left\{\left(\frac{\Delta x}{\Delta t}\right)^2 \frac{\partial^3}{\partial x^3}(u_x C) + 3\left(\frac{\Delta x}{\Delta t}\right)^2 \frac{\partial}{\partial x}\left(u_x \frac{\partial^2 C}{\partial x^2}\right) + 3\frac{\partial}{\partial x}\left(u_x \frac{\partial^2 C}{\partial t^2}\right)\right\}\Bigg|_{i,j}^{n+\frac{1}{2}}$$

$$+ O(h^4)$$

$$E_y = -\frac{\Delta t^2}{24}\left\{\left(\frac{\Delta y}{\Delta t}\right)^2 \frac{\partial^3}{\partial y^3}(u_y C) + 3\left(\frac{\Delta y}{\Delta t}\right)^2 \frac{\partial}{\partial y}\left(u_y \frac{\partial^2 C}{\partial y^2}\right) + 3\frac{\partial}{\partial y}\left(u_y \frac{\partial^2 C}{\partial t^2}\right)\right\}\Bigg|_{i,j}^{n+\frac{1}{2}}$$

$$+ O(h^4) \qquad B(5)$$

The accumulation term is spatially weighted over the five-point difference star,

$$\left(\phi \frac{\partial C}{\partial t}\right)_{ij}^{n+\frac{1}{2}} = (1-\omega_1-\omega_2)\left[\phi \Delta_t C\right]_{ij}^{n+\frac{1}{2}}$$

$$+ \frac{\omega_1}{2}\left[(\phi \Delta_t C)_{i+1,j} + (\phi \Delta_t C)_{i-1,j}\right]^{n+\frac{1}{2}}$$

$$+ \frac{\omega_2}{2}\left[(\phi \Delta_t C)_{i,j+1} + (\phi \Delta_t C)_{i,j-1}\right]^{n+\frac{1}{2}} + E_t \qquad B(6)$$

with E_t as the weighted truncation error of discretization also expressed to fourth-order.

$$E_t = -\frac{\Delta t^2}{24}\left\{\phi \frac{\partial^3 C}{\partial t^3} + 12\omega_1\left(\frac{\Delta x}{\Delta t}\right)^2 \frac{\partial^2}{\partial x^2}\left(\phi \frac{\partial C}{\partial t}\right) + 12\omega_2\left(\frac{\Delta y}{\Delta t}\right)^2 \frac{\partial^2}{\partial y^2}\left(\phi \frac{\partial C}{\partial t}\right)\right\}_{i,j}^{n+\frac{1}{2}}$$

$$+ O(h^4) \qquad B(7)$$

The discretized CDA equation has the form,

$$\left\{\Delta_x[D_{xx}\Delta_x\bar{C} + D_{xy}\Delta_y\bar{C} - u_x\bar{C}] + \Delta_y[D_{yx}\Delta_x\bar{C} + D_{yy}\Delta_y\bar{C} - u_y\bar{C}]\right\}_{ij}^{n+\frac{1}{2}}$$

$$- \left\{(1-\omega_1-\omega_2)[\phi\Delta_t C]_{ij} + \frac{\omega_1}{2}[(\phi\Delta_t C)_{i+1,j} + (\phi\Delta_t C)_{i-1,j}]\right.$$

$$\left. + \frac{\omega_2}{2}[(\phi\Delta_t C)_{i,j+1} + (\phi\Delta_t C)_{i,j-1}]\right\}^{n+\frac{1}{2}}$$

$$- \left\{4\pi N_p \bar{r}_p^2[\alpha_s(\bar{C}-C^*)]\right\}_{ij}^{n+\frac{1}{2}} = E \qquad \text{B(8)}$$

where E is the net discretization error,

$$E = E_a - E_d - \frac{\Delta t^2}{24}\left\{\left[\phi\frac{\partial^3 C}{\partial t^3} + 12\frac{\omega_1}{r_1^2}\frac{\partial^2}{\partial x^2}\left(\phi\frac{\partial C}{\partial t}\right) + 12\frac{\omega_2}{r_2^2}\frac{\partial^2}{\partial y^2}\left(\phi\frac{\partial C}{\partial t}\right)\right]\right.$$

$$+ \left[\frac{1}{r_1^2}\frac{\partial^3}{\partial x^3}(u_x C) + \frac{3}{r_1^2}\frac{\partial}{\partial x}\left(u_x\frac{\partial^2 C}{\partial x^2}\right) + 3\frac{\partial}{\partial x}\left(u_x\frac{\partial^2 C}{\partial t^2}\right)\right]$$

$$\left. + \left[\frac{1}{r_2^2}\frac{\partial^3}{\partial y^3}(u_y C) + \frac{3}{r_2^2}\frac{\partial}{\partial y}\left(u_y\frac{\partial^2 C}{\partial y^2}\right) + 3\frac{\partial}{\partial y}\left(u_y\frac{\partial^2 C}{\partial t^2}\right)\right]\right\}_{ij}^{n+\frac{1}{2}}$$

$$+ O(h^4) \qquad \text{B(9)}$$

E_d and E_a are the second-order errors of diffusion and adsorption, respectively, and the parameters r_1 and r_2 are the ratios of time step to component cell-dimensions.

$$r_1 = \frac{\Delta t}{\Delta x}$$

$$r_2 = \frac{\Delta t}{\Delta y} \qquad \text{B(10)}$$

As the rate of dissolution drops, the solid phase becomes virtually inert and miscible transport dominates. At high flow rates,

diffusion becomes small and convection dominates. In the limiting case, the CDA equation reduces to convection equation,

$$\phi \frac{\partial C}{\partial t} + \frac{\partial}{\partial x}(u_x C) + \frac{\partial}{\partial y}(u_y C) = 0 \qquad \text{B(11)}$$

and the porosity becomes constant in time. With these assumptions, the third-order partials can be calculated directly from B(11).

$$\phi \frac{\partial^3 C}{\partial t^3} = -\left[\frac{\partial^3}{\partial t^2 \partial x}(u_x C) + \frac{\partial^3}{\partial t^2 \partial y}(u_y C)\right]$$

$$\frac{\partial^2}{\partial x^2}\left(\phi \frac{\partial C}{\partial t}\right) = -\left[\frac{\partial^3}{\partial x^3}(u_x C) + \frac{\partial^3}{\partial x^2 \partial y}(u_y C)\right] \qquad \text{B(12)}$$

$$\frac{\partial^2}{\partial y^2}\left(\phi \frac{\partial C}{\partial t}\right) = -\left[\frac{\partial^3}{\partial x \partial y^2}(u_x C) + \frac{\partial^3}{\partial y^3}(u_y C)\right]$$

Upon substitution of these third-order partials into B(9), the net discretization error becomes:

$$E = E_a - E_d - \frac{\Delta t^2}{24}\left\{\left[\frac{(1-12\omega_1)}{r_1^2}\frac{\partial^3(u_x C)}{\partial x^3} - 12\frac{\omega_1}{r_1^2}\frac{\partial^3(u_y C)}{\partial x^2 \partial y}\right.\right.$$

$$\left. + \frac{3}{r_1^2}\frac{\partial}{\partial x}\left(u_x \frac{\partial^2 C}{\partial x^2}\right) - \frac{\partial^3(u_x C)}{\partial x \partial t^2} + 3\frac{\partial}{\partial x}\left(u_x \frac{\partial^2 C}{\partial t^2}\right)\right]$$

$$+ \left[\frac{(1-12\omega_2)}{r_2^2}\frac{\partial^3(u_y C)}{\partial y^3} - \frac{12\omega_2}{r_2^2}\frac{\partial^3(u_x C)}{\partial y^2 \partial x} + \frac{3}{r_2^2}\frac{\partial}{\partial y}\left(u_y \frac{\partial^2 C}{\partial y^2}\right)\right.$$

$$\left.\left. - \frac{\partial^3(u_y C)}{\partial y \partial t^2} + 3\frac{\partial}{\partial y}\left(u_y \frac{\partial^2 C}{\partial t^2}\right)\right]\right\}_{ij}^{n+\frac{1}{2}} + O(h^4) \qquad \text{B(13)}$$

The weights ω_1 and ω_2 are local to the immediate neighbourhood of the volume element about mesh point P_{ij} and are spatial averages with time dependence only. The differential operators are regrouped,

$$E = E_a - E_d - \frac{\Delta t^2}{24}\left\{\frac{\partial}{\partial x}\left[\frac{(1-12\omega_1)}{r_1^2}\frac{\partial^2(u_xC)}{\partial x^2} - 12\frac{\omega_1}{r_1^2}\frac{\partial^2(u_yC)}{\partial x\partial y} + \frac{3u_x}{r_1^2}\frac{\partial^2 C}{\partial x^2} - \frac{\partial^2(u_xC)}{\partial t^2} + 3u_x\frac{\partial^2 C}{\partial t^2}\right]\right.$$

$$+\frac{\partial}{\partial y}\left[\frac{(1-12\omega_2)}{r_2^2}\frac{\partial^2(u_yC)}{\partial y^2} - \frac{12\omega_2}{r_2^2}\frac{\partial^2(u_xC)}{\partial y\partial x} + \frac{3u_y}{r_2^2}\frac{\partial^2 C}{\partial y^2} - \frac{\partial^2(u_yC)}{\partial t^2}\right.$$

$$\left.\left.+ 3u_y\frac{\partial^2 C}{\partial t^2}\right]\right\}_{ij}^{n+\frac{1}{2}} + O(h^4) \qquad \text{B(14)}$$

to give the equivalent vector expression:

$$E = E_a - E_d - \frac{\Delta t^2}{24}(\nabla\cdot\vec{\varepsilon}) + O(h^4) \qquad \text{B(15)}$$

The error flux, $\vec{\varepsilon}$, is a second-order differential equation and can be expressed using tensor notation by,

$$\vec{\varepsilon} = \left\{\left[\hat{e}_i\frac{\partial}{\partial x_i}\omega_{ij}\frac{\partial}{\partial x_j}\hat{e}_j\right]\cdot(C\vec{u}) - \frac{\partial^2}{\partial t^2}(C\vec{u})\right\}$$

$$+ 3\left\{\left[\left(\hat{e}_i\frac{\partial}{\partial x_i}\frac{1}{r_1^2}\frac{\partial}{\partial x_i}\hat{e}_i\right)C\right]\cdot\vec{u} + \left(\frac{\partial^2 C}{\partial t^2}\right)\vec{u}\right\} \qquad \text{B(16)}$$

where the cartesian weight matrix of the differential tensor operator is defined as:

$$\begin{bmatrix} \omega_{11} & \omega_{12} \\ \omega_{21} & \omega_{22} \end{bmatrix} = \begin{bmatrix} \frac{(1-12\omega_1)}{r_1^2} & \frac{-12\omega_1}{r_1^2} \\ \frac{-12\omega_2}{r_2^2} & \frac{(1-12\omega_2)}{r_2^2} \end{bmatrix} \qquad B(17)$$

Evaluation of the dot products in B(16) gives the cartesian error components.

$$\varepsilon_i = \omega_{ij} \frac{\partial^2}{\partial x_i \partial x_j} (u_j C) + 3 \frac{u_i}{r_i^2} \frac{\partial^2 C}{\partial x_i^2} - \frac{\partial^2}{\partial t^2} (C u_i) + 3 u_i \frac{\partial^2 C}{\partial t^2} \qquad B(18)$$

The error flux is dependent on both velocity magnitude and angle, such that a similarity transformation into velocity coordinates give rise to longitudinal and transverse components. In the velocity frame $F_u\{x_i'\}$, the velocity direction coincides with the principal longitudinal axis. The similarity transformation from cartesian to velocity frame involves a point rotation through a velocity angle, θ.

$$R = \begin{bmatrix} \cos\theta & -\sin\theta \\ \sin\theta & \cos\theta \end{bmatrix}$$

$$\theta = \tan^{-1}\left(\frac{u_y}{u_x}\right) \qquad B(19)$$

The basis vectors and partial differential operators transform accordingly,

$$\hat{e}_i = R_{ik} \hat{e}_k'$$

$$\frac{\partial}{\partial x_i} = R_{i\ell} \frac{\partial}{\partial x_\ell'} \qquad B(20)$$

to give the error flux in velocity coordinates.

$$\vec{\varepsilon} = \left\{ \left[R_{ik} \hat{e}'_k R_{i\ell} \frac{\partial}{\partial x'_\ell} \omega_{ij} R_{jm} \frac{\partial}{\partial x'_m} R_{jn} \hat{e}'_n \right] \cdot (Cu\hat{e}'_1) - \frac{\partial^2}{\partial t^2} (Cu)\hat{e}'_1 \right\}$$

$$+ 3\left\{ \left[\left(R_{ik} \hat{e}'_k R_{i\ell} \frac{\partial}{\partial x'_\ell} \frac{1}{r_i^2} R_{im} \frac{\partial}{\partial x'_m} R_{in} \hat{e}'_n \right) C \right] \cdot (u\hat{e}'_1) + \left(\frac{\partial^2 C}{\partial t^2} \right) u\hat{e}'_1 \right\} \qquad B(21)$$

Evaluation of the dot products,

$$\vec{\varepsilon} = \left\{ \left[R_{ik} \hat{e}'_k R_{i\ell} \frac{\partial}{\partial x'_\ell} \omega_{ij} R_{jm} \frac{\partial}{\partial x'_m} R_{j1} \right] (Cu) - \frac{\partial^2}{\partial t^2} (Cu)\hat{e}_1 \right\}$$

$$+ 3\left\{ \left[\left(R_{ik} \hat{e}'_k R_{i\ell} \frac{\partial}{\partial x'_\ell} \frac{1}{r_i^2} R_{im} \frac{\partial}{\partial x'_m} R_{i1} \right) C \right] u + \left(\frac{\partial^2 C}{\partial t^2} \right) u\hat{e}_1 \right\} \qquad B(22)$$

allows an isolation of the individual longitudinal and transverse error flux terms.

$$\varepsilon'_1 = \left\{ \left[R_{i1} R_{i\ell} \frac{\partial}{\partial x'_\ell} \omega_{ij} R_{jm} \frac{\partial}{\partial x'_m} R_{j1} \right] (Cu) - \frac{\partial^2}{\partial t^2} (Cu) \right\}$$

$$+ 3\left\{ \left[\left(R_{i1} R_{i\ell} \frac{\partial}{\partial x'_\ell} \frac{1}{r_i^2} R_{im} \frac{\partial}{\partial x'_m} R_{i1} \right) C \right] u + \left(\frac{\partial^2 C}{\partial t^2} \right) u \right\}$$

$$\varepsilon'_2 = \left\{ \left[R_{i2} R_{i\ell} \frac{\partial}{\partial x'_\ell} \omega_{ij} R_{jm} \frac{\partial}{\partial x'_m} R_{j1} \right] (Cu) \right.$$

$$\left. + 3 \left[\left(R_{i2} R_{i\ell} \frac{\partial}{\partial x'_\ell} \frac{1}{r_i^2} R_{im} \frac{\partial}{\partial x'_m} R_{i1} \right) C \right] u \right\} \qquad B(23)$$

Termwise expansion of the component fluxes gives second-order differential expressions in the velocity frame.

$$\varepsilon_1' = \left\{ \omega_{ij} R_{i1} R_{j1} \left[R_{i1} R_{j1} \frac{\partial^2 (Cu)}{\partial x_1'^2} + (R_{i2} R_{j1} + R_{i1} R_{j2}) \frac{\partial^2 (Cu)}{\partial x_1' \partial x_2'} + R_{i2} R_{j2} \frac{\partial^2 (Cu)}{\partial x_2'^2} \right] \right.$$

$$\left. + \frac{3u}{r_i^2} R_{i1}^2 \left[R_{i1}^2 \frac{\partial^2 C}{\partial x_1'^2} + 2 R_{i1} R_{i2} \frac{\partial^2 C}{\partial x_1' \partial x_2'} + R_{i2}^2 \frac{\partial^2 C}{\partial x_2'^2} \right] - \frac{\partial^2 (Cu)}{\partial t^2} + 3u \frac{\partial^2 C}{\partial t^2} \right\}$$

$$\varepsilon_2' = \left\{ \omega_{ij} R_{i2} R_{j1} \left[R_{i1} R_{j1} \frac{\partial^2 (Cu)}{\partial x_1'^2} + (R_{i2} R_{j1} + R_{i1} R_{j2}) \frac{\partial^2 (Cu)}{\partial x_1' \partial x_2'} + R_{i2} R_{j2} \frac{\partial^2 (Cu)}{\partial x_2'^2} \right] \right.$$

$$\left. + \frac{3u}{r_i^2} R_{i1} R_{i2} \left[R_{i1}^2 \frac{\partial^2 C}{\partial x_1'^2} + 2 R_{i1} R_{i2} \frac{\partial^2 C}{\partial x_1' \partial x_2'} + R_{i2}^2 \frac{\partial^2 C}{\partial x_2'^2} \right] \right\} \qquad \text{B(24)}$$

The quantized flow within the volume element is assumed incompressible and irrotational,

$$\nabla \cdot \vec{u} = 0 \Rightarrow \frac{\partial u}{\partial x_1'} = 0$$

$$\nabla \times \vec{u} = 0 \Rightarrow \frac{\partial u}{\partial x_2'} = 0 \qquad \text{B(25)}$$

such that the quantized velocity is constant about the immediate neighbourhood of the central mesh point. The quantized velocity is also assumed stationary about the mid-time node.

$$\frac{\partial u}{\partial t} = 0 \qquad \text{B(26)}$$

The partials are expanded, and then regrouped to yield:

$$\varepsilon_1' = u \left\{ R_{i1}^2 \left[\omega_{ij} R_{j1}^2 + \frac{3}{r_i^2} R_{i1}^2 \right] \frac{\partial^2 C}{\partial x_1'^2} \right.$$

$$+ R_{i1} \left[\omega_{ij} R_{j1} (R_{i2} R_{j1} + R_{i1} R_{j2}) + \frac{3}{r_i^2} R_{i1}^2 R_{i2} \right] \frac{\partial^2 C}{\partial x_1' \partial x_2'}$$

$$\left. + R_{i1} R_{i2} \left[\omega_{ij} R_{j1} R_{j2} + \frac{3}{r_i^2} R_{i1} R_{i2} \right] \frac{\partial^2 C}{\partial x_2'^2} + 2 \frac{\partial^2 C}{\partial t^2} \right\}$$

$$\varepsilon_2' = u \left\{ R_{i1} R_{i2} \left[\omega_{ij} R_{j1}^2 + \frac{3}{r_i^2} R_{i1}^2 \right] \frac{\partial^2 C}{\partial x_1'^2} \right.$$

$$+ R_{i2} \left[\omega_{ij} R_{j1} (R_{i2} R_{j1} + R_{i1} R_{j2}) + \frac{3}{r_1^2} R_{i1}^2 R_{i2} \right] \frac{\partial^2 C}{\partial x_1' \partial x_2'}$$

$$\left. + R_{i2}^2 \left[\omega_{ij} R_{j1} R_{j2} + \frac{3}{r_i^2} R_{i1} R_{i2} \right] \frac{\partial^2 C}{\partial x_2'^2} \right\} \qquad \text{B(27)}$$

The limiting convection equation in velocity coordinates,

$$\phi \frac{\partial C}{\partial t} = -u \frac{\partial C}{\partial x_1'} \qquad \text{B(28)}$$

is differentiated with respect to the longitudinal coordinate, and with respect to time, to relate the second-order time derivative to the second-order spatial derivative.

$$\frac{\partial^2 C}{\partial x_1' \partial t} = - \frac{u}{\phi} \frac{\partial^2 C}{\partial x_1'^2}$$

$$\frac{\partial^2 C}{\partial t^2} = - \frac{u}{\phi} \frac{\partial^2 C}{\partial t \partial x_1'} = \left(\frac{u}{\phi} \right)^2 \frac{\partial^2 C}{\partial x_1'^2} \qquad \text{B(29)}$$

Substitution into B(27) gives an expression for the quantized error flux, fully in terms of spatial partials.

$$\varepsilon_1' = u\left\{\left[R_{i1}^2\left(\omega_{ij}R_{j1}^2 + \frac{3}{r_i^2}R_{i1}^2\right) + 2\left(\frac{u}{\phi}\right)^2\right]\frac{\partial^2 C}{\partial x_1'^2}\right.$$

$$+ R_{i1}\left[\omega_{ij}R_{j1}(R_{i2}R_{j1}+R_{i1}R_{j2}) + \frac{3}{r_i^2}R^2{}_{i1}R_{i2}\right]\frac{\partial^2 C}{\partial x_1'\partial x_2'}$$

$$\left. + R_{i1}R_{i2}\left[\omega_{ij}R_{j1}R_{j2} + \frac{3}{r_i^2}R_{i1}R_{i2}\right]\frac{\partial^2 C}{\partial x_2'^2}\right\}$$

$$\varepsilon_2' = u\left\{R_{i1}R_{i2}\left[\omega_{ij}R_{j1}^2 + \frac{3}{r_i^2}R_{i1}^2\right]\frac{\partial^2 C}{\partial x_1'^2}\right.$$

$$+ R_{i2}\left[\omega_{ij}R_{j1}(R_{i2}R_{j1}+R_{i1}R_{j2}) + \frac{3}{r_i^2}R_{i1}^2R_{i2}\right]\frac{\partial^2 C}{\partial x_1'\partial x_2'}$$

$$\left. + R_{i2}^2\left[\omega_{ij}R_{j1}R_{j2} + \frac{3}{r_i^2}R_{i1}R_{i2}\right]\frac{\partial^2 C}{\partial x_2'^2}\right\} \qquad \text{B(30)}$$

Large concentration gradients may exist as a result of sharp solvent fronts propagating in the longitudinal direction. With transverse gradients small in the absence of diffusion, the dominant term of the second-order error flux is due to the longitudinal perturbation along the slopes of the propagating concentration front. The error flux, and consequently the divergence can be minimized by constraining the coefficients of the second-order longitudinal partials to vanish in both longitudinal and transverse components.

$$R_{i1}^2\left(\omega_{ij}R_{j1}^2 + \frac{3}{r_i^2}R_{i1}^2\right) + 2\left(\frac{u}{\phi}\right)^2 = 0$$

$$R_{i1}R_{i2}\left(\omega_{ij}R_{j1}^2 + \frac{3}{r_i^2}R_{i1}^2\right) = 0 \qquad \text{B(31)}$$

In this manner, the local errors from high convection rates are damped about the mesh point, and not allowed to grow with propagation. Both first-order numerical smearing and second-order longitudinal oscillations are minimized, but transverse perturbations may still force the second-order error to accumulate and its divergence effect the overall accuracy of the discretization.

The system of constraints, B(31), is expanded in terms of component weights,

$$\cos^2\theta\left[\frac{(1-12\omega_1)}{r_1^2}\cos^2\theta - \frac{12\omega_1}{r_1^2}\sin^2\theta + \frac{3}{r_1^2}\cos^2\theta\right]$$

$$+ \sin^2\theta\left[\frac{-12\omega_2}{r_2^2}\cos^2\theta + \frac{(1-12\omega_2)}{r_2^2}\sin^2\theta + \frac{3}{r_2^2}\sin^2\theta\right] = -2\left(\frac{u}{\phi}\right)^2$$

$$-\cos\theta\sin\theta\left[\frac{(1-12\omega_1)}{r_1^2}\cos^2\theta - \frac{12\omega_1}{r_1^2}\sin^2\theta + \frac{3}{r_1^2}\cos^2\theta\right]$$

$$+ \cos\theta\sin\theta\left[\frac{-12\omega_2}{r_2^2}\cos^2\theta + \frac{(1-12\omega_2)}{r_2^2}\sin^2\theta + \frac{3}{r_1^2}\sin^2\theta\right] = 0 \qquad \text{B(32)}$$

simplified to,

$$\frac{\cos^2\theta}{r_1^2}\left(\cos^2\theta - 3\omega_1\right) + \frac{\sin^2\theta}{r_2^2}\left(\sin^2\theta - 3\omega_2\right) = -\frac{1}{2}\left(\frac{u}{\phi}\right)^2$$

$$\frac{1}{r_1^2}\left(\cos^2\theta - 3\omega_1\right) - \frac{1}{r_2^2}\left(\sin^2\theta - 3\omega_2\right) = 0 \qquad \text{B(33)}$$

and solved simultaneously, to obtain the optimal weights.

$$\omega_1 = \frac{1}{3}\left[\cos^2\theta + \frac{1}{2}\left(\frac{u\Delta t}{\phi\Delta x}\right)^2\right]$$

$$\omega_2 = \frac{1}{3}\left[\sin^2\theta + \frac{1}{2}\left(\frac{u\Delta t}{\phi\Delta y}\right)^2\right] \qquad \text{B(34)}$$

In comparison, Laumbach[17] determines

$$\omega_1 = \frac{1}{3}\left[1 + \frac{1}{2}\left(\frac{u_x\Delta t}{\phi\Delta x}\right)^2\right]$$

$$\omega_2 = \frac{1}{3}\left[1 + \frac{1}{2}\left(\frac{u_y\Delta t}{\phi\Delta y}\right)^2\right] \qquad \text{B(35)}$$

from an alternating direction implicit (ADI) procedure.

The present analysis is valid when both diffusion and adsorption are negligable, and the optimal weights may differ considerably otherwise. As diffusion and adsorption become significant, their second-order errors, E_d and E_a, effectively reduce the overall accuracy. A stability analysis determines the range of TCP applicability and gives the qualitative effects of larger diffusion and adsorption terms.

STABILITY ANALYSIS

The von Neumann method is applied to determine the stability criterion for the direct TCP discretization. The purely-convective

problem has the discrete form,

$$
\begin{aligned}
&-\left\{\frac{1}{4\Delta x}\left[u^{n+\frac{1}{2}}_{x_{i+\frac{1}{2},j}}\left(C^{n+1}_{i+1,j}+C^{n+1}_{ij}+C^{n}_{i+1,j}+C^{n}_{ij}\right)-u^{n+\frac{1}{2}}_{x_{i-\frac{1}{2},j}}\left(C^{n+1}_{ij}+C^{n+1}_{i-1,j}+C^{n}_{ij}+C^{n}_{i-1,j}\right)\right]\right.\\
&\left.+\frac{1}{4\Delta y}\left[u^{n+\frac{1}{2}}_{y_{i,j+\frac{1}{2}}}\left(C^{n+1}_{i,j+1}+C^{n+1}_{ij}+C^{n}_{i,j+1}+C^{n}_{ij}\right)-u^{n+\frac{1}{2}}_{y_{i,j-\frac{1}{2}}}\left(C^{n+1}_{ij}+C^{n+1}_{i,j-1}+C^{n}_{ij}+C^{n}_{i,j-1}\right)\right]\right\}\\
&=\frac{1}{\Delta t}\left\{(1-\omega_1-\omega_2)\phi^{n+\frac{1}{2}}_{ij}\left(C^{n+1}_{ij}-C^{n}_{ij}\right)\right.\\
&\qquad+\frac{\omega_1}{2}\left[\phi^{n+\frac{1}{2}}_{i+1,j}\left(C^{n+1}_{i+1,j}-C^{n}_{i+1,j}\right)+\phi^{n+\frac{1}{2}}_{i-1,j}\left(C^{n+1}_{i-1,j}-C^{n}_{i-1,j}\right)\right]\\
&\qquad\left.+\frac{\omega_2}{2}\left[\phi^{n+\frac{1}{2}}_{i,j+1}\left(C^{n+1}_{i,j+1}-C^{n}_{i,j+1}\right)+\phi^{n+\frac{1}{2}}_{i,j-1}\left(C^{n+1}_{i,j-1}-C^{n}_{i,j-1}\right)\right]\right\}
\end{aligned}
\qquad \text{B(36)}
$$

At each point (x_i, y_j, t^n) in space-time, an error of the form,

$$
\begin{aligned}
&\varepsilon = \exp[\alpha t + i(\beta x+\gamma y)]\\
&i = \sqrt{-1}\,; \quad \alpha,\beta \text{ real constants}
\end{aligned}
\qquad \text{B(37)}
$$

grows with the concentration according to B(36). The relative growth of error is determined by the amplification factor, A, over the time step, Δt,

$$
A = (\varepsilon^{n+1}_{ij}/\varepsilon^{n}_{ij}) = \exp(\alpha\Delta t) \qquad \text{B(38)}
$$

such that,

$$
\begin{aligned}
&\frac{(1+A)}{4\Delta x}\left\{u^{n+\frac{1}{2}}_{x_{i+\frac{1}{2},j}}\left(\varepsilon^{n}_{i+1,j}+\varepsilon^{n}_{ij}\right)-u^{n+\frac{1}{2}}_{x_{j-\frac{1}{2},j}}\left(\varepsilon^{n}_{ij}+\varepsilon^{n}_{i-1,j}\right)\right\}\\
&\quad+\frac{(1+A)}{4\Delta y}\left\{u^{n+\frac{1}{2}}_{y_{i,j+\frac{1}{2}}}\left(\varepsilon^{n}_{i,j+1}+\varepsilon^{n}_{i,j}\right)-u^{n+\frac{1}{2}}_{y_{i,j-\frac{1}{2}}}\left(\varepsilon^{n}_{ij}+\varepsilon^{n}_{i,j-1}\right)\right\}\\
&=\frac{(1-A)}{\Delta t}\left\{(1-\omega_1-\omega_2)\phi^{n+\frac{1}{2}}_{ij}\varepsilon^{n}_{ij}+\frac{\omega_1}{2}\left(\phi^{n+\frac{1}{2}}_{i+1,j}\varepsilon^{n}_{i+1,j}+\phi^{n+\frac{1}{2}}_{i-1,j}\varepsilon^{n}_{i-1,j}\right)\right.\\
&\quad\left.+\frac{\omega_2}{2}\left(\phi^{n+\frac{1}{2}}_{i,j+1}\varepsilon^{n}_{i,j+1}+\phi^{n+\frac{1}{2}}_{i,j-1}\varepsilon^{n}_{i,j-1}\right)\right\}
\end{aligned}
\qquad \text{B(39)}
$$

Cancelling the current central error from both sides simplifies the expression to:

$$\left\{(1-\omega_1-\omega_2)\phi_{ij}^{n+\frac{1}{2}} + \frac{\omega_1}{2}\left[\phi_{i+1,j}^{n+\frac{1}{2}} e^{i\beta\Delta x} + \phi_{i-1,j}^{n+\frac{1}{2}} e^{-i\beta\Delta x}\right] + \frac{\omega_2}{2}\left[\phi_{i,j+1}^{n+\frac{1}{2}} e^{i\gamma\Delta y} + \phi_{i,j-1}^{n+\frac{1}{2}} e^{-i\gamma\Delta y}\right]\right\}$$

$$= \frac{\Delta t}{4}\left(\frac{1+A}{1-A}\right)\left\{\frac{1}{\Delta x}\left[u_{x_{i+\frac{1}{2},j}}^{n+\frac{1}{2}}(1+e^{i\beta\Delta x}) - u_{x_{i-\frac{1}{2},j}}^{n+\frac{1}{2}}(1+e^{-i\beta\Delta x})\right] + \frac{1}{\Delta y}\left[u_{y_{i,j+\frac{1}{2}}}^{n+\frac{1}{2}}(1+e^{i\gamma\Delta y}) - u_{y_{i,j-\frac{1}{2}}}^{n+\frac{1}{2}}(1+e^{-i\gamma\Delta y})\right]\right\} \qquad \text{B(40)}$$

In the absence of both velocity and porosity gradients, B(40) reduces to the complex equation,

$$z = Re_0 + \frac{1+A}{1-A}\, iIm_0 = 0 \qquad \text{B(41)}$$

with the real and imaginary parts,

$$Re_0 = \{1 + [\cos(\beta\Delta x)-1]\omega_1 + [\cos(\gamma\Delta y)-1]\omega_2\}$$

$$Im_0 = -\frac{1}{2}\left\{\frac{u_x\Delta t}{\phi\Delta x}\sin(\beta\Delta x) + \frac{u_y\Delta t}{\phi\Delta y}\sin(\gamma\Delta y)\right\} \qquad \text{B(42)}$$

Solving for the amplifaction factor from B(41),

$$A = \frac{Re_0 + iIm_0}{Re_0 - iIm_0} \qquad \text{B(43)}$$

$$|A| = 1 \Rightarrow \text{WEAKLY STABLE}$$

determines this special case as weakly stable.

The effects of a variable velocity field can be deduced from the

first-order Taylor expansion about the mid-point velocity components in B(40). An additive real term,

$$Re_u = -\frac{\Delta t}{2\phi}\left\{[1+\cos(\beta\Delta x)]\frac{\partial u_x}{\partial x} + [1+\cos(\gamma\Delta y)]\frac{\partial u_y}{\partial y}\right\}$$

$$Re = Re_0 + \left(\frac{1+A}{1-A}\right)Re_u \qquad \text{B(44)}$$

implies adverse stability for a decreasing velocity field.

$$A = \frac{(Re_0 + Re_u) + iIm_0}{(Re_0 - Re_u) - iIm_0} \qquad \text{B(45)}$$

$$Re_u \leq 0 \Rightarrow \text{STABLE}$$

In the same manner, a variable porosity results in an additive imaginary term,

$$Im_\phi = \left\{\omega_1 \sin(\beta\Delta x)\frac{\partial}{\partial x}(\ell n\ \phi) + \omega_2 \sin(\gamma\Delta y)\frac{\partial}{\partial y}(\ell n\ \phi)\right\}$$

$$Im = \left(\frac{1+A}{1-A}\right)Im_0 + Im_\phi \qquad \text{B(46)}$$

with phase dependent stability implications.

$$A = \frac{(Re_0 + Re_u) + i(Im_0 + Im)}{(Re_0 - Re_u) - i(Im_0 - Im)} \qquad \text{B(47)}$$

$$Im_\phi \leq 0 \Rightarrow \text{STABLE}$$

The inclusion of a diffusion term with constant coefficients to the discretization B(36),

$$\left\{ D_{xx} \frac{\partial^2 C}{\partial x^2}\Big|_{ij}^{n+\frac{1}{2}} + D_{yy} \frac{\partial^2 C}{\partial y^2}\Big|_{ij}^{n+\frac{1}{2}} \right\}$$

$$= \left\{ \frac{D_{xx}}{2\Delta x^2} \left[(C_{i+1,j}^{n+1} - 2C_{ij}^{n+1} + C_{i-1,j}^{n+1}) + (C_{i+1,j}^{n} - 2C_{ij}^{n} + C_{i-1,j}^{n}) \right] \right.$$

$$\left. + \frac{D_{yy}}{2\Delta y^2} \left[(C_{i,j+1}^{n+1} - 2C_{ij}^{n+1} + C_{i,j-1}^{n+1}) + (C_{i,j+1}^{n} - 2C_{ij}^{n} + C_{i,j-1}^{n}) \right] \right\} \qquad B(48)$$

results in the addition of a real term,

$$Re_d = -\left\{ \frac{D_{xx}\Delta t}{\phi \Delta x^2} [1 - \cos(\beta \Delta x)] + \frac{D_{yy}\Delta t}{\phi \Delta y^2} [1 - \cos(\gamma \Delta y)] \right\}$$

$$Re = Re_0 + \left(\frac{1+A}{1-A} \right) [Re_u + Re_d] \qquad B(49)$$

which effectively stabilizes the discretization.

$$A = \frac{(Re_0 + Re_u + Re_d) + i(Im_0 + Im_\phi)}{(Re_0 - Re_u - Re_d) - i(Im_0 - Im_\phi)} \qquad B(50)$$

$$Re_d \leq 0 \Rightarrow \text{STABLE}$$

Similarily, the inclusion of an adsorption term,

$$(4\pi N_p r_p^2)_{ij}^{n+\frac{1}{2}} [\alpha (C_{ij}^{n+\frac{1}{2}} - C^*)] = (4\pi N_p r_p^2 \alpha)_{ij}^{n+\frac{1}{2}} [\tfrac{1}{2} (C_{ij}^{n+1} + C_{ij}^{n}) - C^*] \qquad B(51)$$

results in the addition of a real term,

$$Re_a = -(4\pi N_p r_p^2 \alpha)\Delta t$$

$$Re = Re_0 + \left(\frac{1+A}{1-A} \right) [Re_u + Re_d + Re_a] \qquad B(52)$$

which also stabilizes the discretization.

$$A = \frac{(Re_0 + Re_u + Re_d + Re_a) + i(Im_0 + Im_\phi)}{(Re_0 - Re_u - Re_d - Re_a) - i(Im_0 - Im_\phi)} \qquad B(53)$$

$$Re_a \leq 0 \Rightarrow \text{STABLE}$$

The complex error equation of discretization will have the general form:

$$z = Re + iIm = 0 \qquad B(54)$$

To satisfy this equality, both real and imaginary parts must vanish simultaneously. For the special case of pure convection B(42), the system

$$\begin{aligned} 1 + [\cos(\beta\Delta x) - 1]\omega_1 + [\cos(\gamma\Delta y) - 1]\omega_2 &= 0 \\ \frac{u_x}{\Delta x}\sin(\beta\Delta x) + \frac{u_y}{\Delta y}\sin(\gamma\Delta y) &= 0 \end{aligned} \qquad B(55)$$

can be satisfied by setting,

$$\left.\begin{aligned} \beta &= \frac{m\pi}{\Delta x}, \quad m \text{ odd integer} \\ \gamma &= \frac{\ell\pi}{\Delta y}, \quad \ell \text{ odd integer} \end{aligned}\right\} \qquad B(56)$$

to obtain the stability criterion for the weights.

$$\omega_1 + \omega_2 = \frac{1}{2} \qquad B(57)$$

This equality establishes the upper limit to the general case. The general stability condition,

$$\omega_1 + \omega_2 \leq \frac{1}{2} \qquad B(58)$$

bounds the weights and fixes the maximum allowable time step for stability.

$$\omega_1 + \omega_2 = \frac{1}{3}\left\{1 + \frac{1}{2}\left(\frac{u\Delta t}{\phi}\right)^2 \left[\frac{1}{\Delta x^2} + \frac{1}{\Delta y^2}\right]\right\} \leq \frac{1}{2}$$

$$\Delta t \leq \left(\frac{\phi}{u}\right) \frac{\Delta x \Delta y}{\sqrt{\Delta x^2 + \Delta y^2}} \qquad B(59)$$

As $\Delta y \to \infty$, the discretization collapses to one-dimension, the velocity aligns with the x-direction and the y-weight vanishes. The nontrivial weight and the corresponding time step,

$$\omega_1 = \frac{1}{3}\left[1 + \frac{1}{2}\left(\frac{u_x \Delta t}{\phi \Delta x}\right)^2\right]$$

$$\Delta t \leq \frac{\phi \Delta x}{u} \qquad B(60)$$

reduce to those cited by Laumbach[17] for the one-dimensional analysis.

APPENDIX C

THE ANALYTICAL SOLUTION FOR THE ONE-DIMENSIONAL CONSTANT-COEFFICIENT CONVECTIVE-DIFFUSION EQUATION

The method of Laplace transform is used to obtain the analytical solution to

$$\frac{1}{N_{Pe}} \frac{\partial^2 C}{\partial \xi^2} - \frac{\partial C}{\partial \xi} = \frac{\partial C}{\partial \tau} \qquad C(1)$$

satisfying the initial and boundary conditions:

$$C = 0 \qquad \tau = 0, \qquad \xi > 0 \qquad C(2)$$

$$C = C_0 \qquad \xi = 0, \qquad \tau > 0 \qquad C(3)$$

$$\frac{\partial C}{\partial \xi} = 0 \qquad \xi = 1, \qquad \tau > 0 \qquad C(4)$$

Applying the Laplace transform,

$$\mathcal{L}\{C(\xi,\tau)\} = \int_0^\infty Ce^{-p\tau} d\tau = \bar{C}(\xi,p) \qquad C(5)$$

to C(1), gives:

$$\frac{1}{N_{Pe}} \int_0^\infty e^{-p\tau} \frac{\partial^2 C}{\partial \xi^2} d\tau - \int_0^\infty e^{-p\tau} \frac{\partial C}{\partial \xi} d\tau - \int_0^\infty e^{-p\tau} \frac{\partial C}{\partial \tau} d\tau = 0 \qquad C(6)$$

Interchanging the order of integration and differentiation,

$$\frac{1}{N_{Pe}} \frac{\partial^2}{\partial \xi^2} \int_0^\infty e^{-p\tau} C d\tau - \frac{\partial}{\partial \xi} \int_0^\infty e^{-p\tau} C d\tau - \int_0^\infty e^{-p\tau} \frac{\partial C}{\partial \tau} d\tau = 0 \qquad C(7)$$

and integrating the last term by parts, yields:

$$\frac{1}{N_{Pe}} \frac{\partial^2 \bar{C}}{\partial \xi^2} - \frac{\partial \bar{C}}{\partial \xi} - Ce^{-p\tau}\Big|_0^\infty - p\bar{C} = 0 \qquad C(8)$$

By virtue of the initial condition C(2), the third term of C(8) vanishes and the Laplace transformed equation becomes the ordinary differential equation,

$$\frac{1}{N_{Pe}} \frac{\partial^2 \bar{C}}{\partial \xi^2} - \frac{\partial \bar{C}}{\partial \xi} - p\bar{C} = 0 \qquad C(9)$$

with the boundary conditions:

$$\bar{C} = \int_0^\infty C_0 e^{-p\tau} d\tau = \frac{C_0}{p}, \quad \xi = 0 \qquad C(10)$$

$$\frac{\partial \bar{C}}{\partial \xi} = 0, \quad \xi = 1 \qquad C(11)$$

The characteristic equation of the O.D.E. C(9)

$$\frac{1}{N_{Pe}} r^2 - r - p = 0 \qquad C(12)$$

whose roots,

$$r = \frac{N_{Pe}}{2} \pm \frac{N_{Pe}}{2} \sqrt{1 + \frac{4p}{N_{Pe}}} \qquad C(13)$$

determine the general solution,

$$\bar{C}(\xi,p) = A \exp\left[\left(\frac{N_{Pe}}{2} + \frac{N_{Pe}}{2} \sqrt{1 + \frac{4p}{N_{Pe}}}\right)\xi\right] + B \exp\left[\left(\frac{N_{Pe}}{2} - \frac{N_{Pe}}{2} \sqrt{1 + \frac{4p}{N_{Pe}}}\right)\xi\right] \qquad C(14)$$

where A and B are constants to be determined by the boundary conditions C(3) and C(4).

By defining the variable,

$$q = \sqrt{\frac{N_{Pe}}{4} + p} \qquad C(15)$$

the general solution C(14) and its first-order spatial derivative can be written in the forms,

$$\bar{C} = \left\{ Ae^{\sqrt{N_{Pe}}\, q\xi} + Be^{-\sqrt{N_{Pe}}\, q\xi} \right\} e^{N_{Pe}\xi/2} \qquad C(16)$$

$$\frac{\partial \bar{C}}{\partial \xi} = \left\{ A\left(\sqrt{N_{Pe}}\, q + \frac{N_{Pe}}{2}\right) e^{\sqrt{N_{Pe}}\, q\xi} - B\left(\sqrt{N_{Pe}}\, q - \frac{N_{Pe}}{2}\right) e^{-\sqrt{N_{Pe}}\, q\xi} \right\} e^{N_{Pe}\xi/2} \qquad C(17)$$

Applying the boundary conditions C(3) and C(4),

$$\bar{C}\big|_{\xi=0} = A + B = \frac{C_0}{p} \qquad C(18)$$

$$\frac{\partial \bar{C}}{\partial \xi}\Big|_{\xi=1} = \left\{ A\left(\sqrt{N_{Pe}}\, q + \frac{N_{Pe}}{2}\right) e^{\sqrt{N_{Pe}}\, q} - B\left(\sqrt{N_{Pe}}\, q - \frac{N_{Pe}}{2}\right) e^{-\sqrt{N_{Pe}}\, q} \right\} e^{N_{Pe}/2} = 0 \qquad C(19)$$

and simultaneously solving for A and B gives:

$$A = \frac{C_0}{p} \left\{ \frac{\left(q - \frac{\sqrt{N_{Pe}}}{2}\right) e^{-\sqrt{N_{Pe}}\, q}}{\left(q + \frac{\sqrt{N_{Pe}}}{2}\right) e^{\sqrt{N_{Pe}}\, q} + \left(q - \frac{\sqrt{N_{Pe}}}{2}\right) e^{-\sqrt{N_{Pe}}\, q}} \right\} \qquad C(20)$$

$$B = \frac{C_0}{p} \left\{ \frac{\left(q + \frac{\sqrt{N_{Pe}}}{2}\right) e^{\sqrt{N_{Pe}}\, q}}{\left(q + \frac{\sqrt{N_{Pe}}}{2}\right) e^{\sqrt{N_{Pe}}\, q} + \left(q - \frac{\sqrt{N_{Pe}}}{2}\right) e^{-\sqrt{N_{Pe}}\, q}} \right\} \qquad C(21)$$

The particular solution to C(9) satisfying the boundary conditions C(10) and C(11) is:

$$\bar{C} = \frac{C_0}{p} \left\{ \frac{\left(q + \frac{\sqrt{N_{Pe}}}{2}\right) e^{\sqrt{N_{Pe}}\, q(1-\xi)} + \left(q - \frac{\sqrt{N_{Pe}}}{2}\right) e^{-\sqrt{N_{Pe}}\, q(1-\xi)}}{\left(q + \frac{\sqrt{N_{Pe}}}{2}\right) e^{\sqrt{N_{Pe}}\, q} + \left(q - \frac{\sqrt{N_{Pe}}}{2}\right) e^{-\sqrt{N_{Pe}}\, q}} \right\} e^{N_{Pe}\xi/2} \qquad C(22)$$

The analytical solution to C(1) satisfying the initial and boundary conditions C(2), C(3), and C(4) is the inverse Laplace transform of C(22).

$$C(\xi,\tau) = \mathcal{L}^{-1}\, \bar{C}(\xi,p) \qquad C(23)$$

By defining the variables,

$$a = \frac{N_{Pe}}{4} \qquad C(24)$$

$$s = p + a = q^2 \qquad C(25)$$

and applying the translation property of Laplace transform,

$$C(\xi,\tau) = e^{-a\tau}\mathcal{L}^{-1}\{\bar{C}(\xi,p+a)\} = e^{-a\tau}\mathcal{L}^{-1}\{\bar{C}(\xi,s)\} \qquad C(26)$$

where

$$\bar{C}(\xi,s) = \frac{C_0}{s-a} \left\{ \frac{(\sqrt{s}+\sqrt{a})e^{2\sqrt{as}(1-\xi)} + (\sqrt{s}-\sqrt{a})e^{-2\sqrt{as}(1-\xi)}}{(\sqrt{s}+\sqrt{a})e^{2\sqrt{as}} + (\sqrt{s}-\sqrt{a})e^{-2\sqrt{as}}} \right\} e^{2a\xi} \qquad C(27)$$

By rearranging C(27),

$$\bar{C}(\xi,s) = C_0 e^{2a\xi} \left\{ \frac{(s-a)^{-1} e^{2\sqrt{as}(1-\xi)} + (\sqrt{s}+\sqrt{a})^{-2} e^{-\sqrt{as}(1-\xi)}}{1 + \left(\frac{\sqrt{s}-\sqrt{a}}{\sqrt{s}+\sqrt{a}}\right) e^{-4\sqrt{as}}} \right\} \qquad C(28)$$

and applying the binomial expansion to the denominator,

$$\left[1 + \left(\frac{\sqrt{s}-\sqrt{a}}{\sqrt{s}+\sqrt{a}}\right) e^{-4\sqrt{as}}\right]^{-1} = \sum_{n=0}^{\infty} (-1)^n \left(\frac{\sqrt{s}-\sqrt{a}}{\sqrt{s}+\sqrt{a}}\right)^n e^{-4n\sqrt{as}} \qquad C(29)$$

gives the infinite series:

$$\bar{C}(\xi,s) = C_0 e^{2a\xi} \sum_{n=0}^{\infty} (-1)^n \left\{ \frac{(\sqrt{s}-\sqrt{a})^{n-1}}{(\sqrt{s}+\sqrt{a})^{n+1}} e^{-2\sqrt{as}(2n+\xi)} + \frac{(\sqrt{s}-\sqrt{a})^{n}}{(\sqrt{s}+\sqrt{a})^{n+2}} e^{-2\sqrt{as}(2n+2-\xi)} \right\} \qquad C(30)$$

The infinite series can be expanded into,

$$\bar{C}(\xi,s) = C_0 e^{2a\xi} \left\{ \frac{e^{-2\sqrt{as}\,\xi}}{(s-a)} + \frac{e^{-2\sqrt{as}(2-\xi)}}{(\sqrt{s}+\sqrt{a})^2} - \frac{e^{-2\sqrt{as}(2+\xi)}}{(\sqrt{s}+\sqrt{a})^2} + \frac{(\sqrt{s}-\sqrt{a})}{(\sqrt{s}+\sqrt{a})^3} e^{-2\sqrt{as}(4-\xi)} + \cdots \right\} \qquad C(31)$$

and with the linearity property of inverse Laplace transform,

$$C(\xi,\tau) = C_0 e^{2a\xi} e^{-a\tau} \left| \mathcal{L}^{-1}\left\{\frac{e^{-2\sqrt{as}\,\xi}}{(s-a)}\right\} + \mathcal{L}^{-1}\left\{\frac{e^{-2\sqrt{as}(2-\xi)}}{(\sqrt{s}+\sqrt{a})^2}\right\} + \mathcal{L}^{-1}\left\{\frac{-e^{-2\sqrt{as}(2+\xi)}}{(\sqrt{s}+\sqrt{a})^2}\right\} + \cdots \right| \qquad C(32)$$

The first term of the series is recognized as the solution to the semi-infinite case and the physical significance of the successive terms constitute superimposed diffusion reflections at the outlet boundary $(\xi = 1)$. It can be shown that the series C(32) converges rapidly for Peclet numbers (N_{Pe}) and times (τ) of interest, and can be accurately approximated by the first three terms.

From Crank[46]:

$$\mathcal{L}^{-1}\left\{\frac{e^{-2\sqrt{as}\ \xi}}{s-a}\right\} = \frac{1}{2}\, e^{a\tau}\left\{e^{-2a\xi}\ \text{erfc}\left[\sqrt{\frac{a}{\tau}}\,\xi - \sqrt{a\tau}\right] + e^{2a\xi}\ \text{erfc}\left[\sqrt{\frac{a}{\tau}}\,\xi + \sqrt{a\tau}\right]\right\} \qquad \text{C(33)}$$

From Oberhettinger and Badii[47]:

$$\mathcal{L}^{-1}\left\{\frac{e^{-2\sqrt{as}(2\pm\xi)}}{(\sqrt{s}+\sqrt{a})^2}\right\} = \left\{(2a\tau+2a(2\pm\xi)+1)\exp[2a(2\pm\xi)+a\tau]\,\text{erfc}\left[\sqrt{\frac{a}{\tau}}\,(2\pm\xi)+\sqrt{a\tau}\right] - 2\sqrt{\frac{a\tau}{\pi}}\exp\left[-\frac{a}{\tau}\,(2\pm\xi)^2\right]\right\} \qquad \text{C(34)}$$

Substituting for the inverse Laplace transforms C(33) and C(34) into C(32), the analytical solution to the one-dimensional convective-diffusion equation with constant coefficients in terms of the Peclet number is:

$$C(\xi,\tau) = \frac{1}{2}\left\{\operatorname{erfc}\left[\frac{1}{2}\sqrt{\frac{N_{Pe}}{\tau}}\,(\xi-\tau)\right] + e^{N_{Pe}\xi}\operatorname{erfc}\left[\frac{1}{2}\sqrt{\frac{N_{Pe}}{\tau}}\,(\xi+\tau)\right]\right\}$$

$$+\left\{\left[\frac{N_{Pe}}{2}\,(2-\xi+\tau)+1\right]e^{N_{Pe}}\operatorname{erfc}\left[\frac{1}{2}\sqrt{\frac{N_{Pe}}{\tau}}\,(2-\xi+\tau)\right]\right.$$

$$\left.-\sqrt{\frac{N_{Pe}\,\tau}{\pi}}\exp\left(-\frac{N_{Pe}}{4}\left[\frac{(2-\xi)^2}{\tau}-2\xi+\tau\right]\right)\right\}$$

$$-\left\{\left[\frac{N_{Pe}}{2}\,(2+\xi+\tau)+1\right]e^{N_{pe}(1+\xi)}\operatorname{erfc}\left[\frac{1}{2}\sqrt{\frac{N_{Pe}}{\tau}}\,(2+\xi+\tau)\right]\right.$$

$$\left.-\sqrt{\frac{N_{Pe}\,\tau}{\pi}}\exp\left(-\frac{N_{Pe}}{4}\left[\frac{(2+\xi)^2}{\tau}-2\xi+\tau\right]\right)\right\} \qquad C(35)$$

APPENDIX D

THE OPERATOR COMPACT IMPLICIT METHOD

The operator compact implicit method[30] seeks a linear relationship between the operator and the corresponding concentrations on the m-point difference star. For the one-dimensional constant coefficient case,

$$L(C) = \left(D_{xx} \frac{\partial^2}{\partial x^2} - u_x \frac{\partial}{\partial x} \right) C \qquad D(1)$$

and for $m = 3$,

$$q_{i-1} L(C_{i-1}) + q_i L(C_i) + q_{i+1} L(C_{i+1}) = r_{i-1} C_{i-1} + r_i C_i + r_{i+1} C_{i+1} + r_0 \qquad D(2)$$

where the q's and r's are unknown weighting coefficients to be determined on the basis of the highest-order accuracy possible on the m-point difference-star.

A linear combination of the concentration and their corresponding operators at the peripheral mesh points using fourth-order Taylor series results in the expression:

$$\alpha_1 C_{i+1} + \alpha_2 C_{i-1} + \beta_1 L(C_{i+1}) + \beta_2 L(C_{i-1}) = \left\{ \gamma_{00} C_i + \gamma_{10} \frac{\partial C}{\partial x}\Big|_i + \gamma_{20} \frac{\partial^2 C}{\partial x^2}\Big|_i + \gamma_{30} \frac{\partial^3 C}{\partial x^3}\Big|_i + \gamma_{40} \frac{\partial^4 C}{\partial x^4}\Big|_i \right\} \qquad D(3)$$

where the γ-coefficients arise from the regrouping of Taylor terms.

$$\gamma_{00} = (\alpha_1 + \alpha_2)$$

$$\gamma_{10} = \Delta x \left\{ (\alpha_1 - \alpha_2) + \beta_1 \left(\frac{-u_x}{\Delta x} \right)_{i+1} + \beta_2 \left(\frac{-u_x}{\Delta x} \right)_{i-1} \right\}$$

$$\gamma_{20} = \frac{\Delta x^2}{2} \left\{ (\alpha_1 + \alpha_2) + \beta_1 \left(\frac{2D_{xx}}{\Delta x^2} - \frac{2u_x}{\Delta x} \right)_{i+1} + \beta_2 \left(\frac{2D_{xx}}{\Delta x^2} + \frac{2u_x}{\Delta x} \right)_{i-1} \right\}$$

$$\gamma_{30} = \frac{\Delta x^3}{6} \left\{ (\alpha_1 - \alpha_2) + \beta_1 \left(\frac{6D_{xx}}{\Delta x^2} - \frac{3u_x}{\Delta x} \right)_{i+1} - \beta_2 \left(\frac{6D_{xx}}{\Delta x^2} + \frac{3u_x}{\Delta x} \right)_{i-1} \right\}$$

$$\gamma_{40} = \frac{\Delta x^4}{24} \left\{ (\alpha_1 + \alpha_2) + \beta_1 \left(\frac{12D_{xx}}{\Delta x^2} - \frac{4u_x}{\Delta x} \right)_{i+1} - \beta_2 \left(\frac{12D_{xx}}{\Delta x^2} + \frac{4u_x}{\Delta x} \right)_{i-1} \right\} \qquad D(4)$$

Equating the γ-coefficients to

$$\left.\begin{aligned} \gamma_{10} &= -u_{x_i} \\ \gamma_{20} &= D_{xx_i} \\ \gamma_{30} &= 0 \\ \gamma_{40} &= 0 \end{aligned}\right\} \qquad D(5)$$

forces the right-hand side of D(3) to be a linear combination of the concentration and operator at the central mesh point,

$$\alpha_1 C_{i+1} - \gamma_{00} C_i + \alpha_2 C_{i-1} = -\beta_1 L(C_{i+1}) + L(C_i) - \beta_2 L(C_{i-1}) \qquad D(6)$$

The γ-constraints D(5) yield four equations to determine the α's and β's. By setting,

$$\left.\begin{aligned} r_{i+1} &= \alpha_1 & q_{i+1} &= -\beta_1 \\ r_{i-1} &= \alpha_2 & q_{i-1} &= -\beta_2 \\ r_i &= -\gamma_{00} & q_i &= 1 \\ r_0 &= 0 \end{aligned}\right\} \qquad D(7)$$

equation D(2) is obtained directly from D(6), and can be written in the compact form:

$$QL(C_i) = RC_i + r_0 \qquad D(8)$$

with,

$$\left.\begin{aligned} Q &= q_{i-1}S_{i-1} + q_iI + q_{i+1}S_{i+1} \\ R &= r_{i-1}S_{i-1} + r_iI + r_{i+1}S_{i+1} \end{aligned}\right\} \qquad D(9)$$

where S and I are the shift and identity operators, respectively.

The compact operator can be isolated as

$$L(C_i) = Q^{-1}RC_i + Q^{-1}r_0 \qquad D(10)$$

if the inverse of Q exists, and subsequently equated to the accumulation term,

$$L(C_i) = \phi_m \frac{\partial C_i}{\partial t} \qquad D(11)$$

Using the Crank-Nicolson temporal discretization gives the resulting OCI difference equation:

$$\left(\frac{\phi_m}{\Delta t} Q^{n+\frac{1}{2}} - \frac{R^{n+\frac{1}{2}}}{2}\right) C_i^{n+1} = \left(\frac{\phi_m}{\Delta t} Q^{n+\frac{1}{2}} + \frac{R^{n+\frac{1}{2}}}{2}\right) C_i^n + r_0^{n+\frac{1}{2}} \qquad D(12)$$

The significance of r_0 is observed when the boundary conditions are applied on the boundary-stars $(i,i\pm1,i\pm2)$. For these difference-stars, the first-order spatial derivative is specified as a boundary condition and consequently the first-order γ-coefficient need not be constrained. In order to obtain four equations in four unknowns, the Taylor series expansions are applied to fifth-order, such that

$$\alpha_1 C_{i\pm1} + \alpha_2 C_{i\pm2} + \beta_1 L(C_{i\pm1}) + \beta_2 L(C_{i\pm2})$$

$$= \left\{\gamma_{00} C_i + \gamma_{10} \frac{\partial C}{\partial x}\Big|_i + \gamma_{20} \frac{\partial^2 C}{\partial x^2}\Big|_i + \gamma_{30} \frac{\partial^3 C}{\partial x^3}\Big|_i + \gamma_{40} \frac{\partial^4 C}{\partial x^4}\Big|_i \right.$$

$$\left. + \gamma_{50} \frac{\partial^5 C}{\partial x^5}\Big|_i \right\} \cdots \qquad D(13)$$

Applying the boundary conditions for inlet D(14), or outlet D(15),

$$\frac{\partial C}{\partial x}\Big|_i = -\frac{1}{(1-\alpha_s)} \frac{D_{xx}}{u_x} (C_{IN} - C_i) \qquad D(14)$$

$$\frac{\partial C}{\partial x}\Big|_i = 0 \qquad D(15)$$

at the peripheral mesh point, leads to the necessary conditions:

$$\left.\begin{array}{lll} \gamma_{20} = D_{xx} & q_{i\pm1} = -\beta_1 & r_{i\pm1} = \alpha_1 \\ \gamma_{30} = 0 & q_{i\pm2} = -\beta_2 & r_{i\pm2} = \alpha_2 \\ \gamma_{40} = 0 & q_i = 1 & \\ \gamma_{50} = 0 & & \end{array}\right\} \qquad D(16)$$

with,

$$\left.\begin{aligned} r_i &= -\left[\gamma_{00} + \frac{1}{(1-\alpha_s)} \frac{u_x}{D_{xx}} (u_x + \gamma_{10})\right] \\ r_0 &= \left[\frac{1}{1-\alpha_s} \frac{u_x}{D_{xx}} (u_x + \gamma_{10})\right] C_{IN} \end{aligned}\right\} \qquad D(17)$$

$$\left.\begin{aligned} r_i &= -\gamma_{00} \\ r_0 &= 0 \end{aligned}\right\} \qquad D(18)$$

for inlet and outlet points, respectively.

The invertibility of Q is discussed by Ciment, Leventhal and Weinberg[30], and for an interior point, the invertibility criterion depends on the cell-Peclet number,

$$N_{Ce} = \frac{u_x \Delta x}{D_{xx}} \leq \sqrt{12} \approx 3.464 \qquad D(19)$$

Extension to two dimensions for ADIP involves explicit evaluation of Q^{-1}, however, for direct methods no explicit evaluation of mid-time operators are required. A complete two-dimensional operator including second-order mixed partials requires a nine-point $(m = 9)$ difference-star for direct solution methods. The

invertibility criterion limits the lower bound of the grid size necessary. Since $2(m-1)$ equations must be solved simultaneously at every point in the mesh-centered grid, the amount of work necessary to generate a solution becomes phenomenal in comparison to other methods.

B30402